Durham E-Theses

Simulation of x-ray section topographs due to hydrogen precipitates in silicon

Holland, Anthony James

How to cite:

Use policy

Simulation of X-ray Section Topographs due to Hydrogen Precipitates in Silicon

Anthony James Holland, B.Sc. (Dunelm)

A thesis submitted to the University of Durham
for the Degree of M.Sc.

November 21, 1989

1 1 MAY 1990

Abstract

Computer simulation of X-ray diffraction section topographs has been used to investigate hydrogen precipitates in silicon crystals. The field of X-ray topography is reviewed, with an account of image formation and the experimental techniques used to obtain topographs. The dynamical theory, for a perfect crystal, and Takagi's theory, for an imperfect crystal, are both presented. Simulation techniques, based on numerical integration of Takagi's equations, are then discussed. A computer program is presented, which is used to simulate the experimental topographs due to hydrogen precipitates in silicon, allowing the positions of precipitates to be located. A second simulation program, to take into account the effects of surface relaxation, is constructed. Simulations with and without surface relaxation are compared, and their differences are discussed. Finally, the effect upon simulations of crystal bending is investigated. This is an important consideration, since the growth of an oxide layer onto a silicon wafer, resulting in wafer curvature, is an integral part of silicon device production technology. Possibilities for future work are discussed.

Acknowledgements

Contents

Chapter 1

Introduction to X-ray Diffraction Topography

X-ray Diffraction Topography is a powerful, non-destructive experimental technique used to image microscopic defects in crystals. It is related to the sister-technique of Transmission Electron Microscopy, but has several advantages over the latter. For example, X-ray topography can be used to investigate large volume samples and can be used many times on the same sample, without affecting the structure of that sample. As will be seen later, the technique is of great use in the semiconductor industry.

A topograph is obtained by subjecting a crystal to an X-ray beam and recording the intensity distribution of the beam diffracted by the crystal. The recording can be done either by a T.V. system or, more commonly, by photographic film.

The images on topographs can be thought of as arising from two processes; *orientation contrast* and *extinction contrast*.

Suppose we have a crystal oriented so that Bragg reflection occurs from a particular set of lattice places, for monochromatic X-radiation. Then if the crystal contains a region misoriented relative to the rest of the lattice, Fig. 1.1(a), the planes in the misoriented region cannot give rise to Bragg reflection. Hence, the region AB on the photographic film will be darkened, whilst the region BC will be light. This contrast is *orientation contrast* and can be clearly seen as a sharp boundary on a topograph.

Alternatively, orientation contrast may also arise if a polychromatic beam is incident on the same crystal. The directions of the beams reflected from the two sets of lattice planes are different, so that a region DE of reduced darkening appears on the film, Fig. 1.1(b).

Extinction contrast, on the other hand, arises when a lattice is elastically deformed by the presence of a defect. Such deformation changes the diffraction properties of the lattice, locally, and so there is a different scattered intensity from the vicinity of the defect.

Several thorough reviews of the experimental methods for obtaining topographs have been written [1,2,3]. The three most widely used laboratory techniques are

film   A B   C

NO CONTRAST

crystal

(a)

film   D   E

LOSS

crystal

(b)
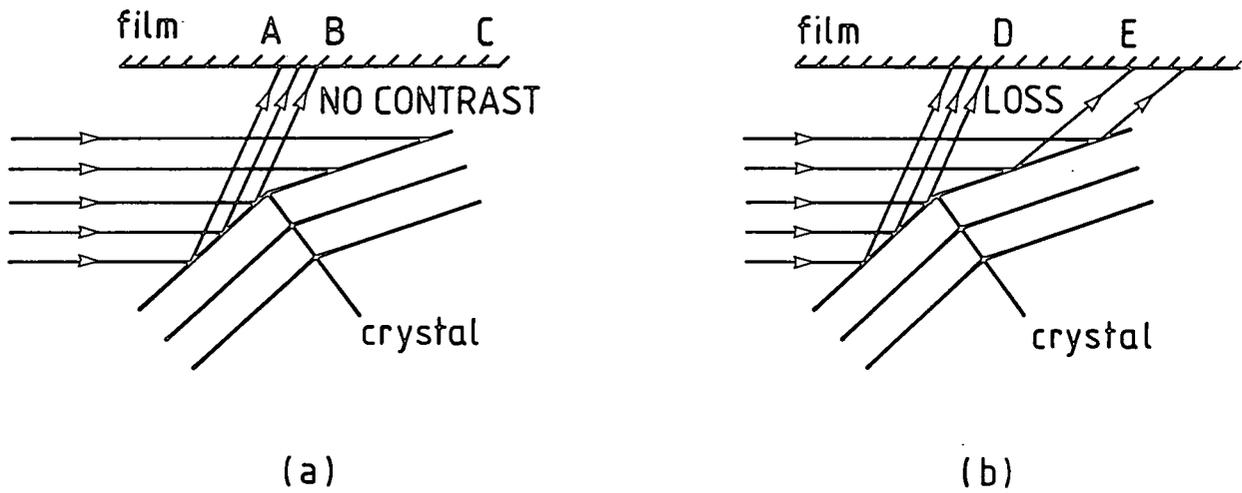
Fig. 1.1: Orientation contrast.

film

source

crystal

(a)

film

slit

source

crystal

(b)
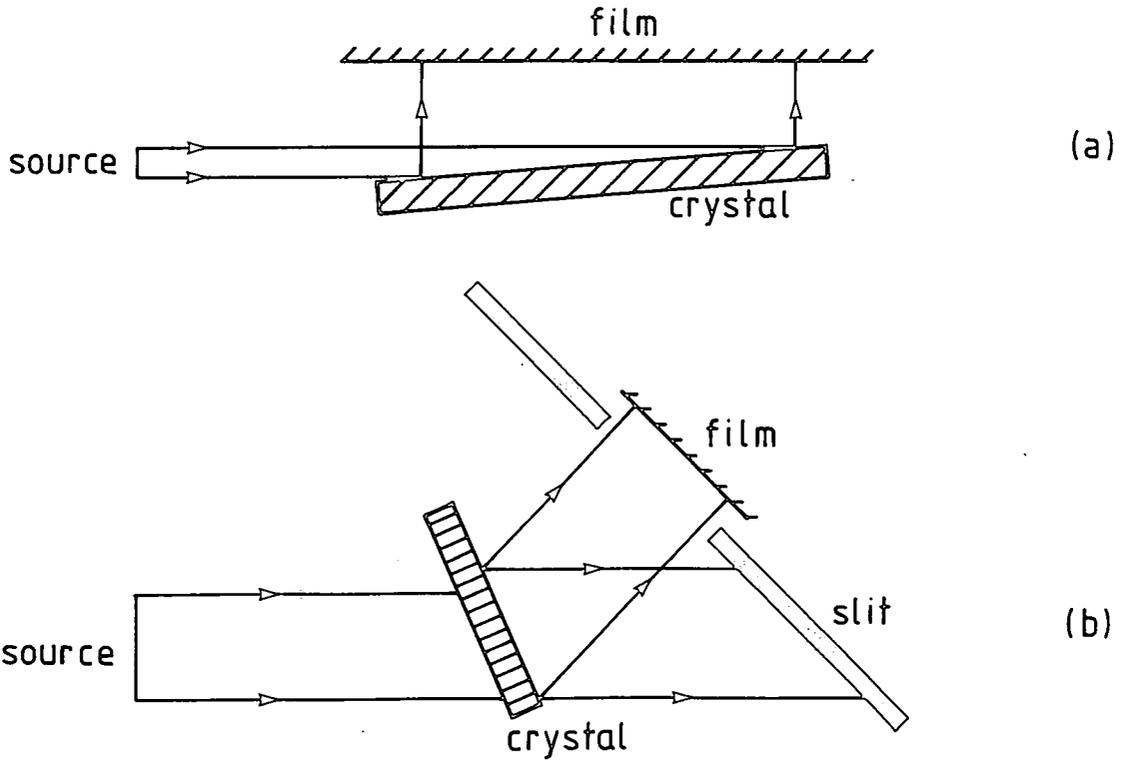
Fig. 1.2: The Berg-Barrett Method:
           (a) Reflection (Bragg) Geometry.
           (b) Transmission (Laue) Geometry.

section topography, *projection topography* and *double-crystal topography*. These techniques have been complemented by the relatively new method of *synchrotron radiation topography*. All of these techniques will be discussed in due course.

All experimental systems correspond to one of two types: the reflection (Bragg) geometry and the transmission (Laue) geometry. The difference between the two is shown in Fig. 1.2, which illustrates the *Berg-Barrett method.*

In both cases, the beam diffracted by the Bragg planes is incident upon a photographic film. In the reflection case, the Bragg planes are inclined to the crystal surface such that the incident beam is diffracted away from the crystal. In the transmission case, the diffracted beam passes through the crystal. A slit then allows this diffracted beam to fall onto the film, whilst blocking the primary transmitted beam. Clearly, the reflection method enables us to probe the surface layer of the crystal, whereas the transmission method allows us to explore the bulk.

In order to understand properly the structure of the images due to defects, it is necessary to use the *dynamical theory* of X-rays in crystals. Here, it is sufficient to use the geometrical approach illustrated in Fig. 1.3. The structure of defect images is described more fully by Authier [4].

The formation of the image in a section topograph due to a dislocation, for example, is illustrated schematically in Fig. 1.3.

The direct beam intersects the dislocation line, D, at point P, and is reflected from this point. The crystal is distorted in the vicinity of P, as a result of the dislocation. This means that rays in the direct beam which do not satisfy the exact Bragg condition for the perfect crystal, can still be reflected from the vicinity of P. Reflection of the direct beam from P gives rise to a dark spot called the *direct image*, around point (1) on the photographic plate.

The dislocation disturbs the energy flow in the direction AQ. Energy is re-distributed throughout the Borrmann fan, ABC, so that there is a reduction in energy being directed along QL. This results in a light patch called the *dynamical image*, around point (3) on the photographic plate.

New wavefields created at Q, and propagating along QM, for example, interfere with the original wavefields to give a series of bright and dark fringes around position (2) on the photographic plate. This series of fringes is called the *intermediary image.*

The direct, intermediary and dynamical images merge to form the defect image as seen on a topograph. This image is superimposed on a background of parallel bright and dark bands occupying the whole topograph. These background bands are called *Pendellösung fringes* [5] and their origin can be traced back to dynamical theory.

Having seen the form taken by section topograph images, let us look at the means by which topographs are obtained experimentally.

One of the most widely used experimental techniques is the *Lang method*, illustrated in Fig. 1.4.
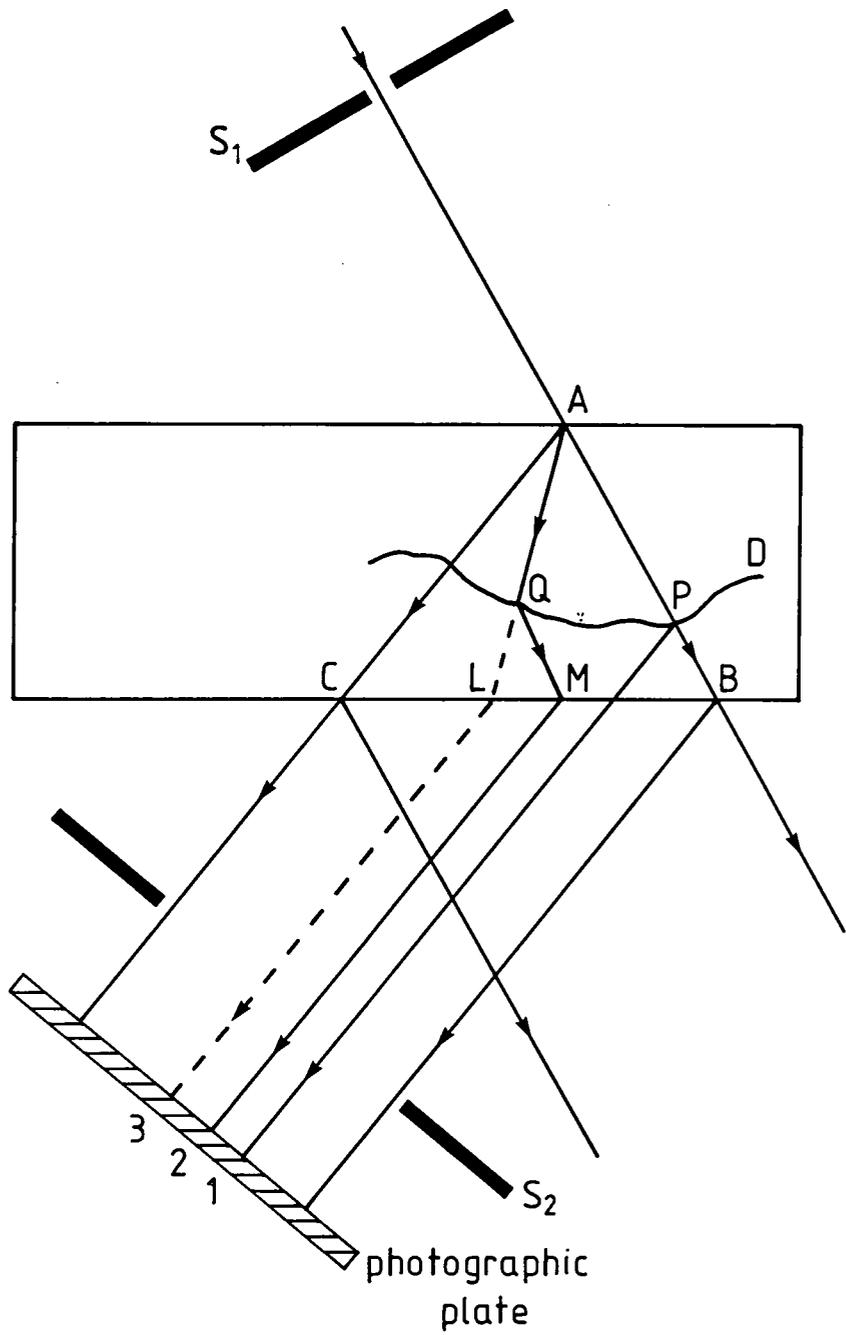
Fig. 1.3: Image structure in transmission topographs, (after Authier).
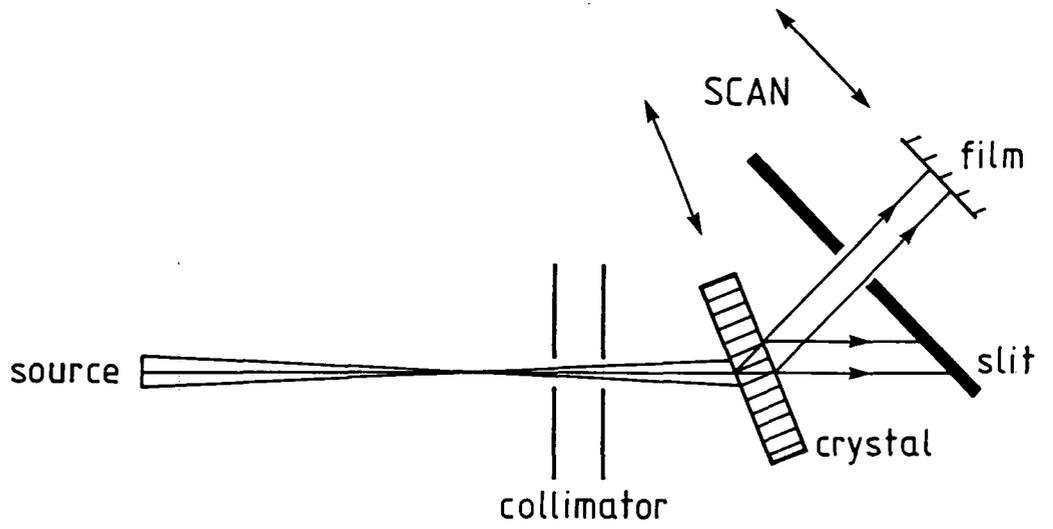
Fig. 1.4:   Lang's transmission method.
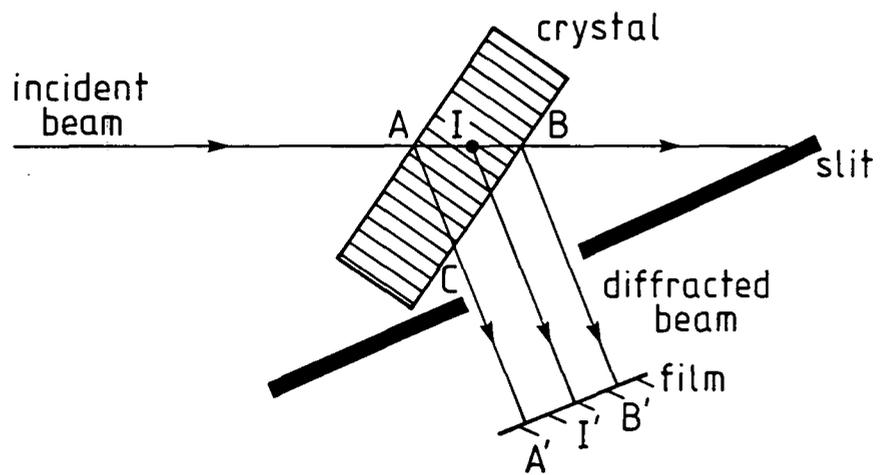
Fig. 1.5:   Location of defect position using
a section topograph.

The advantage of the Lang technique is that it is sensitive to both orientation and extinction contrast. Clearly, the arrangement of Fig. 1.4 is very similar to the transmission Berg-Barrett method.

The radiation usually used in these experiments is the K_α line. This line is, in fact, a closely-spaced doublet, where the $K_{\alpha1}$ component has twice the intensity of the $K_{\alpha2}$. The problem of double-imaging is avoided by collimating the incident beam to such an extent that the $K_{\alpha1}$ and $K_{\alpha2}$ lines are not simultaneously diffracted.

First of all, let us disregard the arrows in Fig. 1.4. The diffracted beam is allowed to fall onto a photographic film, after passing through a slit which blocks the transmitted beam. The intensity distribution across the film gives rise to a *section topograph* [6].

If the crystal and film are traversed together across the incident beam, as indicated by the double arrow in Fig. 1.4, then a *projection topograph* is obtained [7,8]. In this case, the image on the film is a projection of the defect content of the entire crystal.

The advantage of projection topography is that in dealing with dislocations, for example, one can trace the full length of the defect on the topograph. However, the overlapping of defects in three dimensions will cause images to be superimposed, making more difficult the interpretation of the topograph.

The advantage of section topography is that it enables one to locate the position of a defect within a crystal. Consider Fig. 1.5. First of all, it is necessary to have a beam whose width is much smaller than the base length of the Borrmann triangle, ABC. By geometrical considerations, the ratio of lengths AI/AB is equal to A'I'/A'B'. I' is the direct image, due to those rays from the point, I, where the beam AB intersects the defect. Hence, by measuring the position of I' on the film, the depth of the defect in the crystal can be determined.

The type of defect most widely studied by these methods is the dislocation, mentioned previously. Amelinckx [9] gives an excellent review of this field.

It is worthwhile to consider briefly the actual recording of a topograph on photographic film. There is little point in taking great care over the pre-experimental set-up, if the quality of the medium for recording the diffracted beam is poor. Certainly, since dislocation images tend to be greater than one micron in width, it is necessary to use a photographic emulsion of grain size less than this, to obtain satisfactory resolution. The fundamental dilemma is that whilst it is desirable to have thin emulsion for good resolution, it is also desirable to have thick emulsion to compensate for relatively low absorption of X-rays. For each experiment, a compromise between good resolution and absorption efficiency is necessary to generate the optimum result.

Since there are no X-ray lenses, it is necessary to enlarge the initial topograph by optical means. This is done by placing the topograph under a microscope, under conditions of illumination, and taking a photograph through the microscope lens. Scattering of light from emulsions should be minimised, since this reduces the contrast of dislocations. Normally, topographs are viewed under transmitted light,

but for overexposed or overdeveloped topographs, detail which would otherwise have been lost can be reclaimed by viewing in reflected light [10].

The third laboratory method for obtaining topographs is the double-crystal method [11,12], illustrated in Fig. 1.6.

The double-crystal method involves two successive Bragg-reflections off crystals whose Bragg planes are parallel and equally spaced. In order to obtain a diffracted beam of appreciable intensity, it is necessary that the Bragg condition is fulfilled almost exactly for both crystals simultaneously. Consequently, when one of the crystals is rotated, the intensity, I, of the diffracted beam falls off rapidly with angular deviation, $\Delta\theta$, from the exact Bragg condition. Plots of I against $\Delta\theta$ are called *rocking curves*, and the rocking curve shown in Fig. 1.6 for the double-crystal technique is very sharp. Extinction and orientation contrast result from distortion and misorientation, respectively, of the planes in a crystal lattice. It will be seen, then, that the double-crystal technique is highly sensitive to both forms of contrast. In fact, it is possible to use the technique to detect much slower variations in lattice parameter than would be possible in section or projection topography.

These laboratory techniques have been complemented by the relatively new method of synchrotron radiation topography. Tuomi et al. [13] showed that topographs could be obtained by exposing a crystal to a beam of synchrotron radiation and recording the intensity distribution across the diffracted beam. The whole field has been reviewed recently by Bowen [14].

Electrons moving in a circular path will emit radiation which is plane polarised in the plane of the orbit and is a continuous spectrum, extending from the hard X-ray to the microwave region. Such radiation is called *synchrotron radiation*. For electrons moving at highly relativistic speeds, the radiation is seen in the laboratory frame as a cone, tangential to the electron orbit.

Fig. 1.7 illustrates schematically the *storage ring source* (S.R.S.), used to generate synchrotron radiation, at SERC's Daresbury laboratory. Electrons are injected from a 10 MeV linear accelerator into a 600 MeV booster. From there, the electrons are fed into the main ring in bunches, in time with a radio-frequency accelerating field. The electrons are constrained to move in a roughly circular path by bending magnets arranged around the storage ring. The path of the electrons is, in fact, polygonal, with a magnet at each apex, in order to confine the electrons to a closed orbit. Each magnet also provides the radial acceleration of electrons which gives rise to emission of radiation. Several beam lines can be built up within the storage ring, so that radiation can be directed to several different experiments. Energy is continually being lost from the beam through the radiation process. Energy is replaced by the process of the electrons passing through the r.f. field. Since the electrons travel in bunches in the ring, the radiation is pulsed, which can be of great use in the observation of dynamical processes. Successive pulses can be used to generate topographs which will then illustrate the development with time of the sample under study.

An experimental arrangement for obtaining topographs in the Bragg case is illustrated schematically in Fig. 1.8.
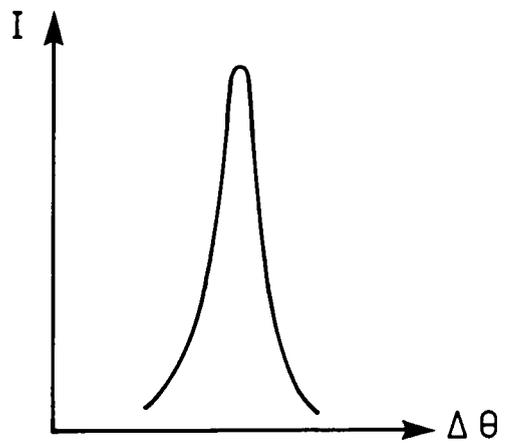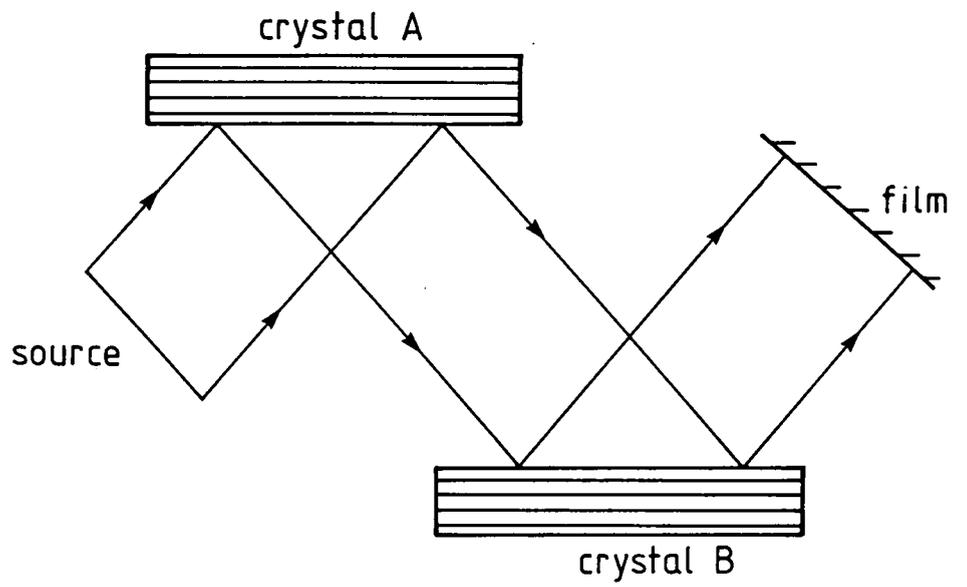
Fig. 1.6: The double-crystal method.
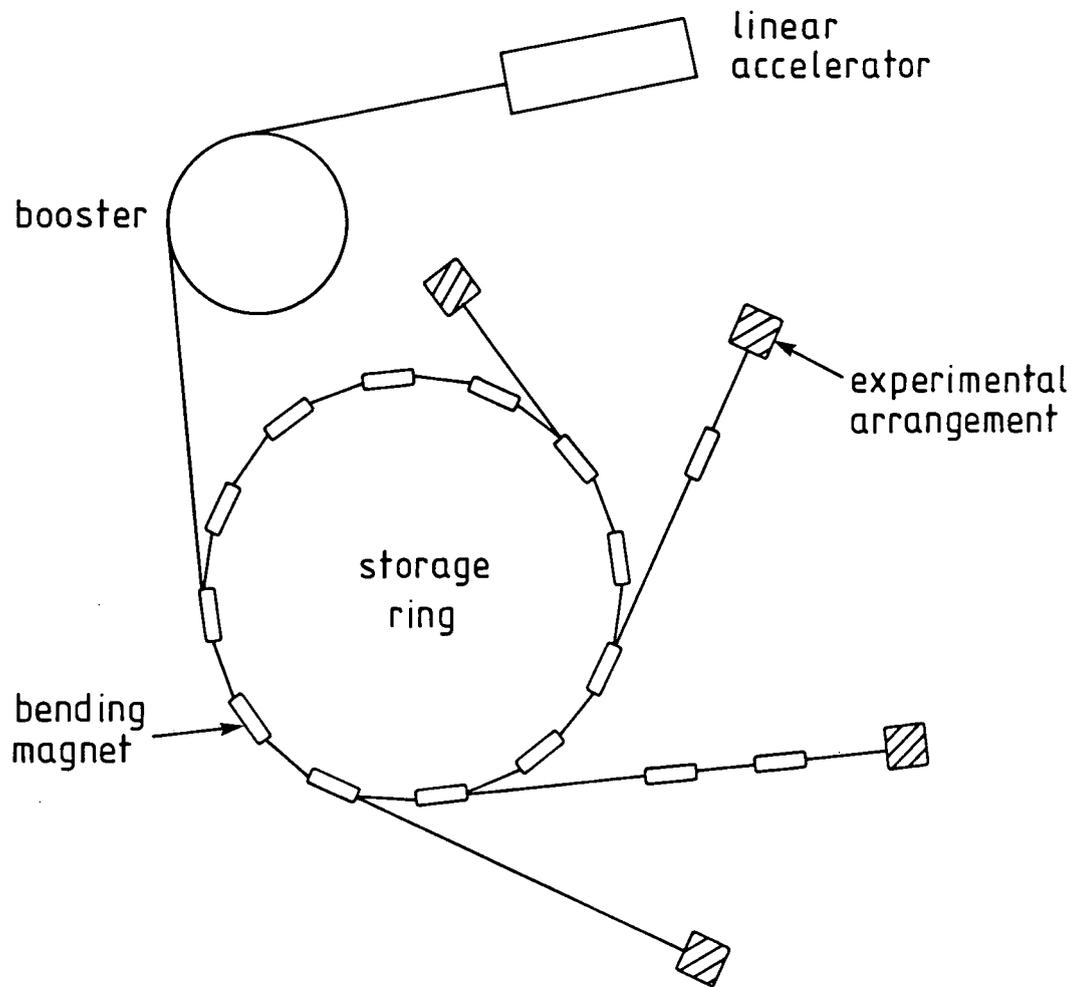
Fig. 1.7: Storage ring source for generation of synchrotron radiation.

film

diffracted
beam

slit

synchrotron
source

sample
crystal

incident
beam
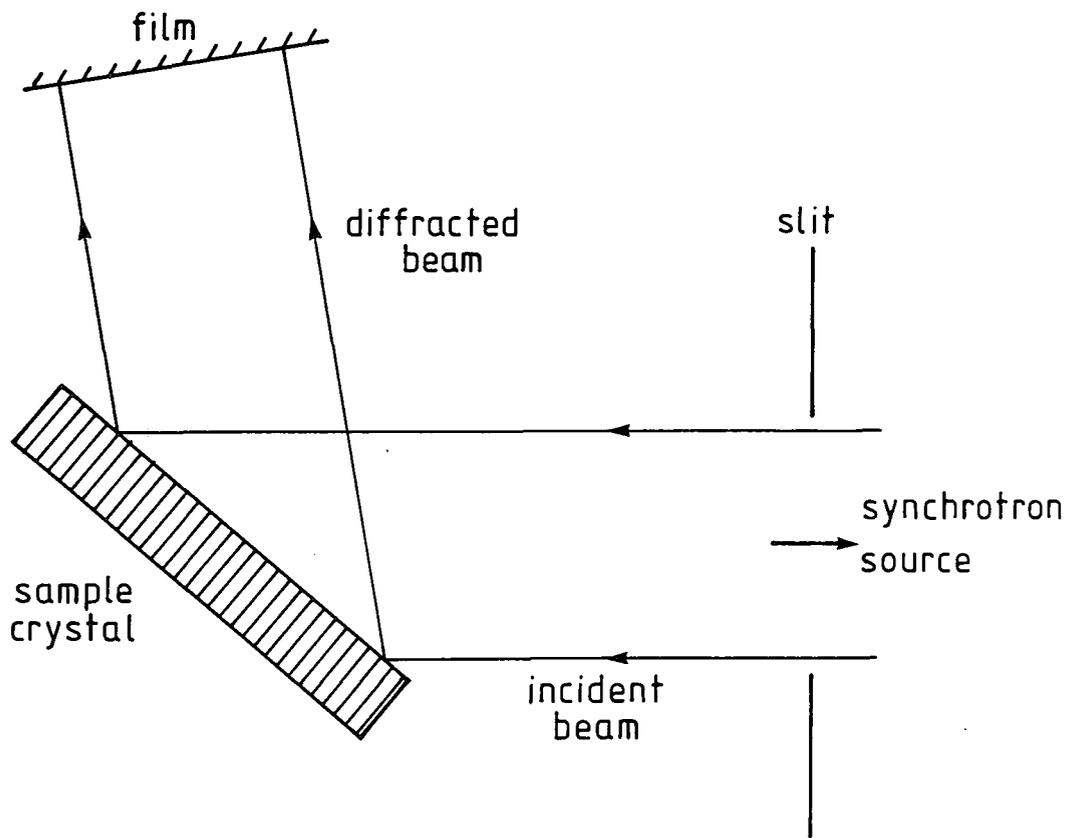
Fig. 1.8: Experimental arrangement for reflection topography using white-beam synchrotron radiation.

Each crystal lattice plane selects a particular wavelength for reflection, and a Laue pattern of spots is obtained on the film. Each 'spot' is in fact a topograph of the crystal, and crystal defects are visible in each such topograph.

Synchrotron topography has numerous advantages over the aforementioned laboratory techniques. Let us look at these, one by one.

First of all, since the incident beam is so wide, the entire crystal can be imaged without using a scanning technique such as projection topography. Clearly, it is then possible to follow defects for their full course after just one exposure.

Synchrotron radiation is very intense, so that exposure times may be of the order of seconds, rather than hours when using conventional techniques. Since the beam divergence is much less in the synchrotron case, the geometrical resolution on a synchrotron topograph is equivalent to that obtained by the Lang method, even though the film can be placed further from the sample in the synchrotron case than in the Lang case. This is a distinct advantage of synchrotron topography, since it allows a large amount of experimental apparatus to be packed around the sample.

Tanner et al. [15] have used synchrotron topography, with its inherent advantages of good resolution and short exposure time, to study magnetic domain wall movements.

Hart [16] has used synchrotron topography to look at grain boundaries in lithium fluoride samples. It was noted that features such as very low angle grain boundaries containing dislocations, and surface scratches, give rise to wider images on synchrotron topographs than on conventional topographs. This indicates that local-strain sensitivity is higher in synchrotron topography than in conventional techniques. By using synchrotron topography, large misoriented regions can be imaged with high local-strain sensitivity. This is not possible in single exposures using conventional techniques.

The various techniques of X-ray topography find considerable use in the semi-conductor industry, where they can be used, together with related methods, to assess crystal quality. This field has been reviewed extensively by Meieran [17].

Since X-ray topography is a non-destructive process, its use in preference to a technique such as destructive etching can save a large amount of money per year. It has already been shown that Lang topography allows easy identification of dislocations in crystals. Of much greater value, from an industrial viewpoint, is the applicability of this technique to the imaging of surface damage. Such damage may be caused either by unintentional handling or by lapping procedures used to produce flat wafers. Precipitates can seriously affect the quality of crystals for use in circuits, and these, too, can be identified using topographic methods. In fact, by using section topography, it is possible to determine the spatial distribution of precipitates. A good indication of the degree of perfection of a crystal is the presence of Pendellösung fringes on the associated topograph. The more perfect a crystal, the greater the visibility of the Pendellösung fringes.

Chapter 2

Dynamical Theory and the Development of the Takagi Equations

In this chapter, we will be concerned with the characterisation of wave propagation in crystals. Whilst the *kinematical theory* is sufficient for small crystals, or crystals in which the scattered amplitude is negligible compared with the incident amplitude, it does not work in cases where the scattering is strong. Hence, we need a theory to take into account multiple scattering and depletion of beam energy. Such a theory is the *dynamical theory in a perfect crystal*. This theory has been comprehensively reviewed by several authors [18,19,20,21]. The objective is to solve Maxwell's Equations in a periodic medium.

We start by writing Maxwell's Equations:

$$\underline{\nabla} \times \underline{E} = \frac{-1}{c} \frac{\partial \underline{B}}{\partial t}, \tag{2.1}$$

$$\text{and} \quad \underline{\nabla} \times \underline{H} = \frac{1}{c} \frac{\partial \underline{D}}{\partial t}. \tag{2.2}$$

$$\text{Now,} \quad \underline{B} = \mu \underline{H},$$
$$\text{and} \quad \underline{D} = \varepsilon \underline{E},$$
$$\text{where} \quad \mu = \text{permeability of medium,}$$
$$\text{and} \quad \varepsilon = \text{permittivity of medium.}$$

Hence, from (2.1):

$$\frac{1}{\varepsilon} \underline{\nabla} \times \underline{D} = \frac{-1}{c} \frac{\partial \underline{B}}{\partial t}$$
$$= \frac{-\mu}{c} \frac{\partial \underline{H}}{\partial t}.$$

Taking the curl of both sides gives:

$$\frac{1}{\varepsilon} \underline{\nabla} \times \underline{\nabla} \times \underline{D} = \frac{-\mu}{c} \frac{\partial}{\partial t} (\underline{\nabla} \times \underline{H}),$$

6

which, from (2.2), becomes:

$$\frac{1}{\varepsilon} \underline{\nabla} \times \underline{\nabla} \times \underline{D} = \frac{-\mu}{c^2} \frac{\partial^2 \underline{D}}{\partial t^2}.$$ (2.3)

For the crystals under consideration, $\mu \cong 1$. Hence,

$$\underline{\nabla} \times \underline{\nabla} \times \frac{1}{\varepsilon} \underline{D} = \frac{-1}{c^2} \frac{\partial^2 \underline{D}}{\partial t^2}.$$

Also, $\varepsilon = 1 + \chi$,

where $\chi =$ dielectric susceptibility.

Then,

$$\frac{1}{\varepsilon} = (1+\chi)^{-1} = 1 + (-1) \cdot \chi + \frac{(-1) \cdot (-2) \cdot \chi^2}{2!} + \cdots$$
$$\simeq 1 - \chi, \text{for } |\chi| \ll 1.$$

Hence, (2.3) becomes:

$$\underline{\nabla} \times \underline{\nabla} \times (1-\chi)\underline{D} = \frac{-1}{c^2} \frac{\partial^2 \underline{D}}{\partial t^2}.$$ (2.4)

Furthermore, susceptibility can be expanded as a Fourier series, reflecting the periodic structure of the crystal lattice, so that:

$$\chi = \sum_h \chi_h \exp(2\pi i \underline{h} \cdot \underline{r}),$$ (2.5)

where $\chi_h = \frac{-e^2 \lambda^2}{\pi m c^2 V} F_h,$ (2.6)

where $e =$ electronic charge,

$\lambda =$ wavelength,

$m =$ electron mass,

$c =$ velocity of light,

$V =$ unit cell volume,

and $F_h =$ structure factor.

The solutions of (2.4) can be expressed as Bloch waves:

$$\underline{D} = \sum_h \underline{D}_h \exp(-2\pi i \underline{k}_h \cdot \underline{r}),$$ (2.7)

where the wavevectors, $\underline{k}_h$, are linked by the relation:

$$\underline{k}_h = \underline{k}_o + \underline{h},$$

where $\underline{h}$ is a reciprocal lattice vector. Substituting (2.7) and (2.5) into (2.4) gives:

$$\sum_g \left\{ \chi_{h-g}(\underline{k}_h.\underline{D}_g)\underline{k}_h - \chi_{h-g}(\underline{k}_h.\underline{k}_h)\underline{D}_g \right\} = (k^2 - \underline{k}_h.\underline{k}_h)\underline{D}_h, \qquad (2.8)$$

where $k = |\underline{k}|$ and $\underline{k}$ = wavevector in vacuum.

Equations (2.8) are the general equations of dynamical theory.

Consider a sphere of radius k, drawn in reciprocal space. Then the condition for Bragg reflection, in the kinematic limit, is that the sphere will cut a reciprocal lattice point and the origin. Now, for the X-ray case, the curvature of this *Ewald sphere* is large, so that the probability of more than two points being cut by the surface of the sphere is very small. Hence, we only need to consider two beams (Fig. 2.1), one transmitted and one diffracted. In this *two beam* case, equation (2.7) becomes:

$$\underline{D} = \underline{D}_o \exp(-2\pi i \underline{k}_o.\underline{r}) + \underline{D}_h \exp(-2\pi i \underline{k}_h.\underline{r}). \qquad (2.9)$$

Also, equations (2.8) reduce to:

$$\alpha_o \alpha_h = \frac{1}{4} k^2 C^2 \chi_h \chi_{\bar{h}}, \qquad (2.10)$$

$$\text{where} \quad \alpha_o = \frac{1}{2k} \left\{ \underline{k}_o.\underline{k}_o - k^2(1 + \chi_o) \right\},$$

$$\alpha_h = \frac{1}{2k} \left\{ \underline{k}_h.\underline{k}_h - k^2(1 + \chi_o) \right\},$$

$$C = \begin{cases} 1, \text{ for } \sigma \text{ - polarisation} \\ \cos 2\theta_B, \text{ for } \pi \text{ - polarisation}, \end{cases}$$

$$\theta_B = \text{ Bragg angle},$$

and χ_h, $\chi_{\bar{h}}$ are the susceptibilities in the direction of the reciprocal lattice vector, and in the direction opposite to the reciprocal lattice vector, respectively.

Equation (2.10) is the equation of the *dispersion surface*, and is the fundamental equation linking $\underline{k}_o$ and $\underline{k}_h$ in the crystal. Each wavevector within the crystal must lie with its tail on the dispersion surface. We can represent the dispersion surface as follows. First of all, we draw two spheres of radius k, one about point O and one about point H, as in Fig. 2.2. The point of intersection, L, is called the *Laue point*. Next, we draw two spheres of radius nk, where n is the refractive index, which represent points corresponding to waves far from the exact Bragg condition. Fig. 2.3 shows a magnification of the two spheres in the region of intersection. AB and $A'B'$ are arcs of the spheres of radius k, and CD and $C'D'$ are arcs of the spheres of radius nk. The *tie-point*, P, is the position of a point corresponding to an allowed pair of wavelengths. The corresponding wavevectors are $\overrightarrow{PO}$ and $\overrightarrow{PH}$. α_o and α_h, from equation (2.10), are in fact the perpendicular distances from the tie-point to the spheres CD and $C'D'$, respectively. The equation of the dispersion surface is a hyperboloid of revolution about OH, and its projection onto the plane of the paper is a hyperbola. This hyperbola is split into
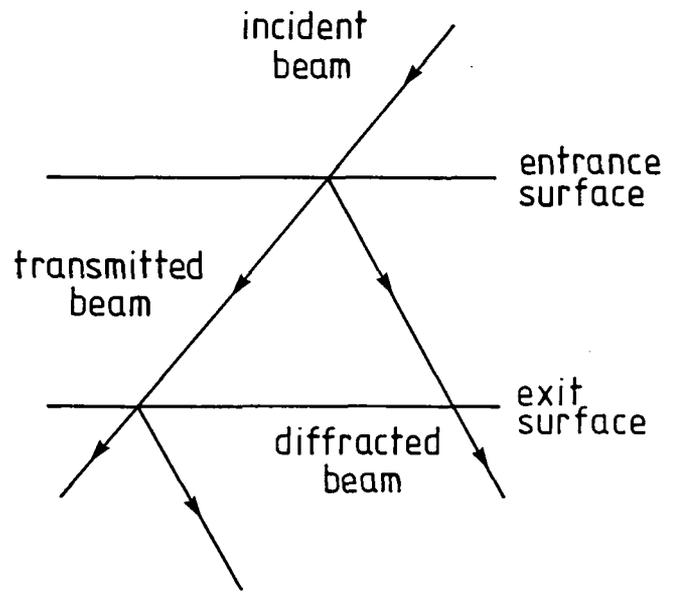
Fig. 2.1:   The two beam case.
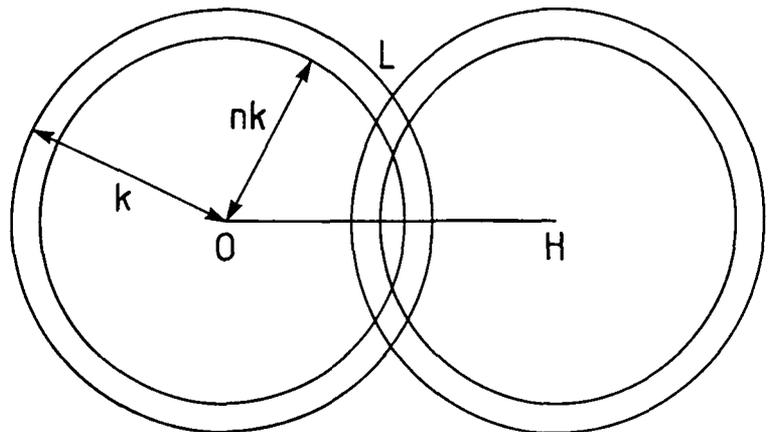
Fig. 2.2:   Spheres in reciprocal space about lattice
points O and H.
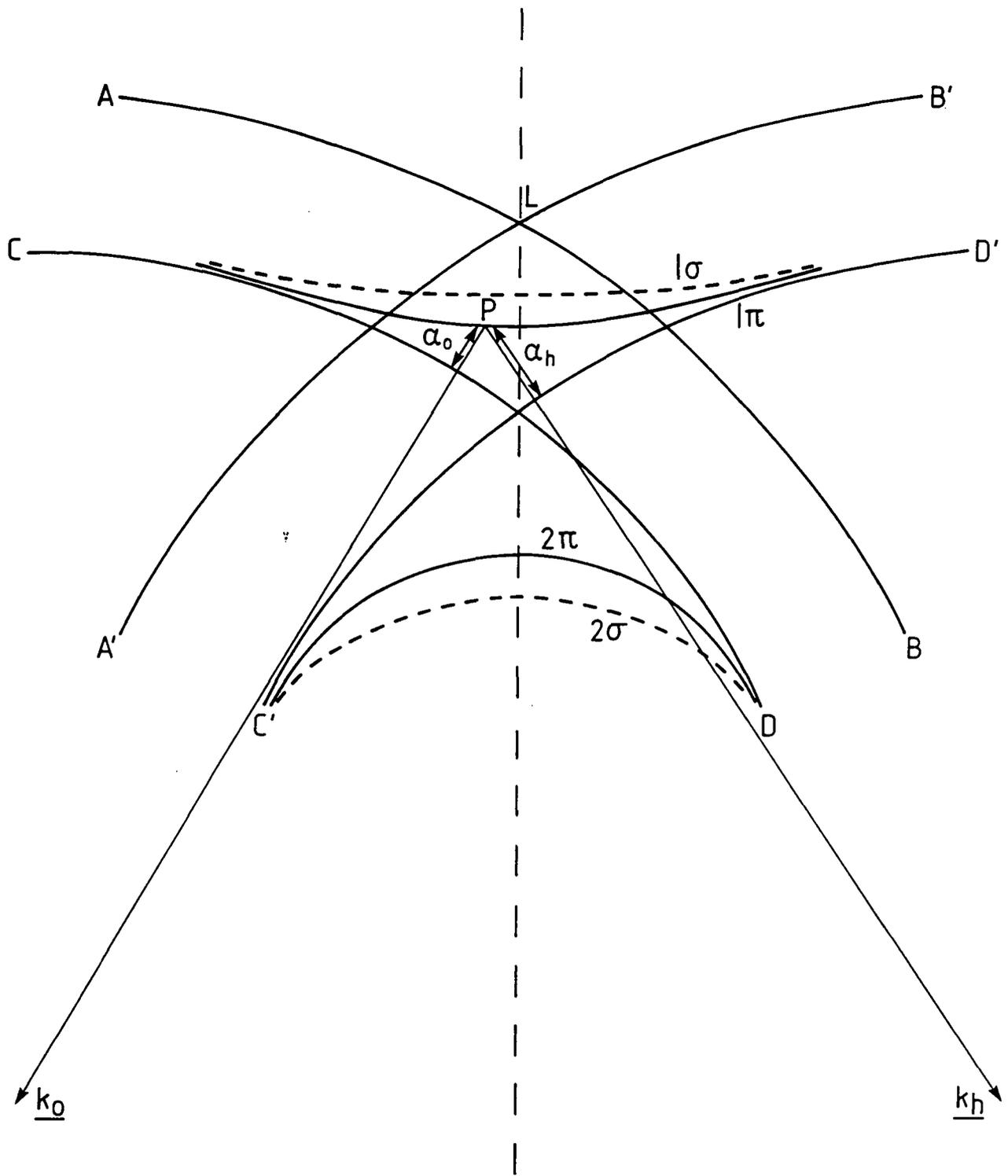
Fig. 2.3: The dispersion surface construction,
(after Tanner).

two branches, labelled 1 and 2. The two branches of the hyperbola are each split into two parts, one corresponding to σ- and one corresponding to π- polarisation. σ-polarisation is the case in which polarisation is perpendicular to the plane of incidence, whilst π-polarisation is parallel to it.

The importance of the dispersion surface will now be seen. Each point on the dispersion surface determines not only the allowed wavevectors, but also the amplitude ratio of the component plane waves in the Bloch wave. Furthermore, it can be shown that the direction of energy flow is perpendicular to the dispersion surface.

One of the most important phenomena described by dynamical theory is the *Pendellösung effect* [5]. This effect results from interference between Bloch waves associated with opposite branches of the dispersion surface. Such Bloch waves have different tie-points, and so different wavevectors, and so different velocities. The fact that the Bloch waves have different velocities leads to the alternate bright and dark fringes seen in wedge-shaped crystals and in section topographs.

Consider a plane wave, of unit amplitude, incident on the entrance surface of a crystal (Fig. 2.4).

The boundary conditions are:

$$1 = D_{o_1} + D_{o_2}$$
$$0 = D_{h_1} + D_{h_2} \qquad (2.11)$$

The amplitude ratio, $R_i = \frac{D_{h_i}}{D_{o_i}}$, where $i = 1$ or 2 denotes the branch of the dispersion surface, is given by:

$$\frac{D_{h_i}}{D_{o_i}} = \eta \pm (1 + \eta^2)^{\frac{1}{2}}, \qquad (2.12)$$

where $\quad \eta \quad = \quad$ deviation parameter, and is a measure of the angular deviation from the exact Bragg condition.

The plus sign in (2.12) is for branch 1 and the minus sign is for branch 2.
Let $\eta = \cot \beta$.
Then, to satisfy (2.11) and (2.12):

$$\begin{array}{ll} D_{o_1} = \cos^2 \frac{\beta}{2} & D_{o_2} = \sin^2 \frac{\beta}{2} \\ D_{h_1} = -\sin \frac{\beta}{2} \cos \frac{\beta}{2} & D_{h_2} = \sin \frac{\beta}{2} \cos \frac{\beta}{2} \end{array} \qquad (2.13)$$

If the crystal has thickness t, then at the exit surface the Bloch waves have additional phase factors:

$$D_i(t) = D_{o_i} \exp(-2\pi i t \underline{k}_{o_i} . \underline{\hat{n}}) + D_{h_i} \exp(-2\pi i t \underline{k}_{h_i} . \underline{\hat{n}}). \qquad (2.14)$$

In (2.14), D_{o_i} and D_{h_i} are the components at the entrance surface and $\underline{\hat{n}}$ is the unit vector perpendicular to the surface.

incident
beam

transmitted
beam

θ_B θ_B

$\underline{S_0}$ $\underline{S_h}$

Bragg
plane
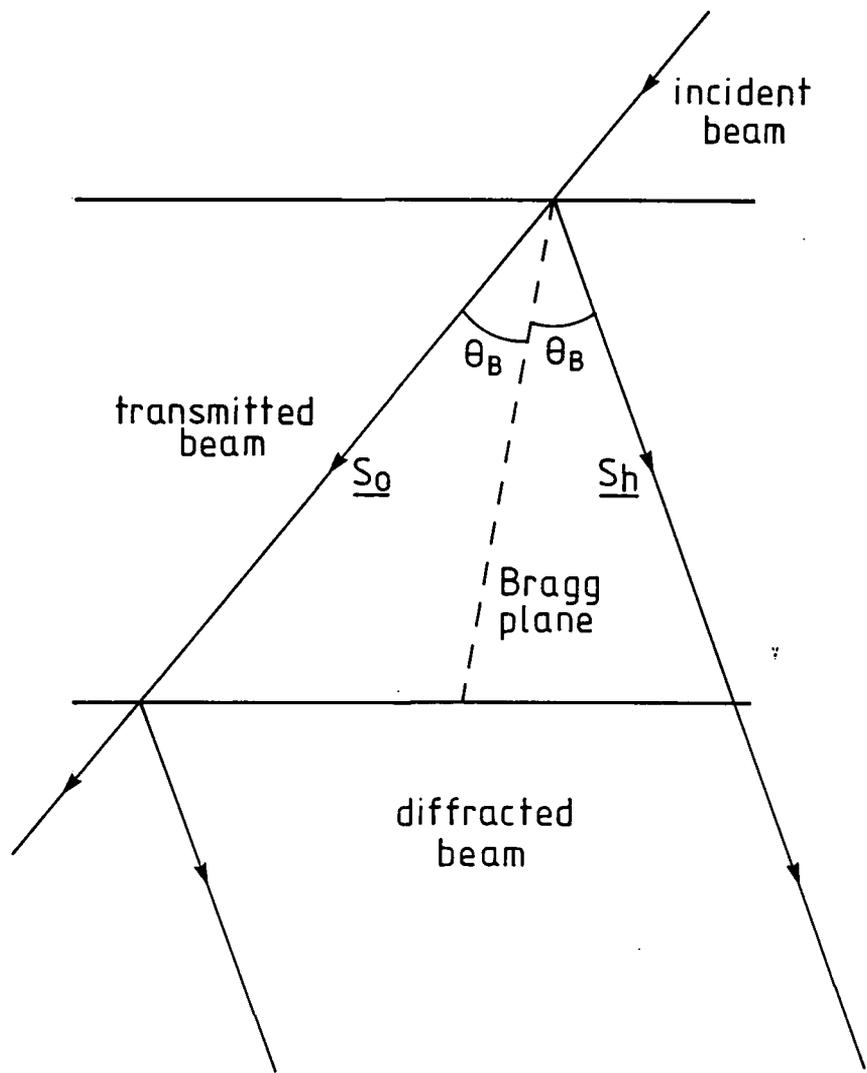
diffracted
beam

θ_B = Bragg angle

$\underline{S_0}, \underline{S_h}$ are unit vectors in the transmitted and
diffracted directions, respectively.

Fig. 2.4:   Diffraction geometry for a plane wave
incident upon a crystal.

At the exit surface, the boundary conditions are:

$$
\begin{aligned}
D_o^e &= D_{o_1}(t) + D_{o_2}(t) \\
D_h^e &= D_{h_1}(t) + D_{h_2}(t)
\end{aligned}
\tag{2.15}
$$

The intensity, I_h, in the diffracted beam is given by

$$
\begin{aligned}
I_h &= D_h^{e*} D_h^e = \\
&\quad \{D_{h_1}\exp(2\pi i t \underline{k}_{h_1}.\hat{n}) + D_{h_2}\exp(2\pi i t \underline{k}_{h_2}.\hat{n}\} \times \\
&\quad \{D_{h_1}\exp(-2\pi i t \underline{k}_{h_1}.\hat{n}) + D_{h_2}\exp(-2\pi i t \underline{k}_{h_2}.\hat{n}\} \\
&= D_{h_1}^2 + D_{h_2}^2 + D_{h_1}D_{h_2}\{\exp[2\pi i t(\underline{k}_{h_2} - \underline{k}_{h_1}).\hat{n}] + \exp[-2\pi i t(\underline{k}_{h_2} - \underline{k}_{h_1}).\hat{n}]\} \\
&= D_{h_1}^2 + D_{h_2}^2 + 2D_{h_1}D_{h_2}\cos[2\pi t(\underline{k}_{h_2} - \underline{k}_{h_1}).\hat{n}].
\end{aligned}
$$

Substituting for D_{h_1} and D_{h_2}, from (2.13), gives

$$
\begin{aligned}
I_h &= 2\sin^2\frac{\beta}{2}\cos^2\frac{\beta}{2} - 2\sin^2\frac{\beta}{2}\cos^2\frac{\beta}{2}\cdot\cos[2\pi t(\underline{k}_{h_2} - \underline{k}_{h_1}).\hat{n}], \\
I_h &= \frac{1}{2}\sin^2\beta\{1 - \cos[2\pi t(\underline{k}_{h_2} - \underline{k}_{h_1}).\hat{n}]\}.
\end{aligned}
\tag{2.16}
$$

Equation (2.16) shows that there is interference between the components of the Bloch waves associated with opposite branches of the dispersion surface, and that this interference depends on depth. The interference beat is proportional to $(\underline{k}_{h_2} - \underline{k}_{h_1})$, the difference in wavevectors.

Using the relation

$$
(\underline{k}_{h_2} - \underline{k}_{h_1}).\hat{n} = \Lambda_o(1 + \eta^2)^{\frac{1}{2}},
$$

where Λ_o = diameter of dispersion surface, and substituting for β, we obtain:

$$
I_h = \frac{\sin^2[\pi\Lambda_o t(1 + \eta^2)^{\frac{1}{2}}]}{1 + \eta^2},
\tag{2.17}
$$

$$
I_o = 1 - \frac{\sin^2[\pi\Lambda_o t(1 + \eta^2)^{\frac{1}{2}}]}{1 + \eta^2}.
\tag{2.18}
$$

(2.17) and (2.18) show that the intensity of both transmitted and diffracted beams varies periodically with crystal thickness. The period is the same for both beams and is given by a depth

$$
[\Lambda_o(1 + \eta^2)^{\frac{1}{2}}]^{-1}.
$$

This has a maximum value at $\eta = 0$, i.e. the exact Bragg condition. In this case, the depth corresponding to one period is known as the *extinction distance*, ξ_g. The extinction distance is then given by:

$$
\xi_g = \Lambda_o^{-1}.
$$

For values of $\eta \neq 0$, the effective extinction distance is:

$$\xi_g' = \frac{\xi_g}{(1 + \eta^2)^{\frac{1}{2}}}.$$

Also, it is seen that the intensities of the transmitted and diffracted beams are complementary. Photographic plates placed in the two beams will show reversed contrast.

The Pendellösung fringes seen in X-ray topographs are very similar to the parallel bright and dark bands observed much earlier in electron micrographs [22]. This similarity illustrates the fact that the processes of X-ray diffraction and electron diffraction are closely related. In fact, as will be shown, the two processes can be described by the same set of equations.

Several theories were proposed in the late 1950s and early 1960s to account for the process of electron diffraction in a distorted crystal. Cowley and Moodie [23,24] proposed a *lamellar theory*, in which the crystal is divided into a set of thin sheets or *lamellae*, parallel to the surface. The relation between wave functions at successive boundary surfaces of the lamellae can be derived, and these relations can be used iteratively to calculate the wave function at the exit surface. Hirsch, Howie and Whelan [25] devised a theory based on the *column approximation*, in which a lamellar crystal is divided again into columns perpendicular to the lamellae. The columns must be sufficiently thin that any part of each lamella within a column can be considered perfect. The theory is then applied to each column individually, to obtain the wave function at the exit surface. Howie and Whelan [26,27] used this theory to calculate electron micrographs due to dislocations in crystals.

Probably the most successful theory, developed independently by Takagi [28,29] and Taupin [30], describes both X-ray and electron diffraction for distorted and perfect crystals.

Previously, the wave field inside the crystal was given by relation (2.7) as a Fourier series:

$$\underline{D}(\underline{r}) = \sum_h \underline{D}_h \exp(-2\pi i \underline{k}_h.\underline{r}).$$

In the above equation, the Fourier components, $\underline{D}_h$, are constant.

Takagi suggested that the $\underline{D}_h$ be allowed to vary slowly with position. It is then possible to take into account variations in the wave field induced by distortion of the crystal.

As a first step, Takagi wrote down the wave function in a distorted crystal as a new Fourier series:

$$\psi(\underline{r}) = \sum_g \psi_g(\underline{r}) \exp(-2\pi i \underline{k}_g.\underline{r}), \tag{2.19}$$

where $\underline{k}_g = \underline{k}_o + \underline{g}$,

and $\underline{g}$ is a reciprocal lattice vector.

It is more convenient to express (2.19) in the form:

$$\psi(\underline{r}) = \sum_g \psi'_g(\underline{r}) \exp[-2\pi i S_g(\underline{r})], \qquad (2.20)$$

where

$$S_g(\underline{r}) = \underline{k}_g \cdot \underline{r} - \underline{g} \cdot \underline{u}(\underline{r}_o). \qquad (2.21)$$

In (2.21), $\underline{u}(\underline{r})$ is a continuous function of position, representing the displacement of the atom at point $\underline{r}$, and $\underline{r}_o$ is the position vector of the point occupied originally by the atom, before it was displaced to point $\underline{r}$ by the distortion.

Hence,

$$\underline{r} = \underline{r}_o + \underline{u}(\underline{r}_o). \qquad (2.22)$$

Takagi defined the wavevector $\underline{k}'_g$, such that

$$\underline{k}'_g = \nabla S_g(\underline{r}) = \underline{k}_g - \nabla(\underline{g} \cdot \underline{u}). \qquad (2.23)$$

He showed that it is possible to define a local reciprocal lattice vector, $\underline{g}'$, in the vicinity of point $\underline{r}$, in the distorted crystal, such that

$$\underline{g}' = \underline{g} - \nabla[\underline{g} \cdot \underline{u}(\underline{r}_o)]. \qquad (2.24)$$

Hence, from (2.23) and (2.24),

$$\underline{k}'_g = \underline{k}_o + \underline{g}'. \qquad (2.25)$$

One effect of allowing ψ_g and ψ'_g to vary with position is that any slight change, $\Delta\underline{k}_o$, in $\underline{k}_o$ can be compensated for by multiplying $\psi_g(\underline{r})$ or $\psi'_g(\underline{r})$ by a factor $\exp(2\pi i \Delta\underline{k}_o \cdot \underline{r})$, without affecting their spatial variation. This holds so long as $\Delta\underline{k}_o$ is sufficiently small compared with any reciprocal lattice vector. Hence, a value of $\underline{k}_o$ must be fixed initially, and so we take

$$\mid \underline{k}_o \mid = nk = n \mid \underline{k} \mid, \qquad (2.26)$$

where n = refractive index,
and $\underline{k}$ = wavevector in vacuum.

Takagi introduced a quantity called the *crystalline field*, $\chi(\underline{r})$, which is defined:

$$\text{(a) in the electron case,} \quad \chi_e(\underline{r}) = \frac{V(\underline{r})}{E} \qquad (2.27)$$

where $V(\underline{r})$ = electrostatic potential in crystal and E = accelerating voltage of incident electron,

$$\text{(b) in the X-ray case,} \quad \chi_x(\underline{r}) = \frac{-e^2\lambda^2}{\pi mc^2} \cdot n(\underline{r}) \qquad (2.28)$$

where e = electronic charge,
λ = wavelength
e = electron mass,
c = velocity of light,
and $n(\underline{r})$ = density of electrons at $\underline{r}$.

12

For a perfect crystal, $\chi(\underline{r})$ is given by a Fourier series:

$$\chi(\underline{r}) = \sum_g \chi_g \exp(-2\pi i \underline{g}.\underline{r}). \tag{2.29}$$

However, the value of χ in the distorted crystal, $\chi'(\underline{r})$, is equal to the value of χ at the corresponding point $\underline{r}_o$, see equation (2.22), in the perfect crystal:

$$\chi'(\underline{r}) = \chi[\underline{r} - \underline{u}(\underline{r}_o)]. \tag{2.30}$$

Substituting (2.29) into (2.30) gives:

$$\chi'(\underline{r}) = \sum_g \chi_g \exp[-2\pi i(\underline{g}.\underline{r} - \underline{g}.\underline{u})]. \tag{2.31}$$

The next step is to consider electrons and X-rays separately, and, for each, to derive an equation describing their propagation in a crystal.

2.1 Electron Diffraction

The Schrödinger Equation for an electron in an electrostatic potential $V(\underline{r})$, given by (2.27), can be written

$$\nabla^2 \psi(\underline{r}) + 4\pi^2 k^2[1 + \chi'(\underline{r})]\psi(\underline{r}) = 0, \tag{2.32}$$

where $\underline{k}$ = wavevector of electron in vacuum.

Substituting (2.20) and (2.31) into (2.32) gives:

$$\sum_g \{\nabla^2 \psi'_g(\underline{r}) + 2\pi i \nabla^2(\underline{g}.\underline{u})\psi'_g(\underline{r}) - 4\pi i[\underline{k}'_g.\underline{\nabla}\psi'_g(\underline{r})]$$

$$+ 4\pi^2[k^2(1 + \chi_o) - \underline{k}_g^2]\psi'_g(\underline{r})$$

$$+ 4\pi^2 k^2 \sum_{g' \neq g} \chi_{g-g'}\psi'_{g'}(\underline{r})\} \cdot \exp[-2\pi i(\underline{k}_g.\underline{r} - \underline{g}.\underline{u})]$$

$$= 0. \tag{2.33}$$

Now, the spatial variation of $\psi'(\underline{r})$ and $(\underline{g}.\underline{u})$ is appreciable only on a scale which is vary large compared to the electron wavelength. Consequently, the first and second terms in the curly brackets in (2.33) can be neglected. The remaining terms are also of such *macroscopic variation* and can thus be taken out of the integration when (2.33) is multiplied by $\exp[2\pi i(\underline{k}_h.\underline{r} - \underline{h}.\underline{u})]$ and integrated with respect to $\underline{r}$ over a unit cell, where $\underline{h}$ is a reciprocal lattice vector.

Performing this integration yields the result:

$$[\underline{k}'_h.\underline{\nabla}\psi'_h(\underline{r})] = -i\pi[k^2(1 + \chi_o) - \underline{k}_h'^2]\psi'_h(\underline{r}) - i\pi k^2 \sum_{h' \neq h} \chi_{h-h'}\psi'_{h'}(\underline{r}). \tag{2.34}$$

For strong reflections, $k \cong |\underline{k}'_h|$, and so dividing through (2.34) by k gives:

$$[\underline{S}_h.\underline{\nabla}\psi'_h(\underline{r})] = i2\pi k \beta'_h(\underline{r})\psi'_h(\underline{r}) - i\pi k \sum_{h' \neq h} \chi_{h-h'}\psi'_{h'}(\underline{r}), \tag{2.35}$$

13

where $\underline{S}_h$ is the unit vector in the direction of $\underline{k}_h$, and

$$\beta_h' = \beta_h - \frac{1}{k}\frac{\partial}{\partial S_h}[\underline{h}.\underline{u}(\underline{r})], \tag{2.36}$$

$$\text{where} \quad \beta_h = \frac{|\underline{k}_h|^2 - |\underline{k}_o|^2}{2k^2}.$$

Equation (2.35) is the fundamental equation describing the process of electron diffraction in a crystal. It includes the equations derived from lamellar theories as a special case.

2.2 X-ray Diffraction

A wave equation for the electric displacement, $\underline{D}$, induced by X-rays in a crystalline medium is:

$$\nabla^2\underline{D} + 4\pi^2 k^2\underline{D} + 4\pi\underline{\nabla} \times \underline{\nabla} \times \underline{P} = 0, \tag{2.37}$$

where $\underline{k}$ = wavevector of X-rays in vacuum, and $\underline{P}$ = electric polarisation, given by:

$$4\pi\underline{P} = \chi'\underline{D}, \tag{2.38}$$

where χ' is 4π times the polarisability of the crystal given by (2.28). The prime on χ' indicates that it refers to a distorted crystal.

$\underline{D}$ can be expressed as a Fourier series, either in a form analogous to (2.19), i.e.

$$\underline{D}(\underline{r}) = \sum_g \underline{D}_g(\underline{r})\exp(-2\pi i\underline{k}_g.\underline{r}), \tag{2.39}$$

or in a form analogous to (2.20), i.e.

$$\underline{D}(\underline{r}) = \sum_g \underline{D}_g'(\underline{r})\exp[-2\pi i(\underline{k}_g.\underline{r} - \underline{g}.\underline{u})]. \tag{2.40}$$

$\underline{P}$ is expanded similarly as

$$\begin{aligned}\chi'(\underline{r})\underline{D}(\underline{r}) &= 4\pi\underline{P}(\underline{r}) \\ &= 4\pi\sum_g \underline{P}_g'(\underline{r}).\exp[-2\pi i(\underline{k}_g.\underline{r} - \underline{g}.\underline{u})],\end{aligned} \tag{2.41}$$

where $\underline{P}_g'(\underline{r})$ is given by:

$$4\pi\underline{P}_g'(\underline{r}) = \sum_{g'}\chi_{g-g'}(\underline{r})\underline{D}_{g'}'(\underline{r}). \tag{2.42}$$

After some manipulation, it is found that:

$$\begin{aligned}\underline{\nabla} \times \underline{\nabla} \times \underline{P} &= -4\pi^2\sum_g[\underline{k}_g \times [\underline{k}_g \times \underline{P}_g']] \\ &\qquad \times \exp[-2\pi i(\underline{k}_g.\underline{r} - \underline{g}.\underline{u})]\end{aligned} \tag{2.43}$$

14

and

$$\nabla^2 \underline{D} = \sum_g \{ -4\pi i(\underline{k}'_g.\underline{\nabla})\underline{D}'_g - 4\pi^2 \underline{k}'^2_g \underline{D}'_g \}$$
$$\times \exp[-2\pi i(\underline{k}_g.\underline{r} - \underline{g}.\underline{u})]. \tag{2.44}$$

Substituting (2.43) and (2.44) into (2.37) gives:

$$\sum_g \{ -4\pi i(\underline{k}_g.\underline{\nabla})\underline{D}'_g + 4\pi^2(k^2 - \underline{k}'^2_g)\underline{D}'_g$$
$$+ 4\pi^2 \sum_{g'} \chi_{g-g'}[\underline{D}'_{g'}]_g \}. \exp[-2\pi i(\underline{k}_g.\underline{r} - \underline{g}.\underline{u})]$$
$$= 0, \tag{2.45}$$

$$\text{where} \quad [\underline{D}'_{g'}]_g = \frac{-1}{|\underline{k}'_g|^2}[\underline{k}'_g \times [\underline{k}'_g \times \underline{D}'_{g'}]] \tag{2.46}$$

and denotes the component vector of $\underline{D}'_{g'}$ perpendicular to $\underline{k}_g$.

Multiplication by $\exp[2\pi i(\underline{k}_h.\underline{r} - \underline{h}.\underline{u})]$ and integration with respect to $\underline{r}$ over a unit cell, similar to the deduction of (2.35) from (2.33), gives:

$$(\underline{S}_h.\underline{\nabla})\underline{D}'_h = i2\pi k\beta'_h\underline{D}'_h - i\pi k \sum_{h' \neq h} \chi_{h-h'}[\underline{D}'_{h'}]_h. \tag{2.47}$$

Equation (2.47) is the fundamental equation describing the process of X-ray diffraction in a crystal.

For the two beam case, Takagi showed that (2.35) and (2.47) reduce to a set of two equations. There are three distinct cases:

1. the electron case,

2. the X-ray case where both $\underline{D}'_o$ and $\underline{D}'_h$ are perpendicular to the plane of incidence, defined by $\underline{k}_o$ and $\underline{k}_h$, and

3. the X-ray case where both $\underline{D}'_o$ and $\underline{D}'_h$ are parallel to the plane of incidence.

The fundamental equations, (2.35) and (2.47), then reduce to:

$$\frac{\partial \psi'_o}{\partial S_o} = -i\pi k C \chi_{\bar{h}} \psi'_h$$
$$\frac{\partial \psi'_h}{\partial S_h} = -i\pi k C \chi_h \psi'_o + i2\pi k \beta'_h \psi'_h, \tag{2.48}$$

$$\text{where} \quad C = \begin{cases} 1, \text{ for cases 1 and 2} \\ \cos 2\theta_B, \text{ for case 3.} \end{cases}$$

ψ'_o and ψ'_h stand, respectively, for $\underline{D}'_o$ and $\underline{D}'_h$ in the X-ray case. Hence, the fundamental equations describing X-ray diffraction in a crystal are:

$$\frac{\partial \underline{D}'_o}{\partial S_o} = -i\pi k C \chi_{\bar{h}} \underline{D}'_h$$

$$\frac{\partial \underline{D}'_h}{\partial S_h} = -i\pi k C \chi_h \underline{D}'_o + i2\pi k \beta'_h \underline{D}'_h. \qquad (2.49)$$

Equations (2.49) are based upon expansion (2.40). If expansion (2.39) were used instead, then we would get the analogous equations for the $\underline{D}_h$:

$$\frac{\partial \underline{D}_o}{\partial S_o} = -i\pi k C \chi_{\bar{h}}' \underline{D}_h$$

$$\frac{\partial \underline{D}_h}{\partial S_h} = -i\pi k C \chi'_h \underline{D}_o + i2\pi k \beta_h \underline{D}_h, \qquad (2.50)$$

$$\text{where} \quad \chi_{\bar{h}}' = \chi_{\bar{h}} \exp[-2\pi i(\underline{h}.\underline{u})],$$

$$\chi'_h = \chi_h \exp[2\pi i(\underline{h}.\underline{u})],$$

$$\text{and} \quad \beta_h = \beta'_h + \frac{1}{k}\frac{\partial}{\partial S_h}(\underline{h}.\underline{u}).$$

The partial equations (2.49) and (2.50) are generalised forms of the corresponding set of ordinary differential equations given by Howie and Whelan [26].

Chapter 3

Simulation Techniques

Analytical solutions of Takagi's equations have been obtained for a perfect, unbent crystal in the Laue case [29] and the Bragg case [31], and for a perfect crystal subject to a uniform strain gradient [32,33]. These are not of practical relevance to this project, where it is crystals with defects which are of interest.

We use here an alternative approach, that of numerically integrating Takagi's equations (2.49). A computer program, based on that of Epelboin [34], has been developed by Green [35] to work out the intensity distribution of the diffracted beam striking the photographic film. The program takes into account the photographic recording process and enables an output device to display a simulation of the experimental topograph. By varying the physical parameters contained within the simulation program, different simulated topographs can be obtained. Hence, by matching experimental and simulated images, it is possible to determine the physical characteristics of the defect which gives rise to the experimental image. This method has been comprehensively reviewed by Epelboin [34.]

Following Authier et al. [36], we now consider how it is possible to numerically integrate Takagi's equations.

Consider a point, P, on the exit surface of a crystal, Fig. 3.1. The wave amplitudes D_o and D_h at P are determined by the interactions of the wavefields in the triangle ABP. This triangle is split by two sets of *characteristic lines*, parallel to the S_o and S_h directions. The point of intersection of two characteristic lines is called a *node*. The step lengths between two nodes, in the S_o and S_h directions, are p and q respectively. The aim of the following derivation is to obtain an iterative algorithm for calculating D_o and D_h at all nodes in the network.

Consider a function $F(f,x) = \frac{df}{dx}$, where f is an unknown function and x is the independent variable.

From Fig. 3.2, the gradient of the straight line AC is approximately equal to the gradient of the curve at B. Hence:

$$\left(\frac{\partial f}{\partial x}\right)_{x+\frac{p}{2}} \approx \frac{f(x+p) - f(x)}{p},$$

17
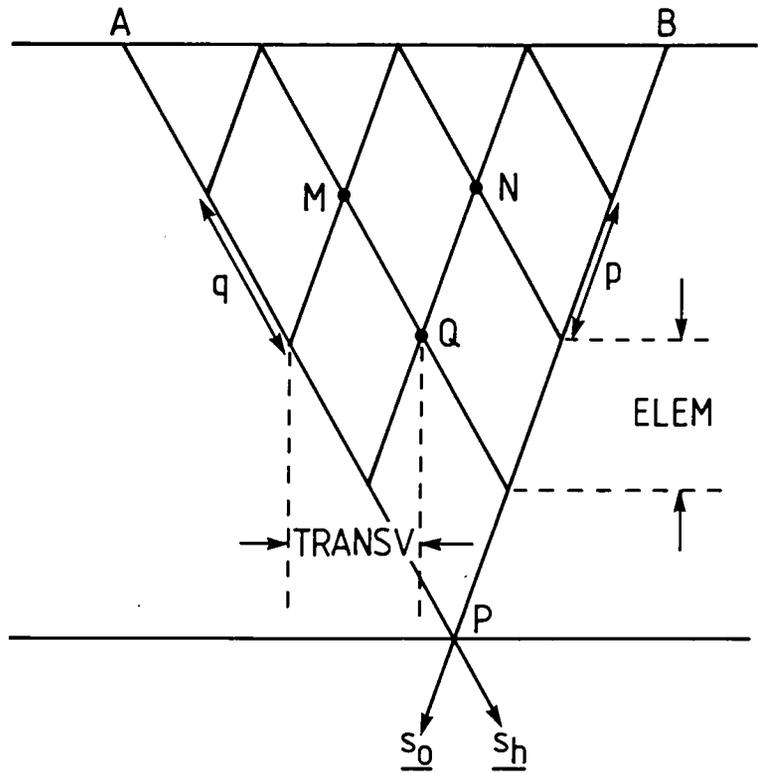
Fig. 3.1:   Network of nodes in a crystal.
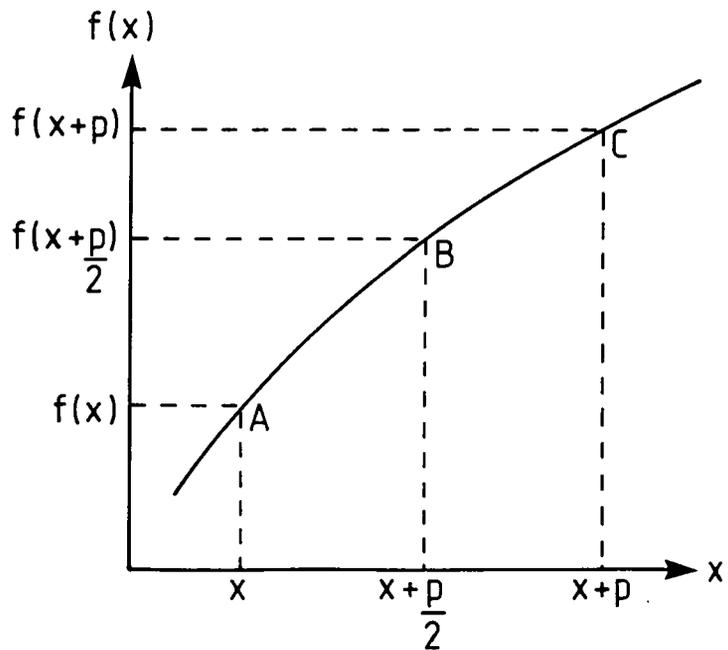
Fig. 3.2:   Representation of the variation of
f(x) with x.

so that

$$f(x + p) \approx f(x) + p \left(\frac{\partial f}{\partial x}\right)_{x + \frac{p}{2}}. \qquad (3.1)$$

Consider Takagi's equations (2.49):

$$\frac{\partial D'_o(r)}{\partial S_o} = -i\pi k C \chi_{\bar{h}} D'_h(r) \qquad \ldots (a)$$
$$\frac{\partial D'_h(r)}{\partial S_h} = -i\pi k C \chi_h D'_o(r) + 2i\pi k \beta'_h D'_h(r) \qquad \ldots (b)$$

$$(3.2)$$

First of all, we use $C = 1$, since we only consider σ-polarised waves. Multiplying equation (3.2a) by p and (3.2b) by q, removing the primes and using oblique coordinates (S_o, S_h) instead of r, we obtain:

$$p \frac{\partial}{\partial S_o} D_o(S_o, S_h) = 2A D_h(S_o, S_h) \qquad \ldots (a)$$
$$q \frac{\partial}{\partial S_h} D_h(S_o, S_h) = 2B D_o(S_o, S_h) + 2W(S_o, S_h) D_h(S_o, S_h) \qquad \ldots (b)$$

$$(3.3)$$

where

$$A = \frac{-1}{2} i\pi p k \chi_{\bar{h}},$$

$$B = \frac{-1}{2} i\pi q k \chi_h,$$

$$\text{and} \quad W(S_o, S_h) = i\pi q k \beta'_h.$$

Extending relation (3.1) to S_o, S_h, we obtain:

$$p \frac{\partial}{\partial S_o} D_o(S_o - \frac{p}{2}, S_h) = D_o(S_o, S_h) - D_o(S_o - p, S_h)$$

$$q \frac{\partial}{\partial S_h} D_h(S_o, S_h - \frac{q}{2}) = D_h(S_o, S_h) - D_h(S_o, S_h - q).$$

Then, substituting into relations (3.3) gives:

$$D_o(S_o, S_h) = D_o(S_o - p, S_h) + 2A D_h(S_o - \frac{p}{2}, S_h) \qquad \ldots (a)$$
$$D_h(S_o, S_h) = D_h(S_o, S_h - q) + 2B D_o(S_o, S_h - \frac{q}{2})$$
$$+ 2W(S_o, S_h - \frac{q}{2}) D_h(S_o, S_h - \frac{q}{2}) \qquad \ldots (b)$$

$$(3.4)$$

It is inconvenient to express the amplitudes at points (S_o, S_h) and $(So - \frac{p}{2}, Sh)$. We avoid this by using the following relation, based on the assumption that the amplitudes vary slowly in the Takagi equations:

$$f(x + \frac{p}{2}) = \frac{f(x) + f(x + p)}{2}$$

$$\text{so that} \quad 2f(x + \frac{p}{2}) = f(x) + f(x + p). \qquad (3.5)$$

18

Using (3.5) in equations (3.4) gives:

$$D_o(S_o, S_h) = D_o(S_o - p, S_h) + AD_h(S_o - p, S_h) + AD_h(S_o, S_h) \qquad \ldots \text{(a)}$$
$$\begin{aligned} D_h(S_o, S_h) = {} & D_h(S_o, S_h - q) + BD_o(S_o, S_h - q) \\ & + BD_o(S_o, S_h) + W\left(S_o, S_h - \tfrac{q}{2}\right) D_h(S_o, S_h - q) \\ & + W\left(S_o, S_h - \tfrac{q}{2}\right) D_h(S_o, S_h) \qquad \ldots \text{(b)} \end{aligned}$$

$$(3.6)$$

Obtaining $D_h(S_o, \dot{S}_h)$ from (3.6b) and substituting into (3.6a) gives:

$$\begin{aligned} D_o(S_o, S_h) = {} & E\{C_2 D_o(S_o - p, S_h) + AC_2 D_h(S_o - p, S_h) \\ & + ABD_o(S_o, S_h - q) + AC_1 D_h(S_o, S_h - q)\} \end{aligned} \qquad (3.7)$$

$$\begin{aligned} \text{where} \quad C_1 &= 1 + W, \\ C_2 &= 1 - W, \\ E &= \frac{1}{1 - W - AB}, \\ \text{and} \quad W &= i\pi k q \beta'_h \left(S_o, S_h - \frac{q}{2}\right). \end{aligned}$$

Similarly, substituting for $D_o(S_o, S_h)$ from (3.6a) into (3.6b) gives:

$$\begin{aligned} D_h(S_o, S_h) = {} & E\{BD_o(S_o - p, S_h) + ABD_h(S_o - p, S_h) \\ & + BD_o(S_o, S_h - q) + C_1 D_h(S_o, S_h - q)\}. \end{aligned} \qquad (3.8)$$

Combining (3.7) and (3.8) in matrix form gives:

$$\begin{bmatrix} D_o(S_o, S_h) \\ D_h(S_o, S_h) \end{bmatrix} = E \begin{bmatrix} C_2 & AC_2 & AB & AC_1 \\ B & AB & B & C_1 \end{bmatrix} \begin{bmatrix} D_o(S_o - p, S_h) \\ D_h(S_o - p, S_h) \\ D_o(S_o, S_h - q) \\ D_h(S_o, S_h - q) \end{bmatrix} \qquad (3.9)$$

Equations (3.9) can be used to calculate the amplitudes D_o and D_h of the waves at any point T, Fig. 3.3, given the amplitudes at points R and S, and given the value of the parameter W at point W. Hence, the initial goal of calculating the amplitudes D_o and D_h at all nodes throughout the network can now be realised.

The algorithm (3.9) can be used iteratively within a computer program to calculate the intensity distribution of the diffracted beam across the exit surface of the crystal, and hence the intensity distribution incident upon the recording medium.

It is important to recognise the fact that the wave amplitudes vary rapidly in certain parts of the Borrmann triangle. Consequently, the elementary slab thickness, *ELEM* in Fig. 3.1, must be sufficiently small to accommodate such variations.

In particular, for a spherical incident wave, the amplitude distribution across the diffracted beam is given by the Bessel function J_o. J_o varies rapidly close to
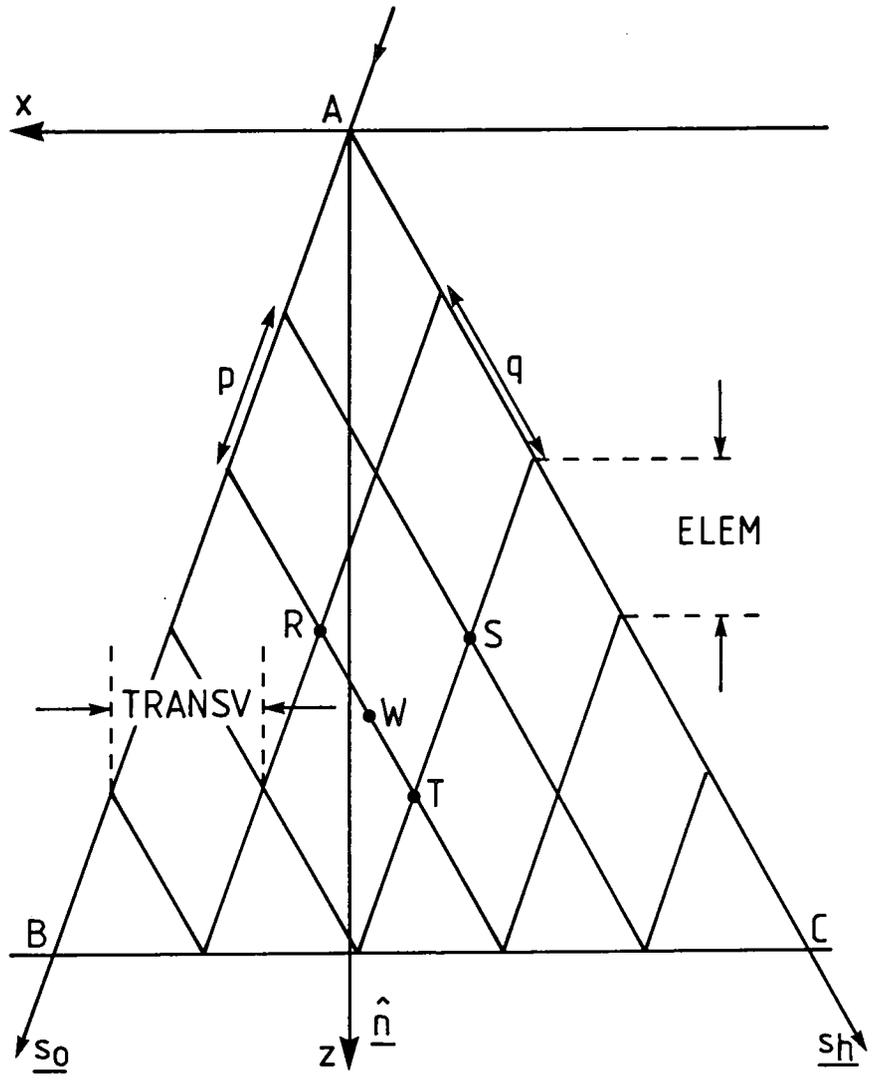
Fig. 3.3: Integration network in the Borrmann fan.

the edges of the Borrmann fan. Fig. 3.4 shows the variation in amplitude of the diffracted wave along a line parallel to the entrance surface.

It is seen that the variation is rapid near the So and Sh directions, and that most of the intensity is contained near the Borrmann fan edges. Thus, if *ELEM* (Fig. 3.1) is not sufficiently small, the distance between two subsequent nodes MQ will not be small enough to take into account the rapid variations in the wavefields. Furthermore, whilst a particular value of *ELEM* may give satisfactory resolution, the corresponding value of *TRANSV* (Fig. 3.1) may be too large. For example, if the node next to the Borrmann fan edge (B in Fig. 3.4) is at the first zero of J_o (D in Fig. 3.4), then the simulation will fail to take into account the high intensity between B and D. Clearly, this is disastrous if the direct image is of interest. The only remedy is to decrease the integration steps near the Borrman fan edges.

When the incident wave is plane, it is important that the integration network reflect the variation in phase across the diffracted beam. The nodes must be spaced such that the variation in phase between two successive nodes MQ (Fig. 3.1) is small.

Whilst the integration step should be as small as possible for greater accuracy in the simulation, it should also be as large as possible in order to minimise the computational time taken to generate a simulation. In practice, the choice of step size represents a compromise between these two considerations.

Initially, simulation programs used *constant step algorithms* (C.S.A.'s), in which the integration steps, p and q, were constant. C.S.A.'s are satisfactory for simulation of section topographs where the direct image is not of concern. However, where the direct image is of interest, it is necessary to decrease the integration steps in those parts of the Borrmann fan which give rise to this image.

Petrashen [37] suggested that the values of p and q be allowed to decrease near the edges of the Borrmann fan, in order to reflect the greater local variation in wave amplitudes. Methods which allow p and q to vary, to suit the local variations in wave amplitudes, are called *varying step algorithms* (V.S.A.'s). V.S.A.'s allow very accurate simulation of direct images to be achieved.

Epelboin [38,39] has developed an algorithm in which the step size is automatically chosen, throughout the crystal, to reflect faithfully the variation in wave amplitudes. The setting up of the integration network for using this algorithm is based on three considerations:

1. the position of the extinction fringes in a perfect crystal is a good guide to local variation in wave amplitude,

2. the interaction of a defect with the wavefields is weaker near the diffracted edge of the Borrmann fan, and

3. the amplitude of wavefields increases greatly in the direction of a defect, whenever it exists.

In order to utilise point (1), the zeros of the Bessel function, J_o, are calculated, and a value of horizontal integration step is chosen so that there are at least five
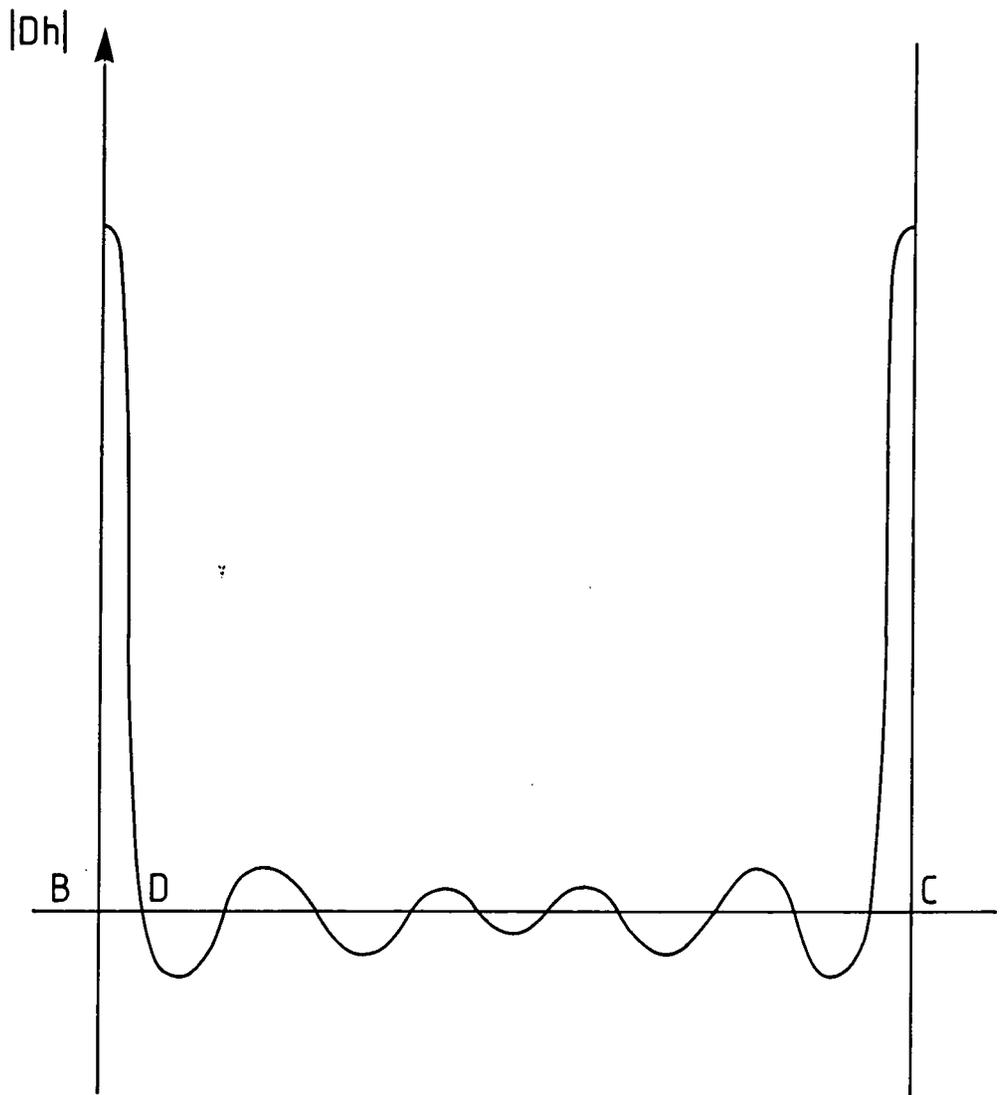
Fig. 3.4: Schematic variation of $|D_h|$ along the crystal exit surface.

steps between each two zeros. Hence, it is possible to calculate the amplitudes at the edges of the Borrmann fan without losing information on intensity or variation in wavefield. The integration step is automatically increased whenever the amplitudes of the wavefields vary more slowly. In fact, this can result in a network with fewer nodes than in the case of a C.S.A. Consequently, it is possible to achieve greater accuracy, with reduced computational time, by using a V.S.A.

Fig. 3.5 shows the position of extinction fringes in the Borrmann fan and Fig. 3.6 shows the corresponding integration network.

The algorithm (3.9) allows the intensity of the diffracted beam emerging from the exit surface to be calculated. However, a simulation program must also take into account the response of the recording medium to this beam, and subsequent developing procedures. The calculated intensities must be translated into various levels of grey in order to simulate what is actually seen on the experimental topograph.

In Fig. 3.3, a single incident ray was shown. The point A could be considered as a point source of waves, giving rise to the wavefields in the Borrmann fan. To simulate a real section topograph, we consider the incident beam as a series of *point sources* along the entrance surface. These points are used to construct the integration network, as in Fig. 3.7. The smaller the distance between point sources, the better the resolution of the final image. A traverse topograph is simulated by the addition of individual section topographs, corresponding to point sources arranged across the entrance surface, as in Fig. 3.8.

We will now return to the point made earlier that the simulation program must take into account the properties of the recording medium and subsequent processing of the photographic film.

There are numerous factors to take into account. For example, it is known that the smaller the grain size in the photographic emulsion, the better the resolution in the final topograph. Also, whilst it is desirable to have a thin emulsion for good resolution, it is also desirable to have a thick emulsion to compensate for relatively poor absorption of X-rays. Of course, the exposure time plays a crucial part in determining the contrast seen on the experimental topograph. Furthermore, the characteristics of the developing process can dramatically affect the quality of the final experimental image. Epelboin et al. [40] have investigated the effect upon image quality of the temperature at which the development is done. It was found that the lower the temperature of development, the better the resolution, but the longer the required exposure time. Increase in development temperature resulted in poorer quality images, but a welcome reduction in exposure time.

All of the above factors must be incorporated into the simulation program.

The earliest simulations were presented using line printers. Different levels of grey were obtained by overprinting. More recently, better quality images have been produced using raster systems. Epelboin [41] recommends the use of a storage display screen. This allows the simulation to be displayed on a screen. A spot of light is stored on the screen, and the distribution of light spots across the screen is translated, by the system, into different grey levels. This is done by splitting the
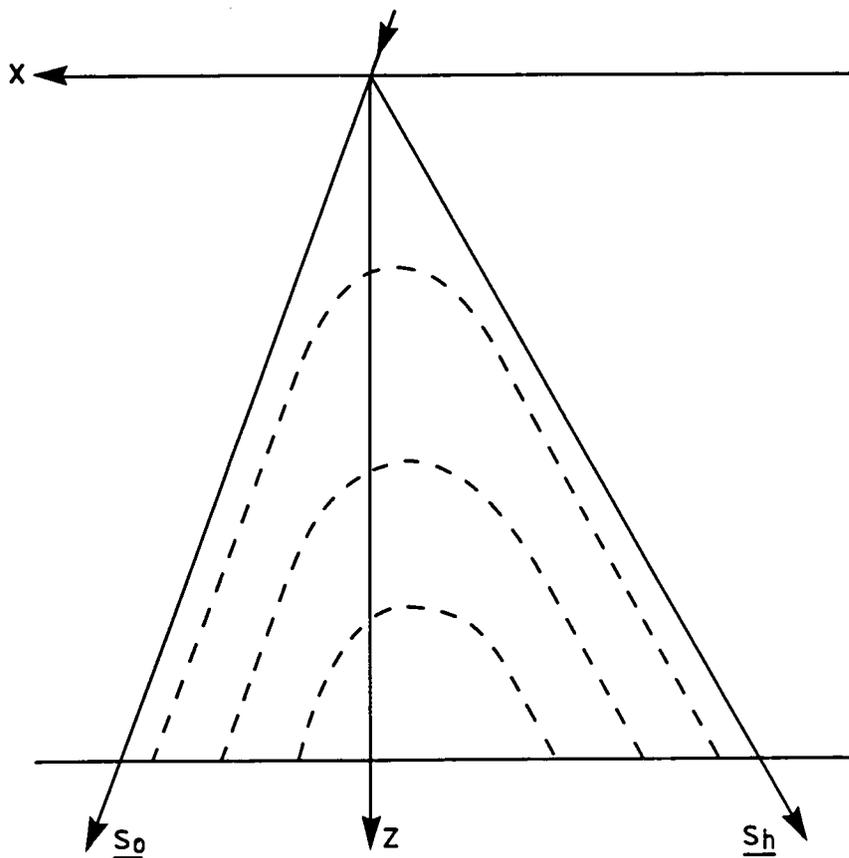
Fig. 3.5: Schematic representation of the positions of the minima of the extinction fringes, (after Epelboin).
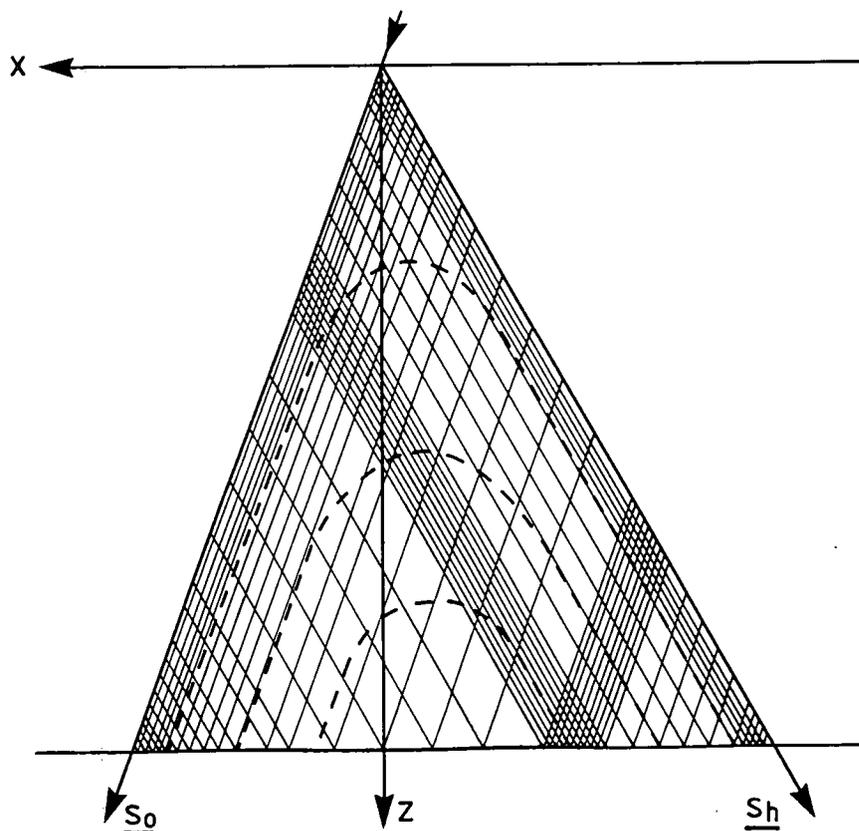
Fig. 3.6: The V.S.A. integration network, (after Epelboin).
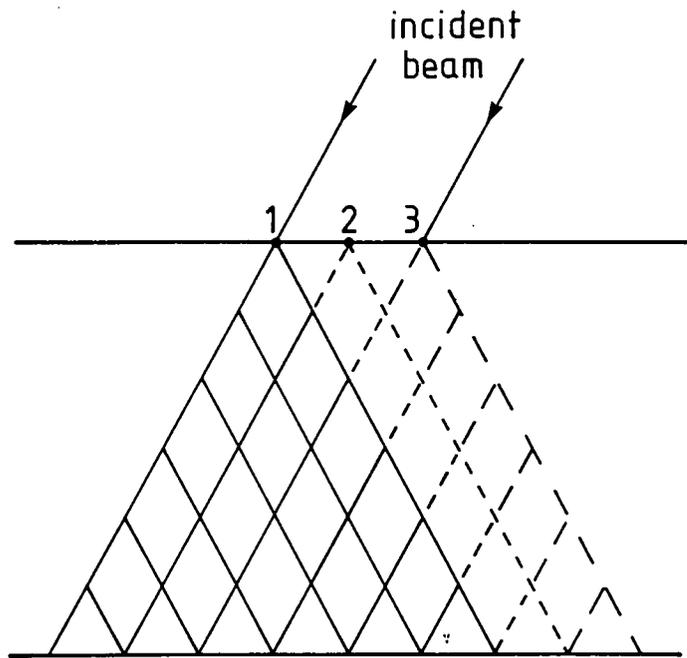
Fig. 3.7:   Simulation of a real section topograph, (after Epelboin).
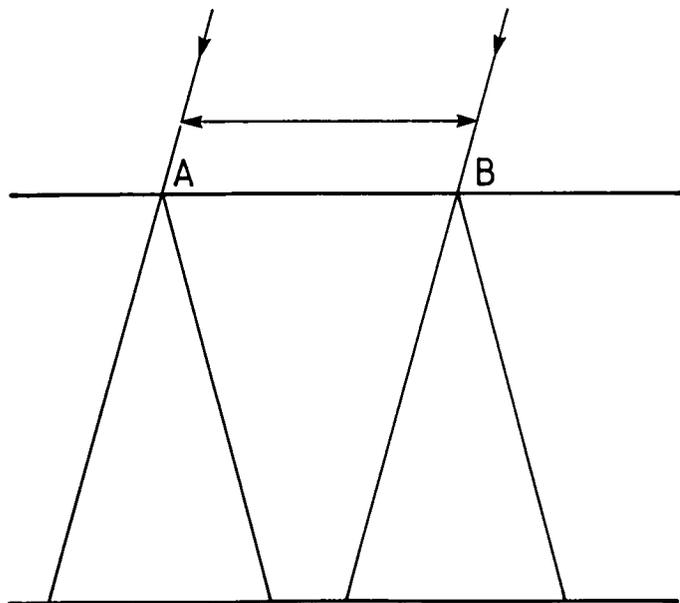
The contributions due to all point sources between A and B are added.

Fig. 3.8:   Simulation of a real traverse topograph, (after Epelboin).

screen into small areas, each of which contains a distribution of spots. The density of grey levels is then given either by the number of light spots in that area, or by the size of each spot in the area. The latter method is found to be preferable, enabling up to 56 different levels of grey to be displayed.

Chapter 4

Simulation of Topographs Due to Hydrogen Precipitates in Unbent Silicon Crystals

It was pointed out in Chapter 1 that precipitates can significantly affect the quality of a crystal for use in a device. Clearly, then, there is a need for some means of detecting the presence of precipitates in crystals. Section topography allows one to do this, and also to map the spatial distribution of precipitates within a crystal.

Cui et al. [42,43] have shown that hydrogen in the atmosphere around *float-zone* grown silicon enters the silicon crystal lattice during its growth. This results in the formation of silicon-hydrogen bonds, which are subsequently broken as the temperature increases. Hydrogen, dissociated by the breaking of bonds, then precipitates along the crystal lattice planes. Hydrogen atoms and molecules aggregate to form clusters. Each of these clusters grows by attracting surrounding atoms and molecules. Finally, a precipitate is formed which is spherical in shape, since in this case the required formation energy is least. With increasing temperature, dislocation glide occurs from cluster walls. This process is one means by which hydrogen causes mechanical damage in crystals, and illustrates why it is important to monitor precipitates in crystals.

Materials other than hydrogen give rise to precipitates, and techniques other than X-ray topography can be used to study such precipitates. It is interesting, for comparison, to look at such techniques. Bergholz et al. [44] have studied oxygen precipitation in silicon, using infra-red spectroscopy (IR), high-resolution transmission electron microscopy (HRTEM) and small-angle neutron scattering (SANS). Czochralski grown silicon contains about 10^{18} oxygen atoms per c.c. If such a sample is heated, then oxygen will diffuse throughout the crystal to agglomerate into silicon-oxide precipitates. IR was used to measure the loss of oxygen from solution, going to form precipitates, whilst HRTEM and SANS were used to investigate the number density and size of precipitates. It is very pleasing to see that the results obtained by HRTEM and SANS are in excellent agreement.

Mai et al. [45] have used X-ray topography to study silicon crystals containing hydrogen precipitates. They have shown that the crystal lattice surrounding a

precipitate is under compression. This illustrates the fact that there is a strain field associated with a precipitate inside a crystal.

Both Eshelby [46] and Teodosiu [47] have applied elasticity theory to the study of crystal defects. We will turn our attention to point defects in particular.

Suppose the displacement at some point, due to the presence of the defect, is $\underline{u}$. Now, the model we will use for a point defect is that of a spherical rigid or elastic inclusion in an infinite, isotropic medium. In each case, the strain field due to the defect is spherically symmetric. Hence, a precipitate can be modelled by a spherically symmetric point defect. If we use spherical coordinates (r, θ, ϕ), we have:

$$\underline{u} = u_r(r)\underline{e_r}; \qquad u_\theta = u_\phi = 0,$$

where u_r, u_θ, u_ϕ are the $r-, \theta-$ and $\phi-$components, respectively, of $\underline{u}$ and $\underline{e_r}$ is a unit vector in the r–direction.

Teodosiu shows that u_r must satisfy the equation:

$$r^2\frac{d^2 u_r}{dr^2} + 2r\frac{du_r}{dr} - 2u_r = 0, \tag{4.1}$$

which has the general solution:

$$u_r = \frac{C}{r^2} + C_1 r, \tag{4.2}$$

where C and C_1 are constants.

From physical considerations, u_r must vanish at infinity, so that $C_1 = 0$ and solution (4.2) reduces to:

$$u_r(r) = \frac{C}{r^2}. \tag{4.3}$$

(4.3) represents the spherically symmetric strain field due to a point defect. In order to simulate the topograph due to a precipitate, it is necessary to take into account the strain associated with that precipitate. Consequently, equation (4.3) is crucial.

Although the first simulations of dislocation images in X-ray topographs were made in 1967 by Balibar and Authier [48], it was not until recently that simulations of spherical strain centres were performed [35,49].

The images due to precipitates have structure which can be broken down into parts which correspond to the direct, intermediary and dynamical images described in Chapter 1. Green et al. [35] have simulated images of spherical strain centres in X-ray topographs. The strain field used was that given by equation (4.3) and several useful results were obtained.

First of all, it was found that the height of the defect image is determined solely by the magnitude of the strain field. The image height increases with increasing strain. The quantity C in equation (4.3), called the *deformation parameter*, is a measure of the strength of the strain field associated with the defect. It was found that the image height, h, was given by:

$$h = A \ln C,$$

where A is a constant.

Furthermore, the image length in the incidence plane is determined solely by the depth of the precipitate in the crystal. This is illustrated in Fig. 4.1.

If p = depth of defect in crystal,

b = thickness of crystal,

q = width of defect image, and

a = width of topograph,

then by simple geometrical considerations:

$$\frac{b-p}{b} = \frac{q}{a},$$

so that $p = b\left(1 - \frac{q}{a}\right).$

Hence, it is a simple matter to determine the depth of the precipitate, since all other quantities can be measured.

It was also found that as the precipitate position moves away from the direct beam, towards the diffracted beam edge, the dynamical and intermediary images reverse their relative positions, and the visibility of the dark head of the defect image reduces. Hence, by looking for these effects on topographs, it is possible to find the distance of the defect from the direct beam. Lefeld-Sosnowska et al. [50] have studied the effects of moving a defect at the exit surface of a crystal, from the direct beam position to the diffracted beam edge, Fig. 4.2. Since the defect is at the exit surface, the extent of the image is limited to a spot. For a defect at A, in the direct beam, the image is a black spot. The darkness of the spot reduces through positions B and C, until at position H, at the diffracted beam edge, the spot is white.

The purpose of the present work is to use a simulation technique, based on the strain field given by equation (4.3), to simulate section topographs due to hydrogen precipitates in silicon. The simulation program called 'SECTION', in Appendix A1, was used.

The first task was to simulate an experimental topograph, taken using the $3\bar{3}\bar{3}$ reflection, for a crystal whose thickness was known to be approximately 800 microns. First of all, a diagram of the reflection geometry was drawn. In order to draw such a diagram, it is necessary to know the Bragg angle, θ_B, and the orientation of the Bragg planes relative to the crystal surfaces.

Consider Fig.4.3.

(a) To Find the Orientation of the Bragg Planes

Suppose the normal to the entrance surface is $\underline{n}$ and the normal to the Bragg planes is $\underline{g}$. Then the angle, θ, between these two vectors is given by:

$$\theta = \arccos\left|\frac{\underline{n}.\underline{g}}{|\underline{n}||\underline{g}|}\right|. \tag{4.4}$$
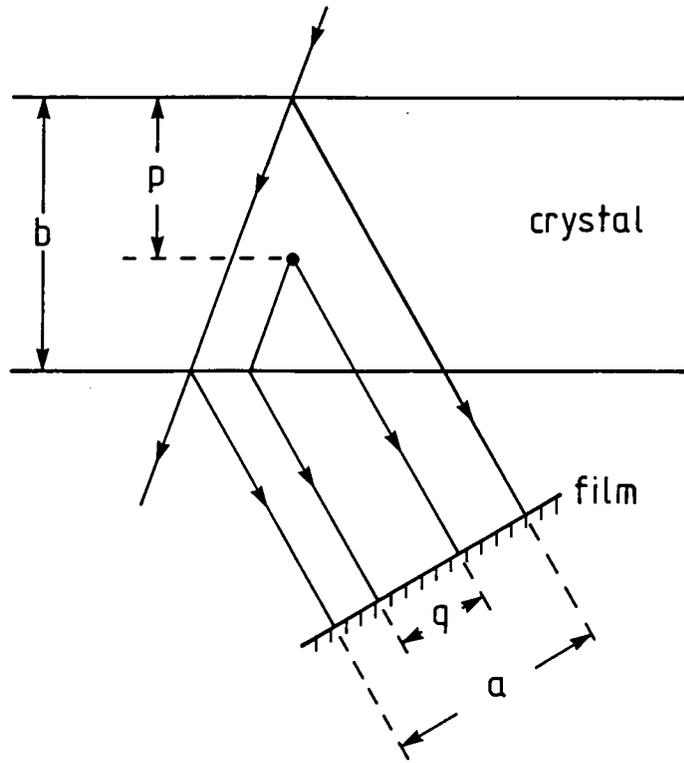
Fig. 4.1: Determination of defect depth.
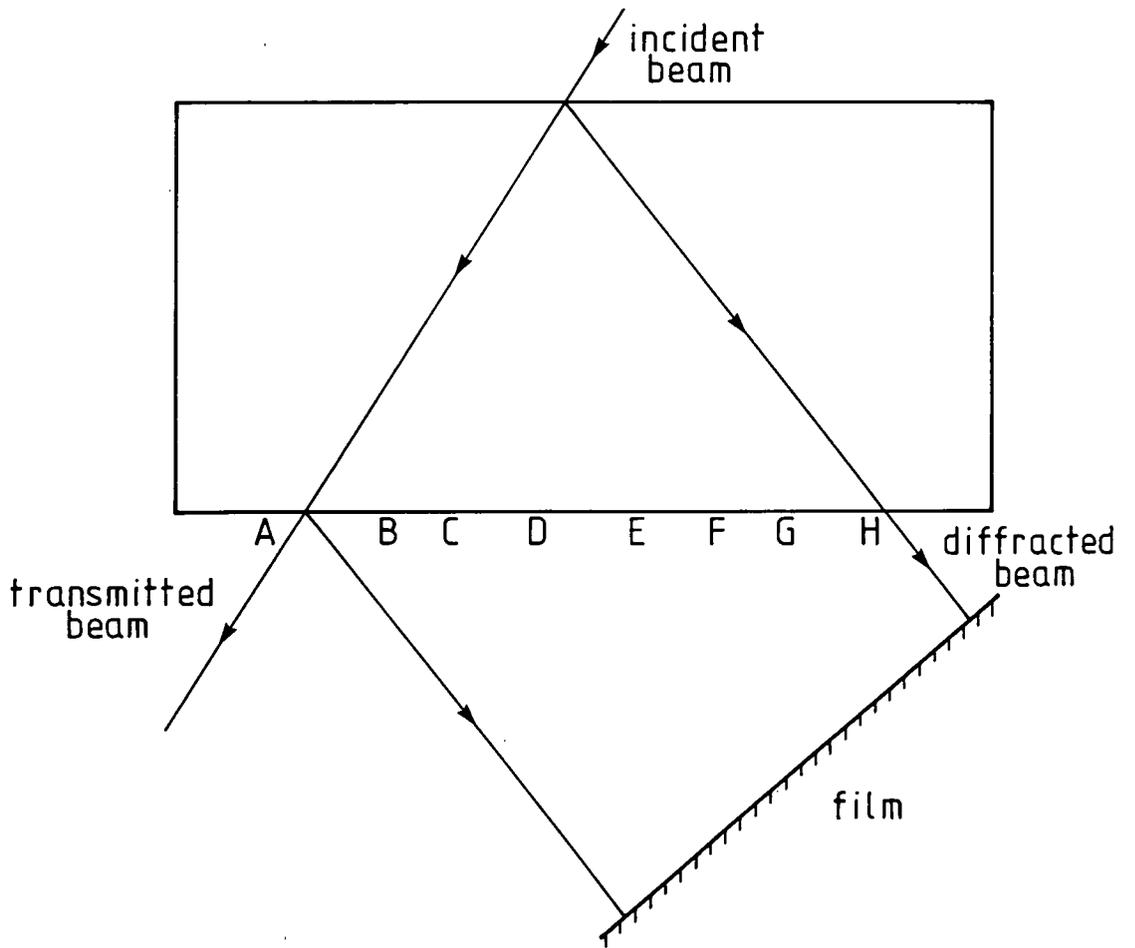
Fig. 4.2: Moving a defect across the base of the Borrmann fan.
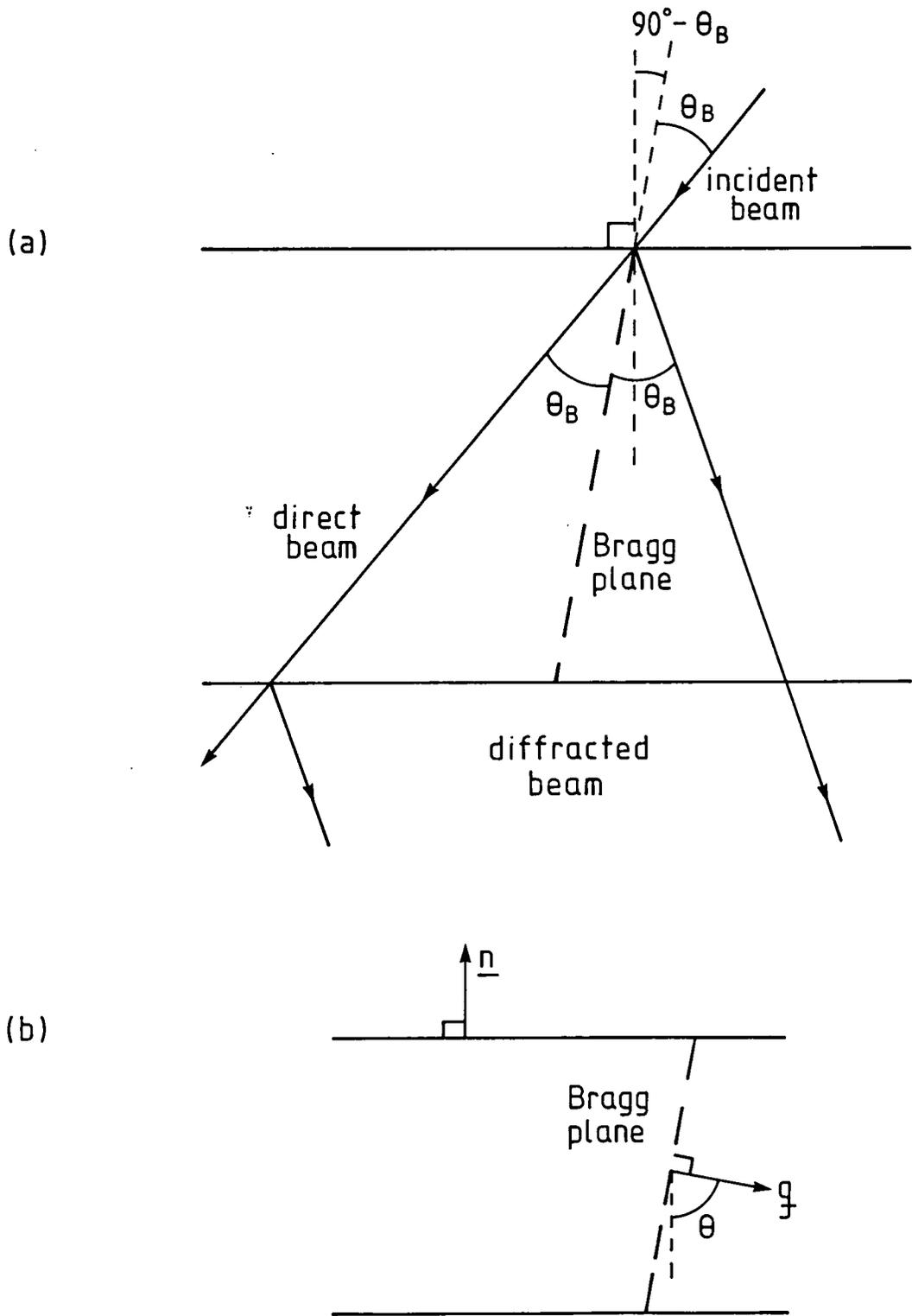
Fig. 4.3: Finding the geometry of a reflection.

This defines the orientation of the Bragg planes.

(b) To find the Bragg Angle

The Bragg condition is:

$$2d(hkl)\sin\theta_B = \lambda,$$

where $d(hkl)$ = spacing of planes with indices $\{hkl\}$,

θ_B = Bragg angle, and

λ = wavelength of radiation.

$d(hkl)$ can be obtained from the relation:

$$d(hkl) = \frac{a}{\sqrt{(h^2 + k^2 + l^2)}}, \qquad (4.5)$$

where a = lattice parameter of silicon

= 5.43 Å.

So, if λ is known, in the same units as d, then θ_B can be found from:

$$\theta_B = \arcsin\left[\frac{\lambda}{2d(hkl)}\right]. \qquad (4.6)$$

All of the simulations in this piece of work are for crystals with surface normal $\underline{n} = (1,1,1)$.

Now, for the $3\overline{3}\overline{3}$ reflection, $\underline{g} = (3,-3,-3)$. Hence, using relation (4.4):

$$\theta = \arccos\left|\frac{-1}{3}\right|,$$

so that $\underline{\theta = 70.5^\circ}.$ $70^\circ 3\overline{z}'$

Also, from (4.5):

$$d(3\overline{3}\overline{3}) = \frac{5.43}{\sqrt{27}} \text{ Å},$$

so that d = 1.05 Å.

For the radiation used in the experiments, $\lambda = 0.7093$ Å. Hence, from (4.6):

$$\theta_B = \arcsin\left[\frac{0.7093}{2 \times 1.05}\right],$$

so that $\underline{\theta_B = 19.7^\circ}.$

Using these values of θ and θ_B, a diagram of the reflection geometry was drawn, Fig. 4.4.

By inspection of the experimental topograph, Fig. 4.5(a), it is clear that the precipitate is near the entrance surface, since the image occupies the full width of the topograph. Furthermore, there is a strong, dark head, implying that the defect is close to the direct beam. Simulations were made for test points at the entrance surface, close to the direct beam. Initially, a value of crystal thickness of 800 microns was used in the simulations. This value was obtained by a geometrical consideration of the width of the experimental topograph and the width of the incident beam, and is accurate in this case to within an extinction distance. The simulation due to a precipitate at point P, with $x - z$ coordinates (10,0), in microns, was found to correspond most closely to the experimental image; see Fig. 4.5(b). However, in order to get a match between the Pendellösung fringes, a more accurate value of crystal thickness was required. It was necessary to adjust slightly the crystal thickness in successive simulations, Fig. 4.6. This neatly illustrates the fact that Pendellösung fringe structure depends on crystal thickness. The closest fit to experiment is simulation (b) in Fig. 4.6, corresponding to a crystal thickness of 792 microns. Hence, we can assign a value of thickness to the crystal of 792 microns, to within about one tenth of an extinction distance, in this case. Simulation 4.6(b) is compared with the experimental topograph in Fig. 4.7. The match between Pendellösung fringes in the experimental and simulated topographs is very good, as is the agreement between the direct and intermediary images.

This illustrates the power of the simulation technique. The position of the defect has been determined, with coordinates (10,0), in microns, relative to the origin where the incident beam strikes the crystal.

It is interesting to compare the Pendellösung fringes in simulations (f) and (g), in Fig. 4.6, with those of simulation (b). Simulations (b) and (f) show that increasing the crystal thickness by half an extinction distance, in this case 32 microns, results in a complete reversal of fringe contrast. Simulations (b) and (g) show that increasing the crystal thickness by a further half of an extinction distance returns the fringe contrast to its original state. This is in accord with the *spherical-wave theory* of Kato[51].

The next task was to simulate images in the topographs, taken using the $1\bar{1}\bar{1}$ reflection, for a different crystal whose thickness was again known to be approximately 800 microns.

Using relations (4.4), (4.5) and (4.6) again, this time with $\underline{g} = (1, -1, -1)$, gives:

$$\theta = 70.5°, \text{ and}$$
$$\theta_B = 6.5°.$$

The corresponding reflection geometry is shown in Fig. 4.8.

Visible in the experimental topograph, Fig. 4.9(a), are two very distinctive types of image. These will be referred to as Class I and Class II. The Class I image is narrow, and stretches the full width of the topograph. It has a 'peardrop' dark head and a light tail with some internal bright and dark structure.
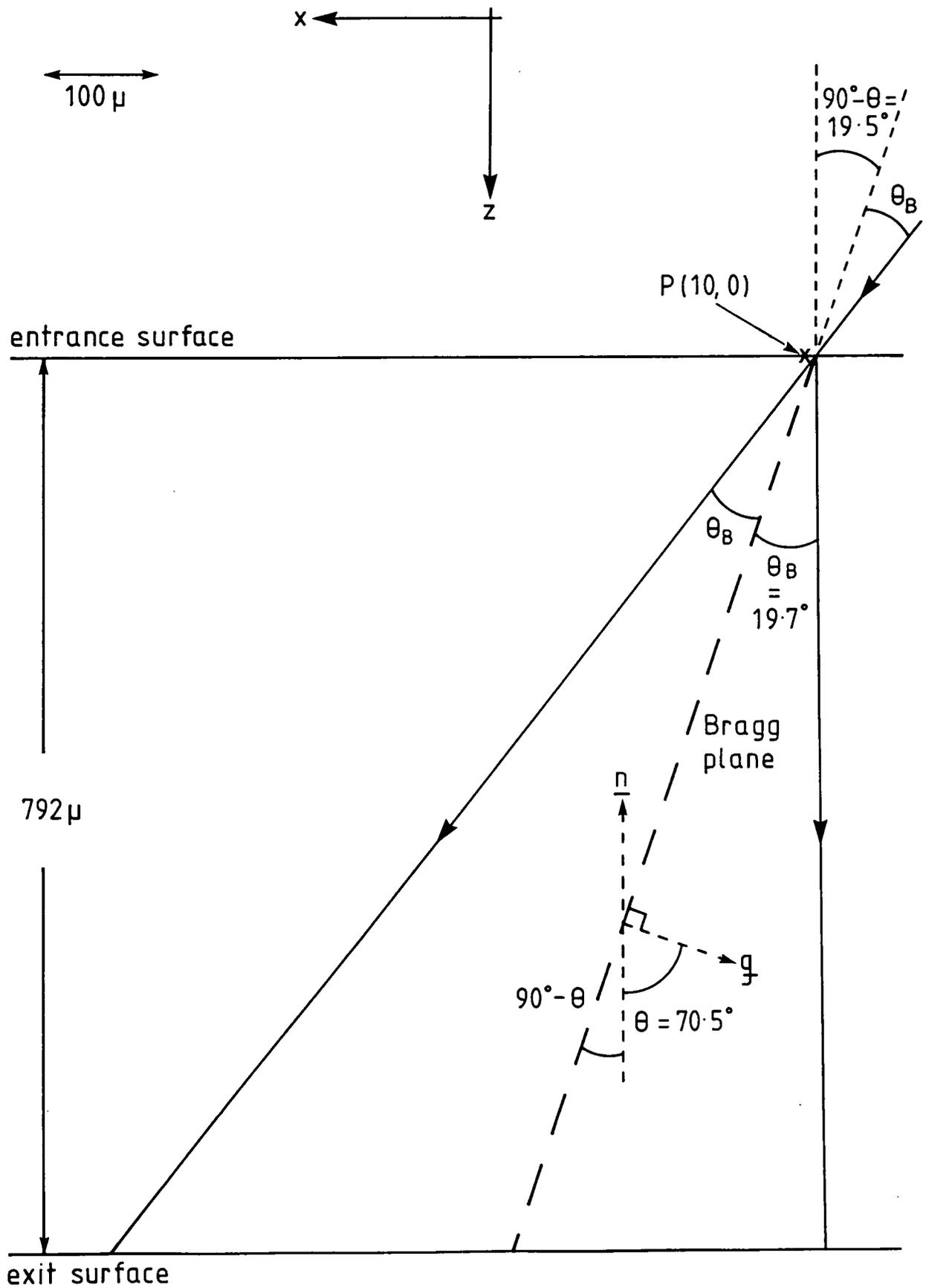
Fig. 4.4: $3\bar{3}\bar{3}$ reflection, (792 micron crystal).

(a)

$\overrightarrow{g}$
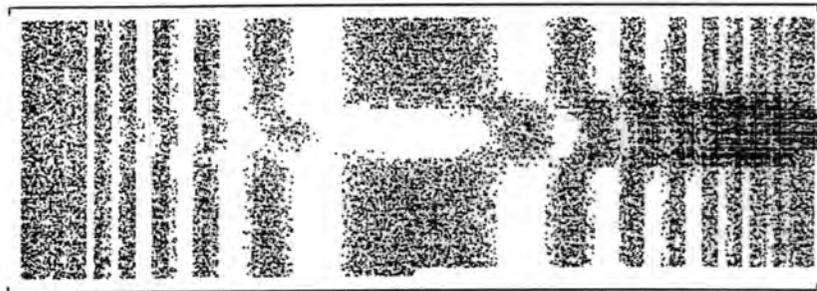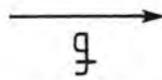
(b)

Fig. 4.5: 3$\bar{3}\bar{3}$ reflection.

(a) Experimental topograph.
(b) Initial attempt at simulation.

Field width = 670μ.
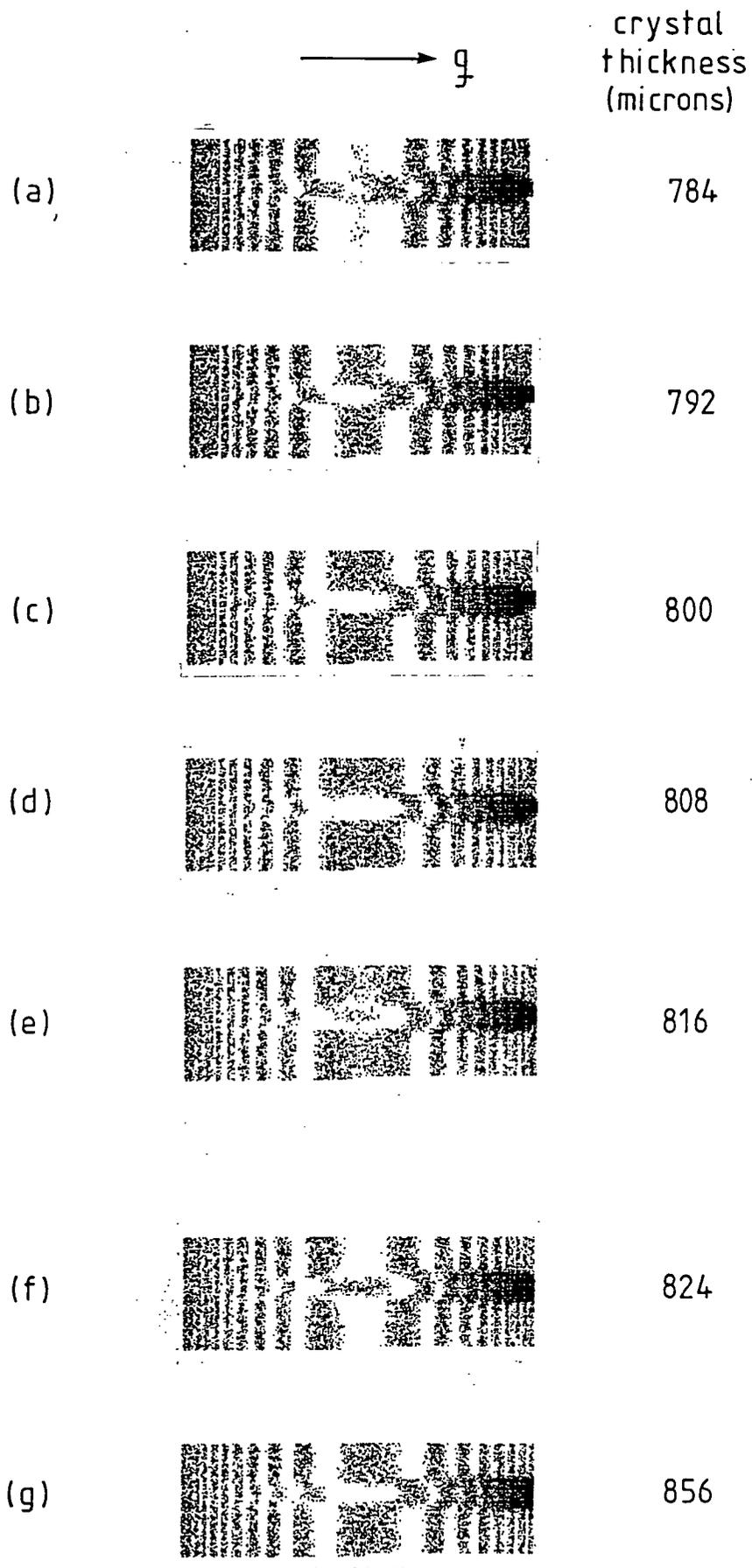
Fig. 4.6: Simulations for the 3$\bar{3}\bar{3}$ reflection, showing the variation in Pendellösung fringe structure with increasing crystal thickness.

(a)

$\xrightarrow{}$
$\underset{}{g}$
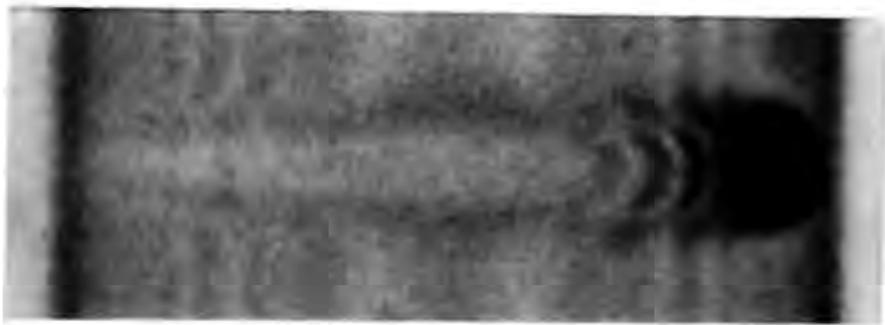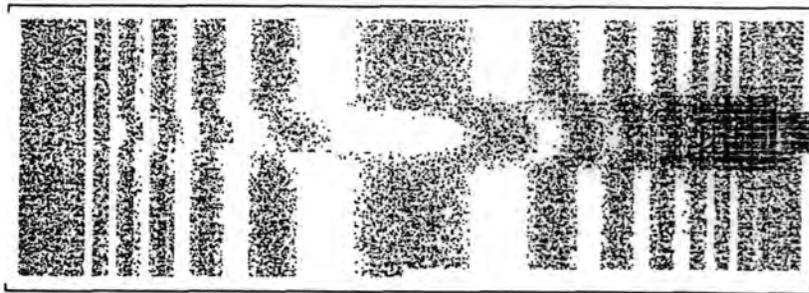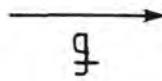
(b)

Fig. 4.7:   3$\bar{3}\bar{3}$ reflection.

(a)   Experimental topograph.
(b)   Accurate simulation.

Field width = 670μ.
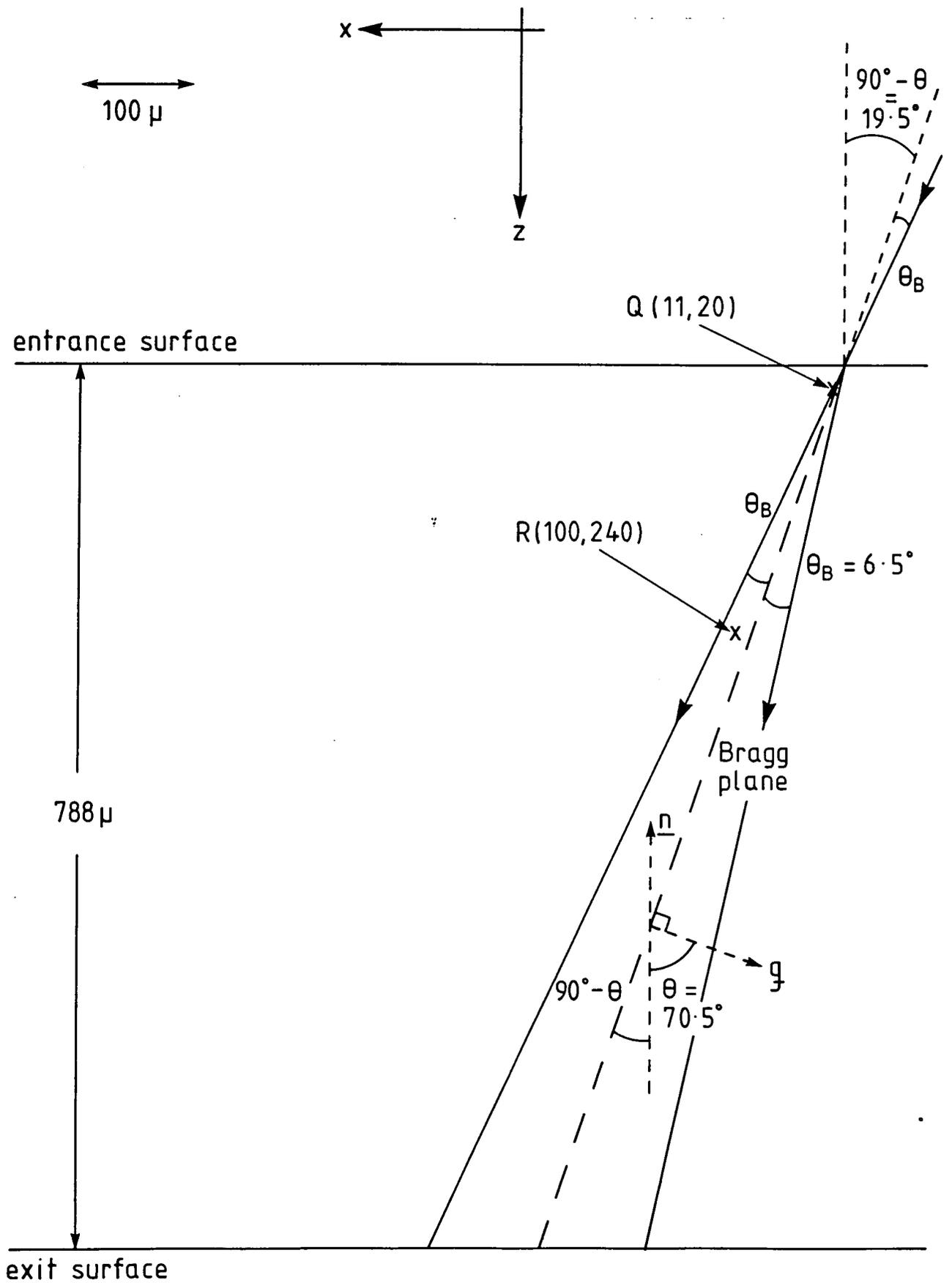
Fig. 4.8: 1Ī̄Ī reflection, (788 micron crystal).
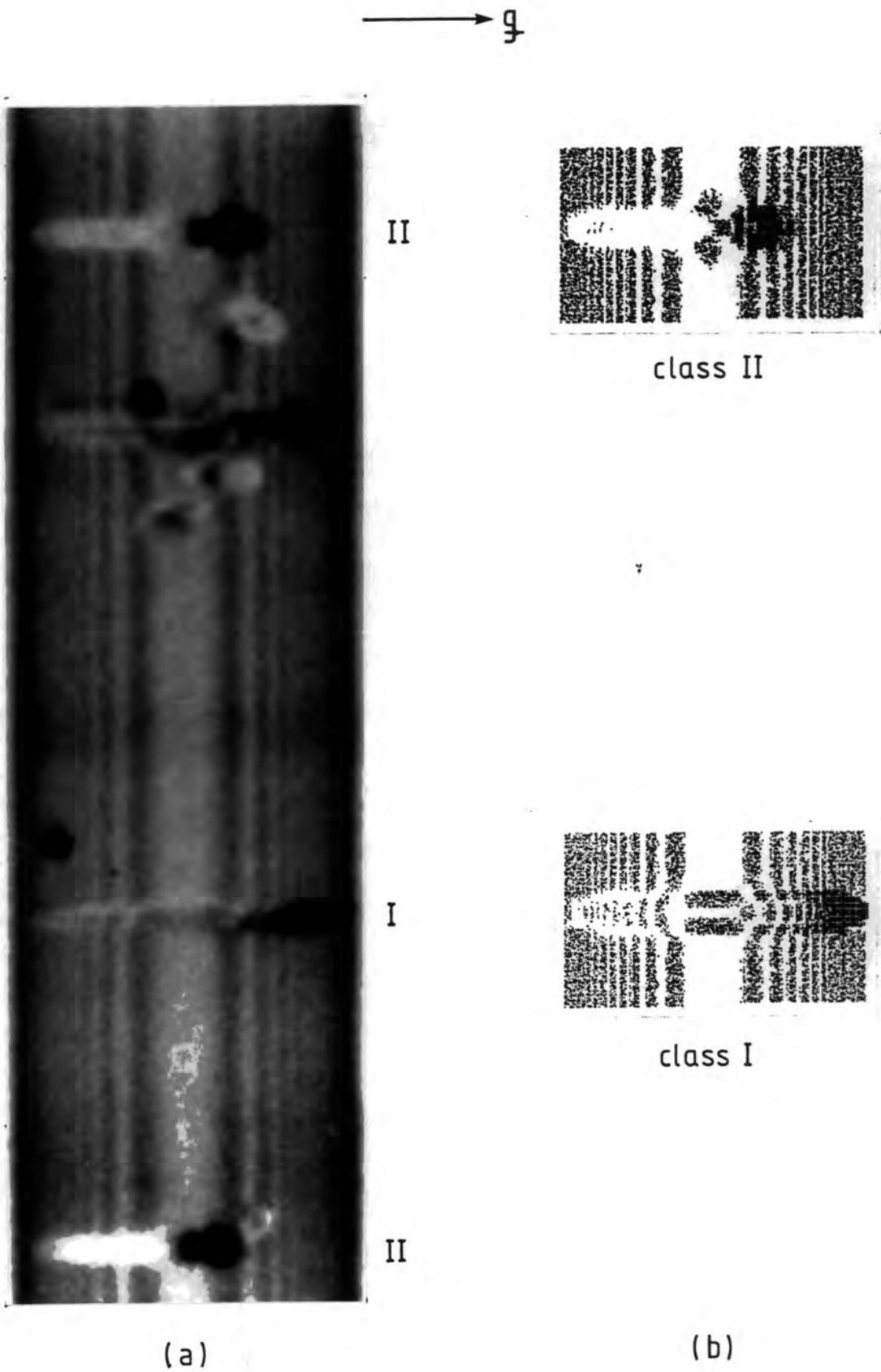
Fig. 4.9: 1$\bar{1}\bar{1}$ reflection.

(a) Experimental topograph.
(b) Simulations.

Field width = 195μ.

There is only one Class I image in the topograph, and it is labelled I. Class II images occupy about two-thirds of the width of the topograph and show very clear contrast. They have very dark 'mushroom' heads and very bright 'comet' tails, with no intermediary image. There are two Class II images in the topograph, and these are labelled II.

By taking simulations of different crystal thicknesses, for the same precipitate test point, and comparing the Pendellösung fringes with those on the experimental topograph, the sample crystal thickness at this point was found to be 788 microns.

The large width of the Class I image indicates that the corresponding defect is close to the entrance surface. The dark head implies that the defect is close to the direct beam. The closest simulation is shown in Fig. 4.9(b), corresponding to a precipitate at point Q (11,20).

The width of Class II images indicates that the corresponding defects are located at about one third of the crystal depth. The dark head again implies that the defects are close to the direct beam. The closest simulation to Class II is shown in Fig. 4.9(b), corresponding to a precipitate at point R (100, 240).

Again, simulation is in good agreement with experiment and enables the defect position to be determined accurately.

It is helpful, when trying to locate a precipitate by this method, to make a set of simulations, corresponding to an array of test points for the precipitate. Such an array of points is illustrated in Fig. 4.10 for the $3\bar{3}\bar{3}$ reflection and in Fig. 4.11 for the $1\bar{1}\bar{1}$ reflection. The corresponding simulations are displayed in Figs. 4.12 and 4.13, respectively.

It is seen that for the $3\bar{3}\bar{3}$ reflection, Fig. 4.12 , the only defect images obtained are for defect positions close to the Borrmann fan edges. In both cases, Fig. 4.12 and Fig. 4.13, the effects described earlier, of varying the defect depth and varying the position across the Borrmann triangle at constant depth, are clearly seen.

Attempts were then made to incorporate surface relaxation into the simulation program, and to determine its effect on the simulations. In order to do this, the *method of images* was used, illustrated in Fig. 4.14.

Fig. 4.14(a) shows a defect, D, at depth z below the crystal surface. Consider now an 'image precipitate', D', to be placed at a distance z above the surface, Fig.4.14(b). Then, the vertical component of strain at all points along the surface is zero. This, then, is a model of surface relaxation.

Fig. 4.15 shows that if the coordinates of some point $P(x,y,z)$, relative to $D(x_{ppt}, y_{ppt}, z_{ppt})$, are $(x - x_{ppt}, y - y_{ppt}, z - z_{ppt})$, then the coordinates of P relative to D' are $(x - x_{ppt}, y - y_{ppt}, z + z_{ppt})$. Consequently, in order to incorporate surface relaxation into the simulation program SECTION, Appendix A1, it is simply necessary to add another line like (b) in SECTION, to take into account the effect of the image precipitate. The alterations are shown in Appendix A2. Apart from these changes, the new simulation program, 'IMAGE', is the same as SECTION. The variable 'dsh' in (b')1, Appendix A2, stores the data calculated by the procedure DIFFPOINT for precipitate D, and the new variable 'dshnew' in (b')2 stores the data calculated for the image precipitate D'. These lines are followed by (b')3,

28
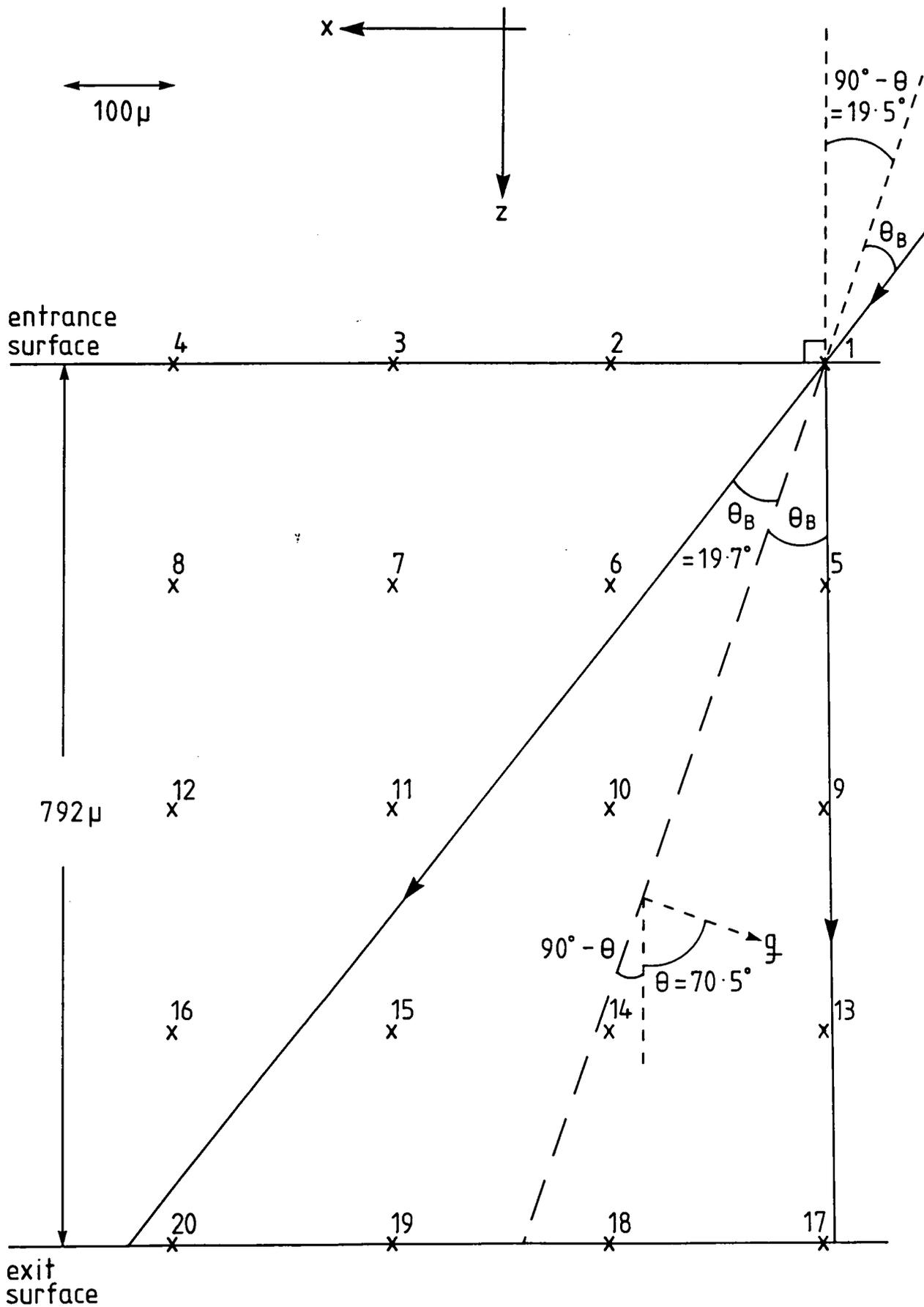
Fig. 4.10: Array of precipitate test points for the $3\bar{3}\bar{3}$ reflection.
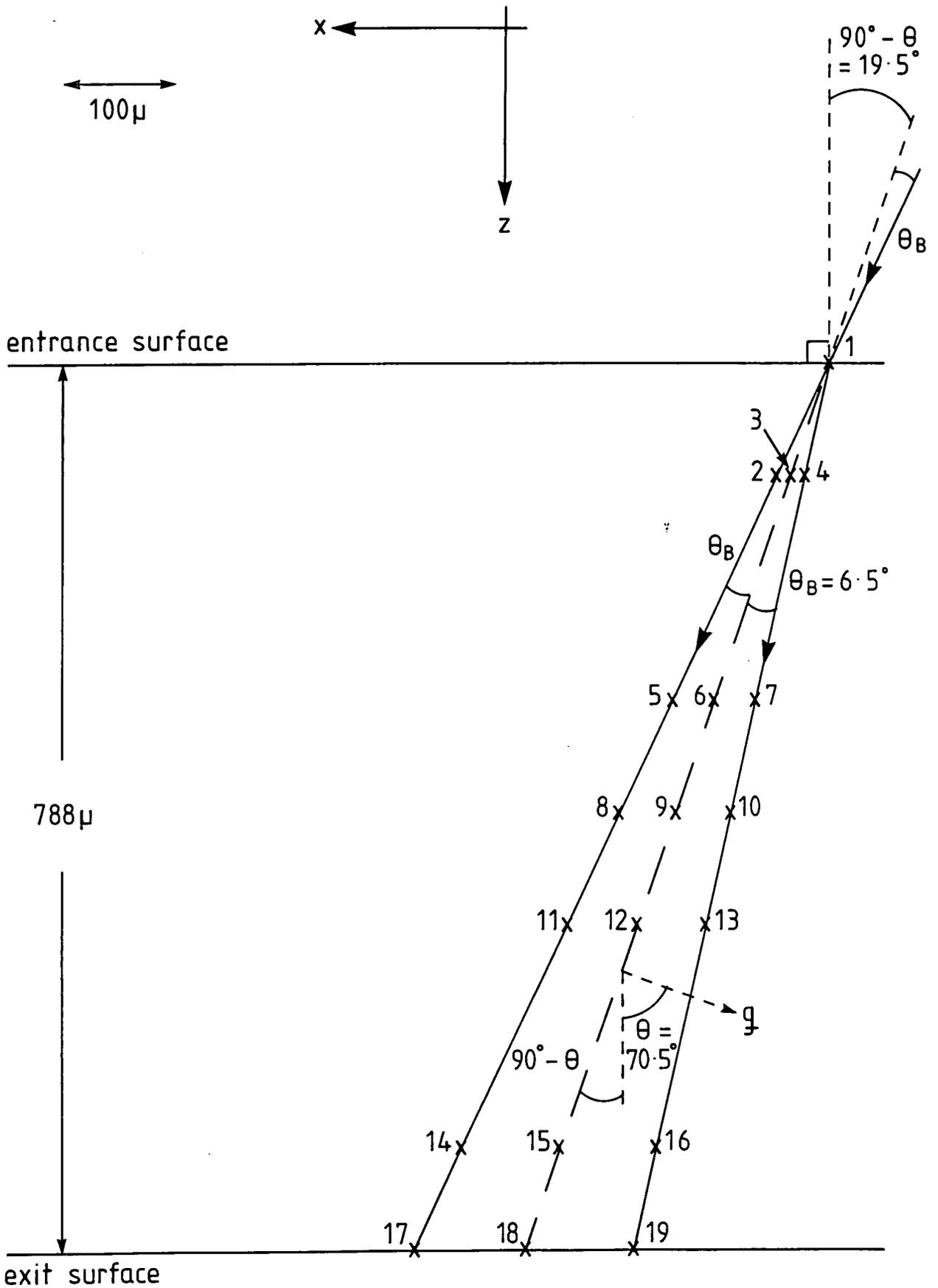
Fig. 4.11: Array of precipitate test points for the 1$\bar{1}\bar{1}$ reflection.

1　5　9　13　17

g →

2　6　10　14　18

3　7　11　15　19

4　8　12　16　20
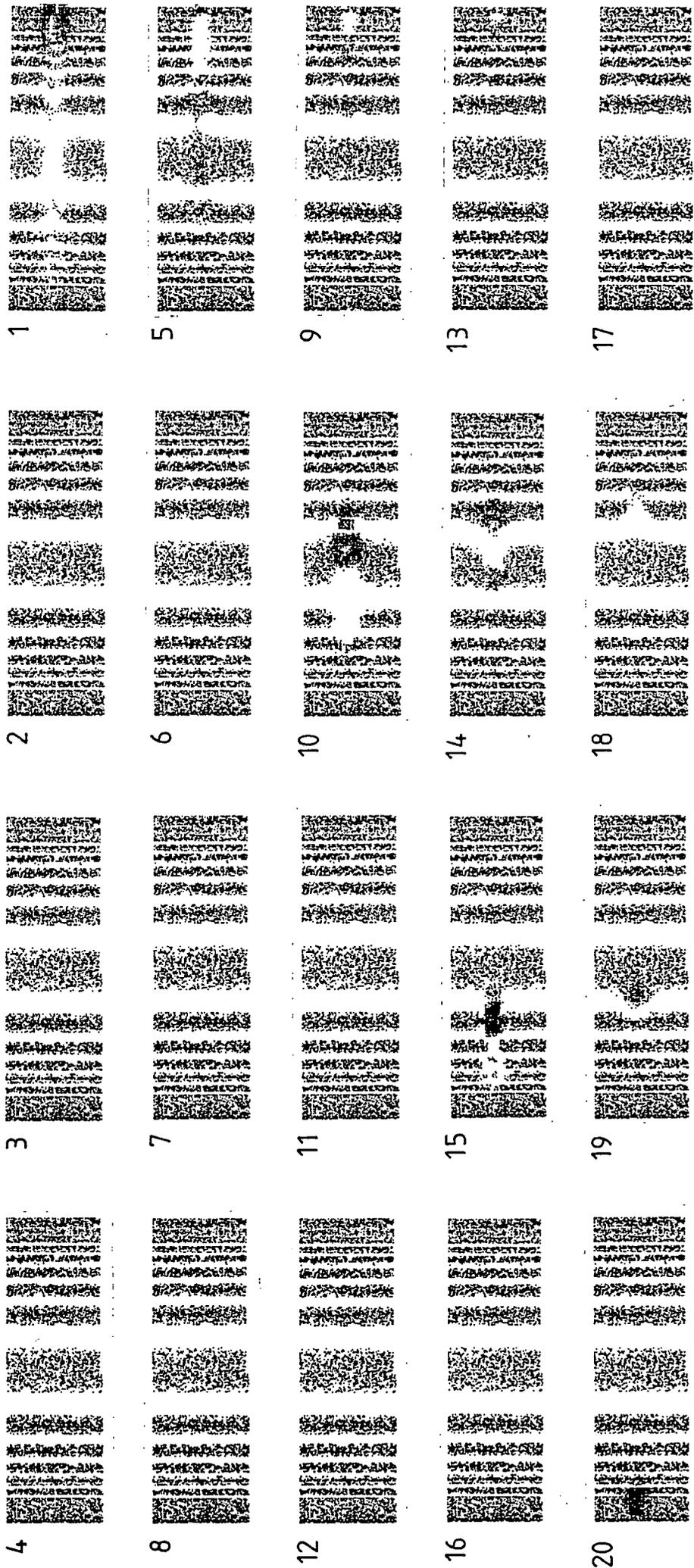
Fig. 4.12:　Array of simulations for the 3̄3̄3̄ reflection.
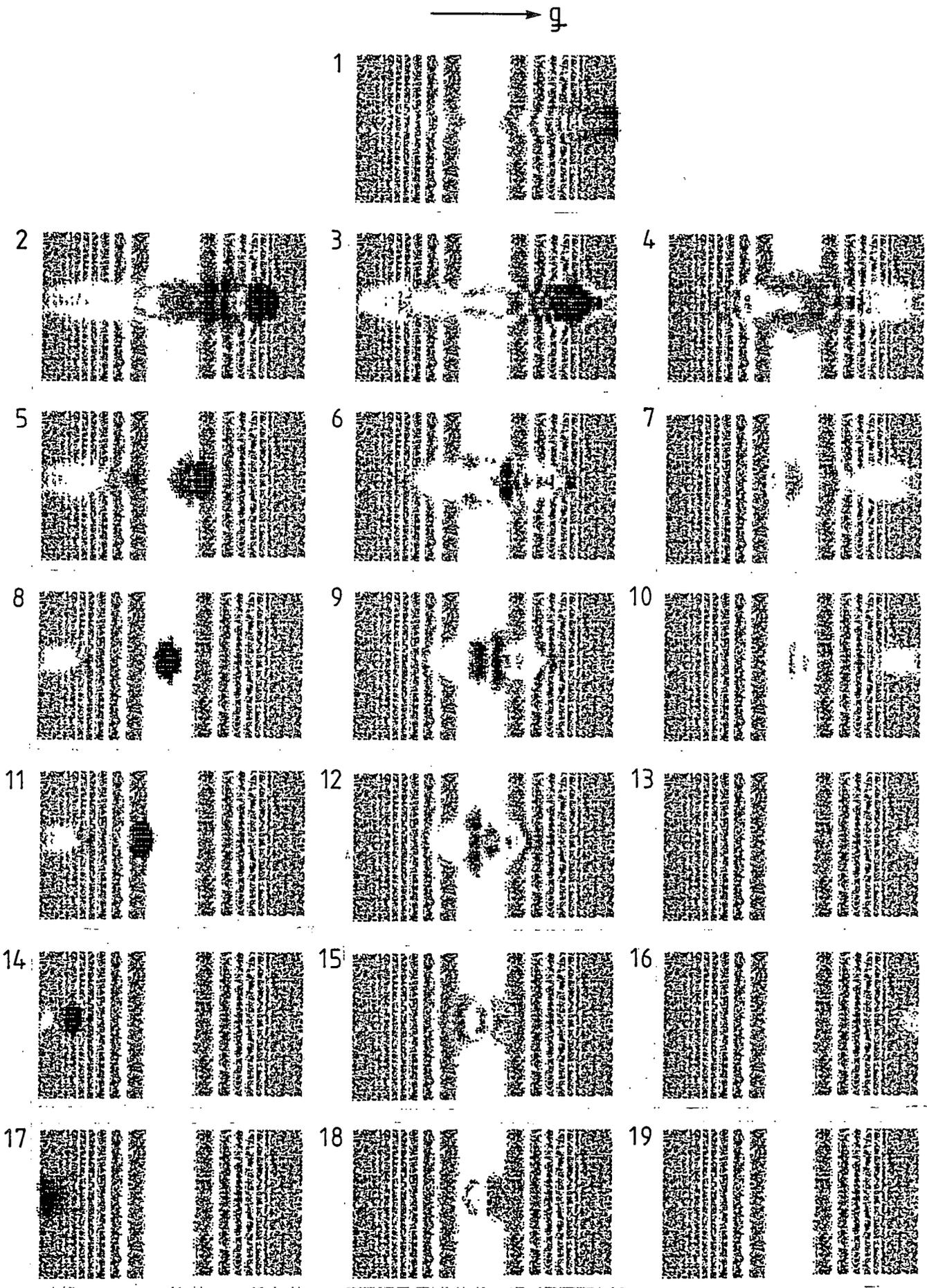
Fig. 4.13: Array of simulations for the 1Ī̄1 reflection.

(a)   (b)
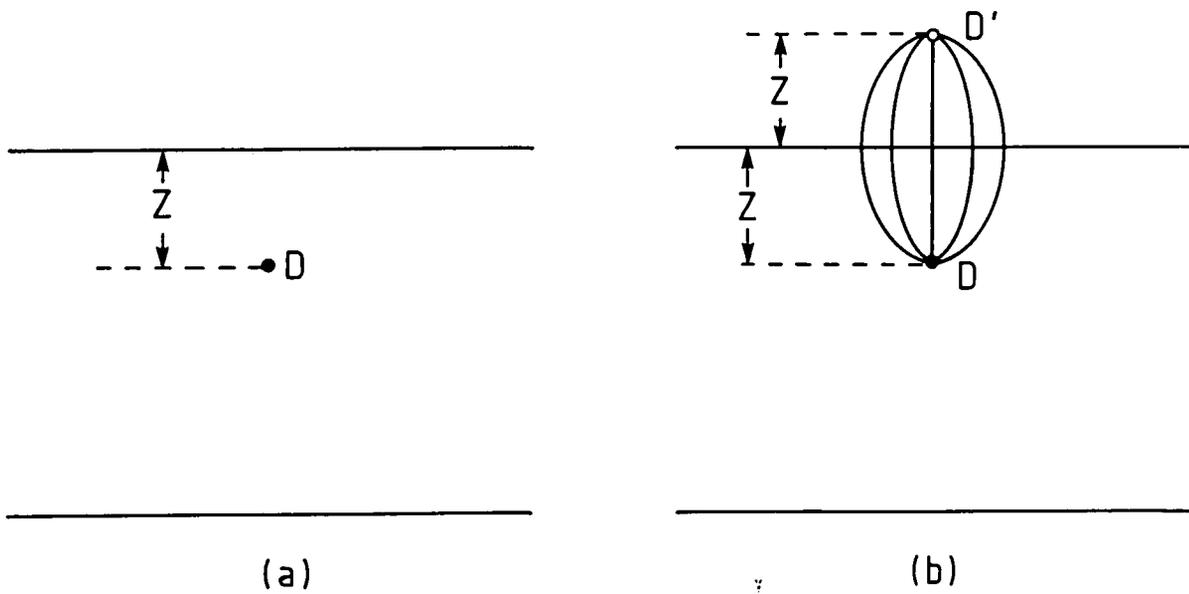
Fig. 4.14: The method of images.

$D'(x_{ppt}, y_{ppt}, -z_{ppt})$

x

y

z

$D(x_{ppt}, y_{ppt}, z_{ppt})$

$P(x, y, z)$
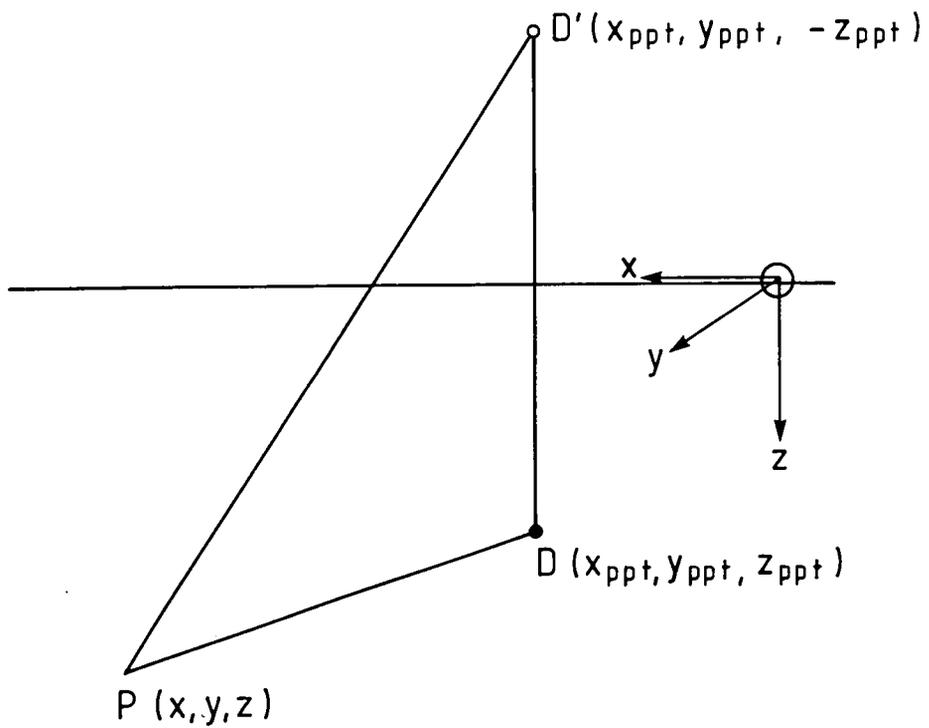
Fig. 4.15: Positions of precipitate and image
            precipitate.

which has the effect of re-defining 'dsh' to represent the strain field due to both D and D'. Of course, it is necessary to include 'dshnew' in the declaration of variables in line (a') of IMAGE.

The new simulation program was used specifically to find the depth at which the effect of surface relaxation became negligible. This was done by taking simulations, for the $3\overline{33}$ reflection, for precipitates along the direct beam at different depths, using both the original and the altered program. This was done for five different values of deformation parameter, i.e. five different strain fields. The results are shown in Appendix B1-5, for deformation parameters of $5 \times 10^{-21}, 1.7 \times 10^{-20}, 5 \times 10^{-20}, 1.5 \times 10^{-19}$ and 5×10^{-19}. In order to check the results, the same process was repeated for points, at different depths, along a Bragg plane. The results are shown in Appendix C1-5.

Clearly, as the deformation parameter increases, the deeper the defect must be before the effect of surface relaxation can be neglected.

Plots of depth at which the effect of surface relaxation becomes negligible vs. deformation parameter are given for the direct beam case, Fig. 4.16(a), and for the Bragg plane case, Fig. 4.16(b). The forms of the curves are almost the same, indicating that the effect of surface relaxation varies with depth, rather than with lateral displacement of the defect across the Borrmann triangle.
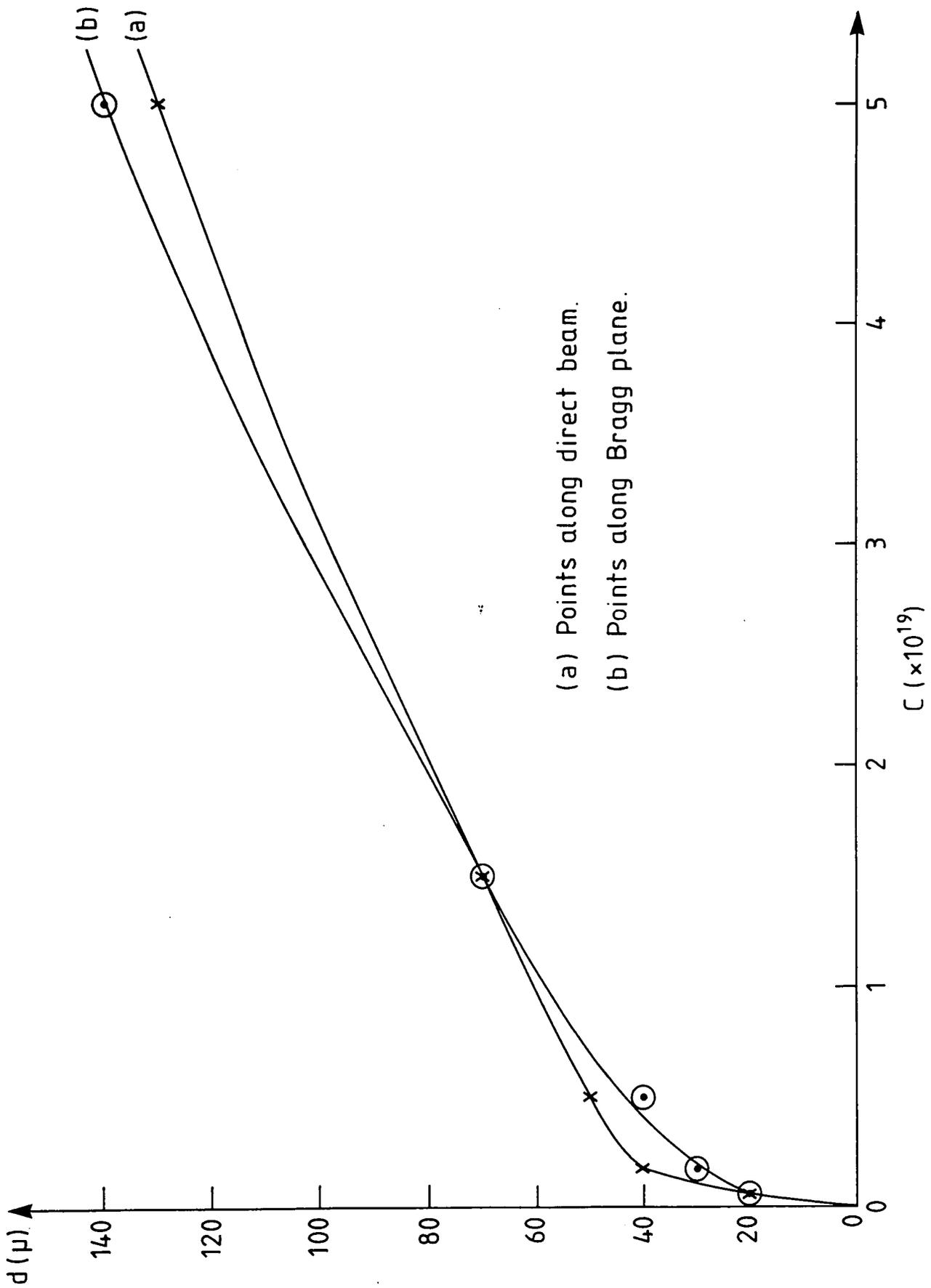
Fig. 4.16: Depth at which difference between simulations with and without surface relaxation becomes negligible, d, vs. deformation parameter, C.

Chapter 5

Simulation of Topographs Due to Hydrogen Precipitates in Curved Silicon Crystals

Growth of an oxide layer, on one surface, forms an integral part of silicon device production technology. The thermal expansion coefficients of the silicon and the oxide are different. In fact, when the oxidised wafer is cooled to room temperature from the oxidation temperature (approx. 1200°C) the oxide film contracts less than the silicon wafer. Consequently, the wafer becomes dish-shaped, as in Fig. 5.1.

Meieran and Blech [52] found that for an asymmetric reflection, the intensity diffracted from a bent crystal was appreciably greater than that diffracted from an unbent crystal. However, the intensity diffracted in a symmetric reflection was the same for both bent and unbent crystals. The enhanced diffracted intensity in the asymmetric case is explained by Kato's spherical-wave dynamical theory of X-ray diffraction for lightly strained, nonabsorbing crystals [53,54]. According to this theory, the intensity diffracted by a set of Bragg planes increases rapidly with Bragg plane curvature. Now, the Bragg planes involved in an asymmetric reflection bend as a result of wafer curvature, giving rise to increased diffracted intensity. The Bragg planes involved in a symmetric reflection remain flat, although no longer parallel, as a result of wafer curvature. These planes fan out so that the effective misorientation is zero. Consequently, a change in intensity from the unbent crystal case is not expected.

Meieran and Blech [52] put to good use the increased intensity diffracted from asymmetric reflections. They showed that by deliberately bending a crystal during the taking of a topograph, the increased intensity would allow a welcome reduction in exposure time.

Hart [55] has investigated the effect of a long range strain field on the Pendellösung fringes due to a wedge-shaped silicon crystal. He demonstrated a displacement in the position of the fringes, and a decrease in local fringe spacing, with increasing strain.

Green and Tanner [56] have simulated the fringes observed when a crystal is curved cylindrically about an axis perpendicular to the plane of incidence of the

oxide film

silicon
wafer

(a) At oxidation temperature

oxide film

silicon
wafer
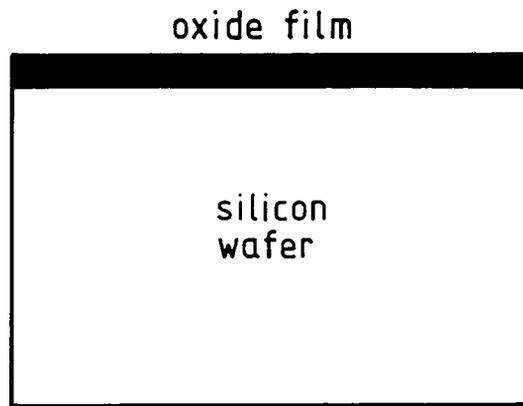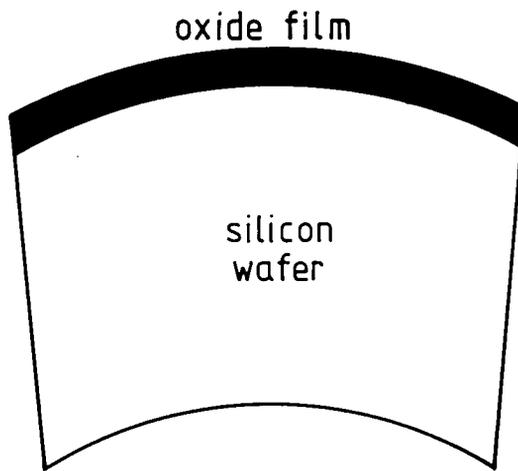
(b) At room temperature

Fig. 5.1: Wafer curvature.

X-rays. Consider polar coordinates (r,θ) centred on the bending axis. Then the radial and tangential components of lattice displacement in a curved crystal are:

$$u_r = 0; \quad u_\theta = (r - r_o)\theta,$$

where r_o = radius of *neutral plane*, in which the circumferential distance between lattice points remains unchanged.

The crystal was taken to be isotropic.

They showed that for the asymmetric $\bar{1}11$ reflection, for a 500 micron thick wafer, the effect of curvature was significant. Decrease in radius of curvature resulted in reduction in the visibility of the Pendellösung fringes and increase in the overall intensity. In addition, the Pendellösung fringes for the symmetric $\bar{2}20$ reflection, for a 200 micron thick wafer, were almost independent of wafer curvature. Both of these results are in agreement with the model of diffraction from curved crystals based on Kato's theory.

However, simulations of the symmetric $\bar{4}22$ reflection did show fringe displacement with increasing wafer curvature. Furthermore, when the $\bar{2}20$ simulation was repeated for a 500 micron thick crystal, variation in Pendellösung fringe structure was also seen. These results are in accordance with the experiments of White and Chen [57], and are due to phase changes in the wavefields, as predicted by Chukhovskii's theory [32,58], which includes second order terms neglected by Kato [53,54].

The purpose of this chapter is to investigate the effect of curvature on the images of precipitates, using simulation techniques.

First of all, the $3\bar{3}\bar{3}$ reflection for the crystal of nominal thickness 792 microns, considered in Chapter 4, was simulated, this time taking into account crystal curvature. A test point was chosen at the crystal surface, 12 microns to the left of the direct beam. Simulations for a precipitate at this point were taken, for the unbent crystal and for a curved crystal with decreasing radius of curvature. The results are shown in Fig. 5.2.

Simulation (b), for 1000m radius of curvature, is almost identical to simulation (a), for the unbent crystal. It is seen that the Pendellösung fringe pattern is displaced, due to phase changes in the wavefields, as a result of decreasing the radius of curvature. This is particularly noticeable when comparing simulations (b) and (c). Also, the dark fringes on either side of the central band become narrower with decreasing radius of curvature. The defect intermediary image is an interference effect and is therefore phase-sensitive. Increase in strain within a crystal affects the phase of the wavefields within the crystal, so it is no surprise that the intermediary image changes with increasing curvature.

Of particular interest is the progressive absence of detail in the images in Figs. 5.2(e) and (f). The reason for this is that increased curvature results in increased strain, which in turn results in increased spatial variation of wave amplitude within the crystal. The resolution (vertical step, ELEM = 4 microns) of the simulations in Fig. 5.2 was insufficient to show up such variations, resulting in reduction, or absence, of detail. This could be remedied by increasing the resolution of the simulations. However, the resulting increase in computational time

radius
of
curvature
(metres)

$\longrightarrow q$

(a)

unbent

(b)

1000

(c)

500

(d)

200

(e)

100

(f)

10
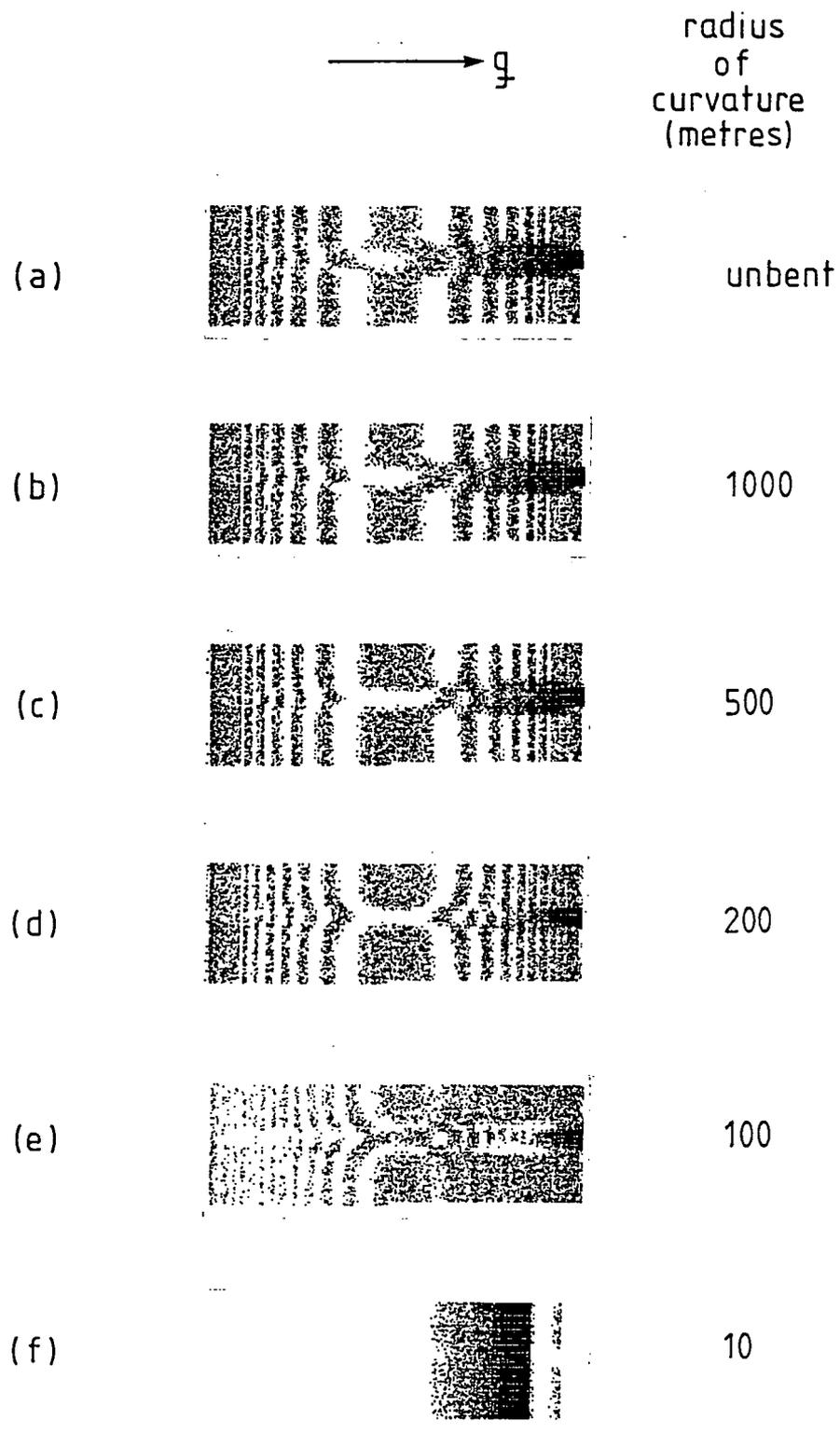
Fig. 5.2: Bent and unbent crystal simulations
for the $3\bar{3}\bar{3}$ reflection.

would be beyond the computing resources available to this project. An alternative is to plot the intensity distributions corresponding to simulation (f) for increased resolution. This is done in Figs. 5.3(a) - (c), using axes of arbitrary units. It is seen that increasing the resolution from 4 microns to 1 micron results in increased integrated intensity and increased uniformity in the intensity distribution.

The next simulations were of the symmetric $4\bar{2}\bar{2}$ reflection for a curved crystal. The geometry of the reflection is shown in Fig. 5.4.

A test point S(15,50) was chosen, in the direct beam. Simulations for a precipitate at this point were taken, for the unbent crystal and for a curved crystal with decreasing radius of curvature. The results are shown in Fig. 5.5.

It is seen that simulation (b), for 1000m radius of curvature, is almost identical to simulation (a), for the unbent crystal. For radii of curvature down to 200m, there is very little change in the simulations. However, subsequent reduction in the radius of curvature results in displacement of the Pendellösung fringe pattern. This complements the results of Green and Tanner [56] and White and Chen [57], illustrating that it is possible to have variation in Pendellösung fringe structure with variation in wafer curvature, for a symmetric reflection. In addition, there is some variation in the intermediary image, illustrating the effect of wafer curvature on phase.

Finally, the $1\bar{1}\bar{1}$ reflection for the crystal of nominal thickness 788 microns was simulated, taking into account crystal curvature. The test point was chosen to be in the direct beam, at 200 microns depth. The simulations are shown in Fig.5.6.

Again, simulation (b), for 1000m radius of curvature, is almost identical to simulation (a), for the unbent crystal. The intermediary image is seen to vary dramatically with increasing curvature. Also, a decrease in radius of curvature results in displacement of the Pendellösung fringes and decrease in the width of the dark fringes on either side of the central band. Again, this illustrates the effect of increased long range strain on Pendellösung fringe structure.
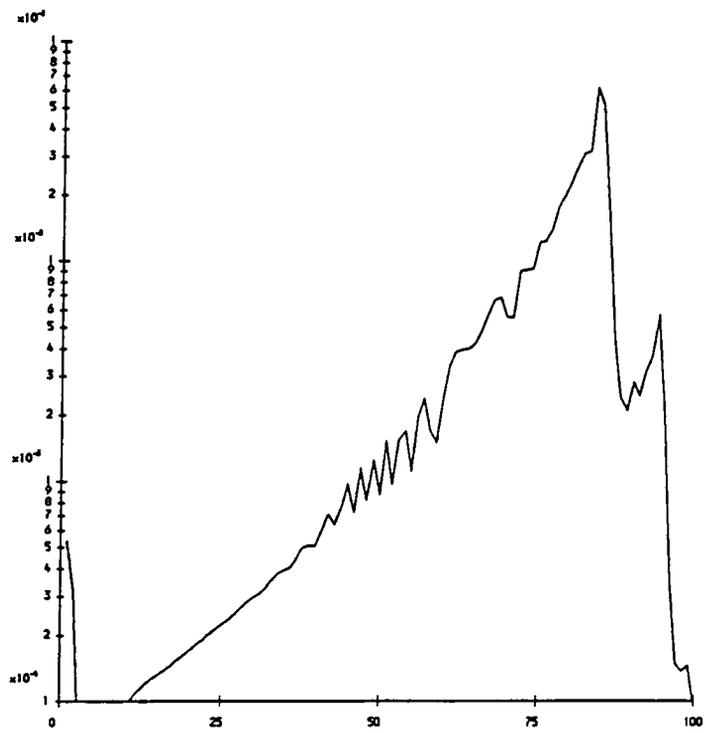
Fig. 5.3(a):   Calculated intensity distribution
               across diffracted beam emerging
               from crystal, (vertical step
               size = 4 microns).
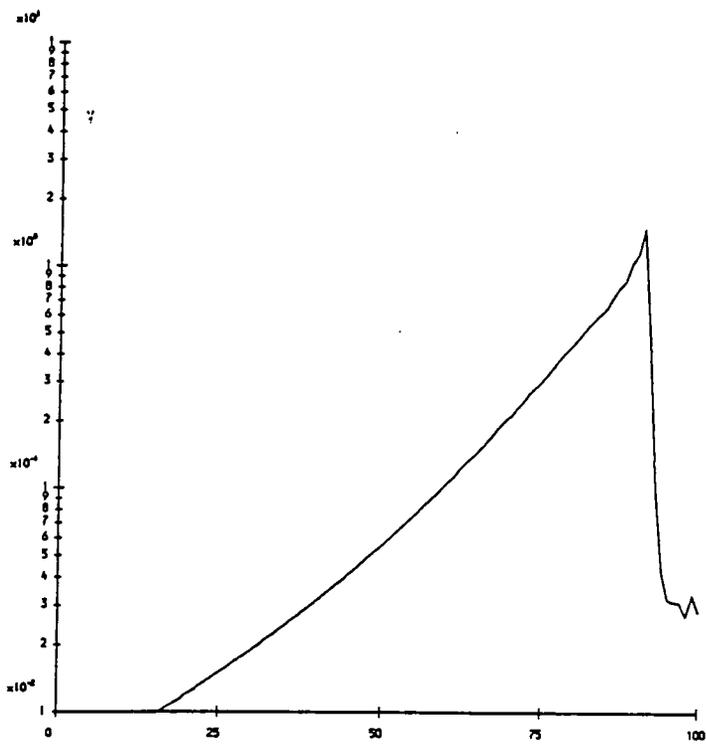
Fig. 5.3(b): Calculated intensity distribution
across diffracted beam emerging
from crystal, (vertical step
size = 2 microns).
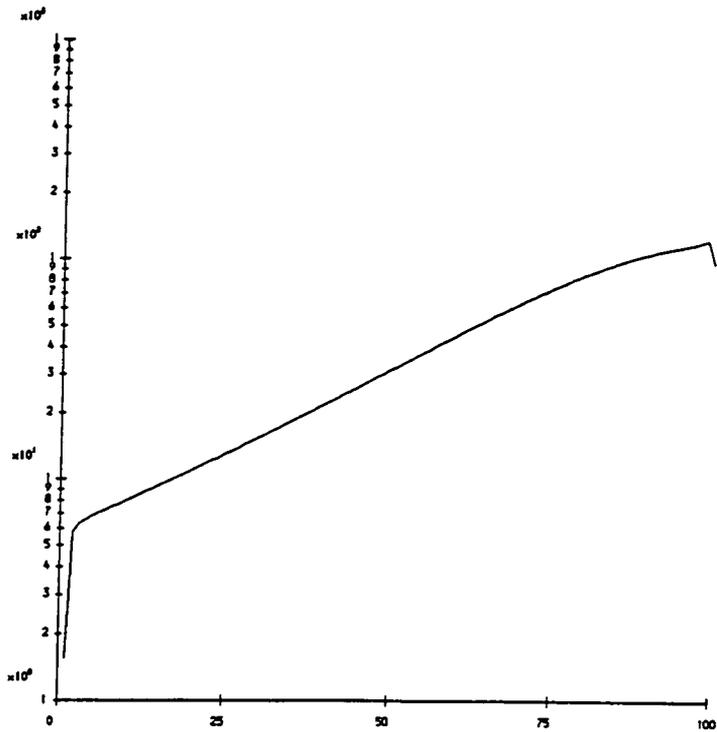
Fig. 5.3(c): Calculated intensity distribution
              across diffracted beam emerging
              from crystal, (vertical step
              size = 1 micron).
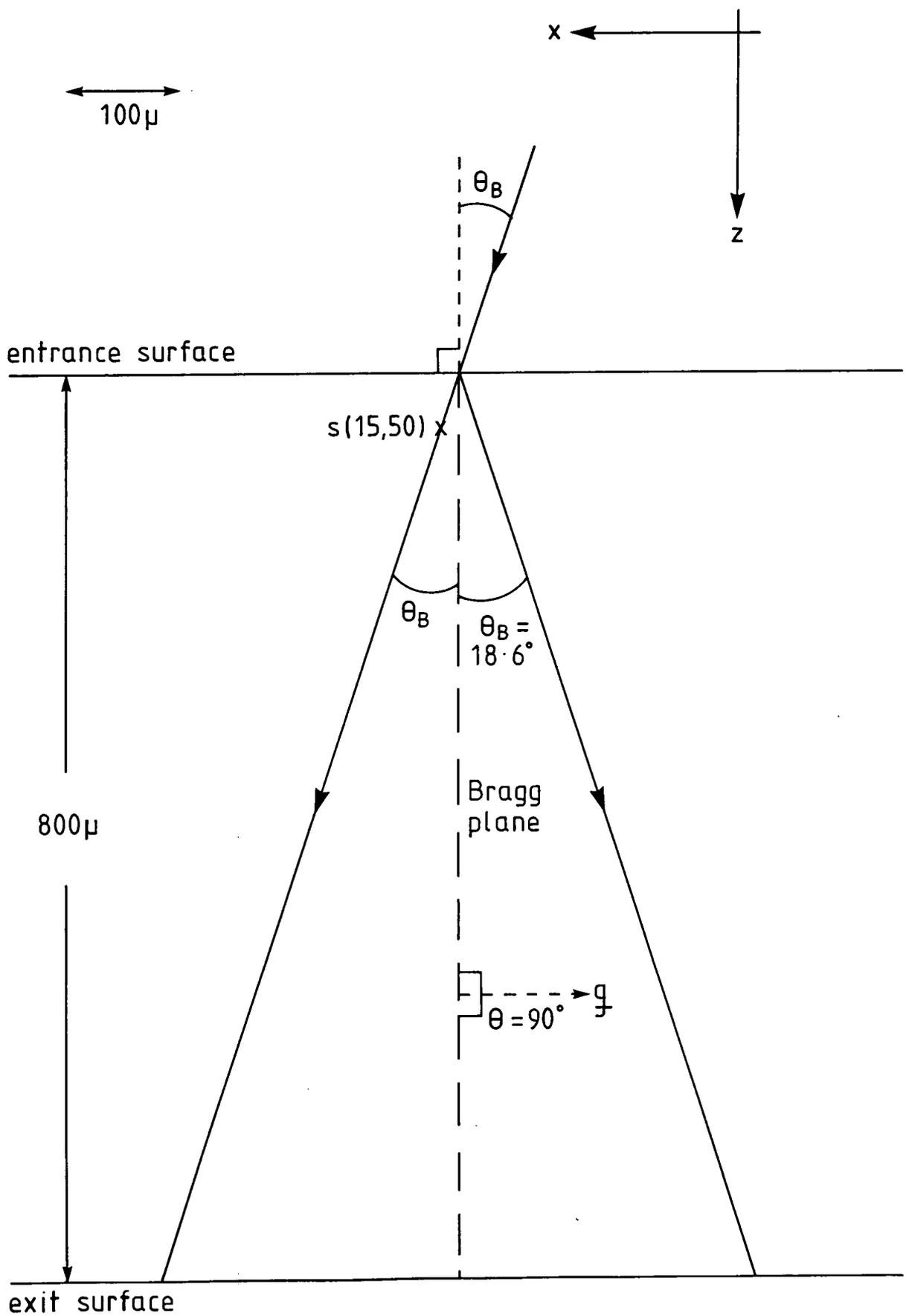
Fig. 5.4: $4\bar{2}\bar{2}$ reflection, (800 micron crystal).

radius
of
curvature
(metres)

(a)   unbent

(b)   1000

(c)   500

(d)   200

(e)   100

(f)   50
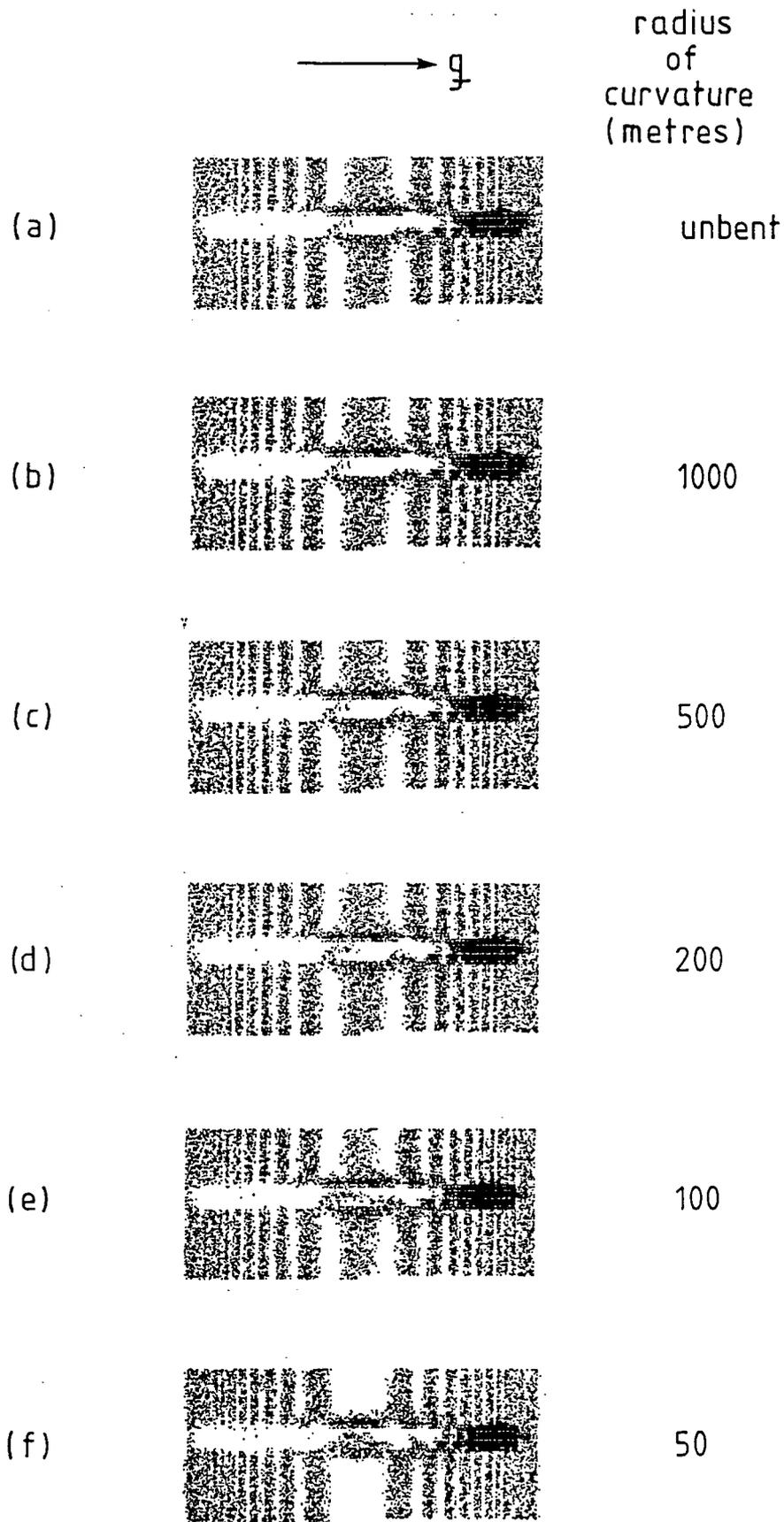
Fig. 5.5:   Bent and unbent crystal simulations
for the $4\bar{2}\bar{2}$ reflection.

radius
of
curvature
(metres)

(a)   unbent

(b)   1000

(c)   500

(d)   200

(e)   100

(f)   50
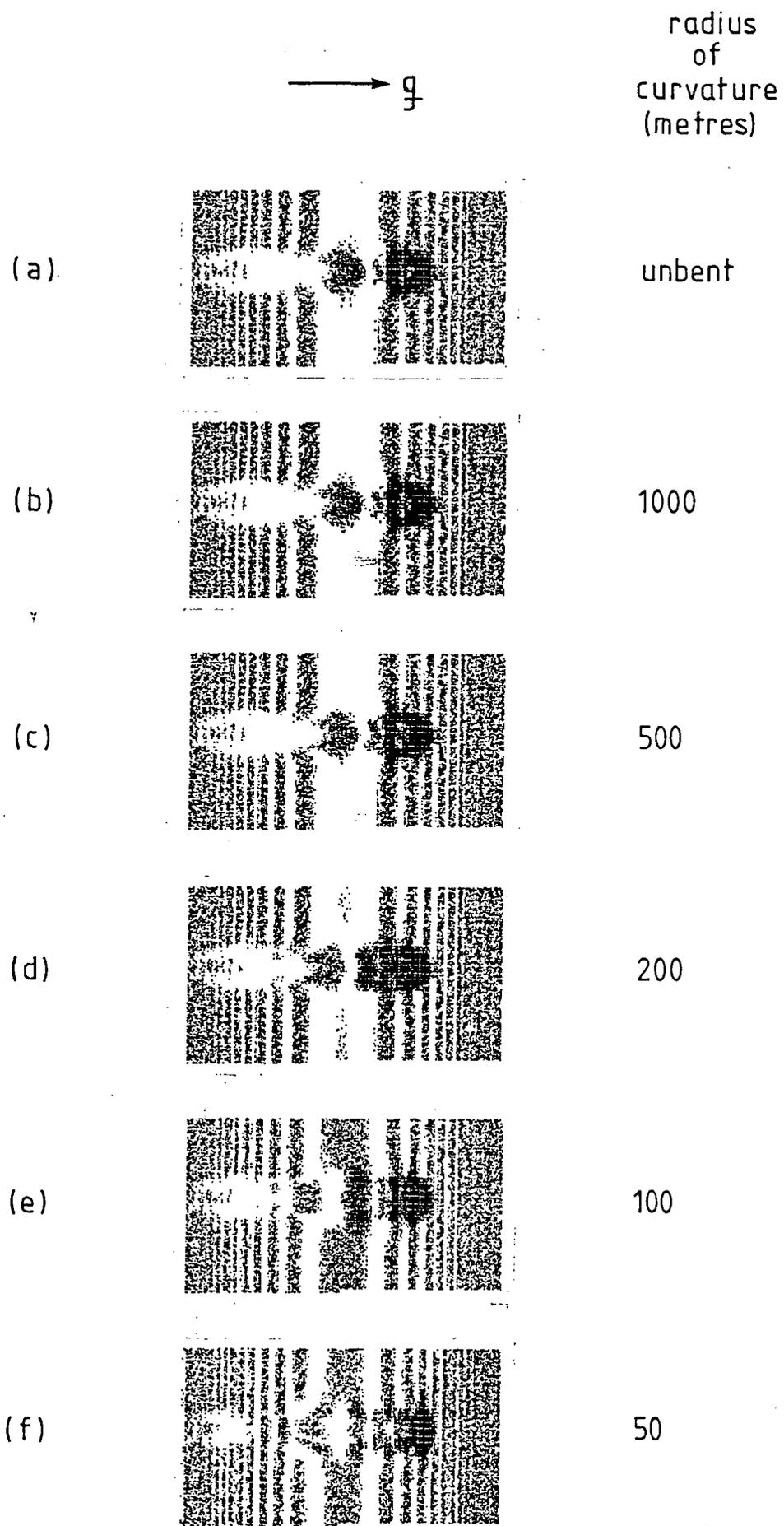
Fig. 5.6: Bent and unbent crystal simulations for the $1\bar{1}\bar{1}$ reflection.

Chapter 6

Conclusions

Simulation of X-ray section topographs has been shown to be a powerful tool in the analysis of silicon crystals containing hydrogen precipitates. By comparing simulations with the corresponding experimental images, it is possible to obtain useful information on the defect.

Simulated and experimental images were successfully matched, for the $3\bar{3}\bar{3}$ reflection (Fig. 4.7) and for the $1\bar{1}\bar{1}$ reflection (Fig. 4.9). In both cases, matching of the experimental and simulated images allowed the defect position to be located. The reversal of Pendellösung fringe contrast upon increase in crystal thickness by half of an extinction distance is clearly shown in Fig. 4.6.

Surface relaxation was incorporated into the simulation program, and its effect was found to decrease with depth. Evidently, surface relaxation has an appreciable effect on simulations of precipitates close to the surface (Appendices B and C). For the sort of precipitates studied in this project, the deformation parameter, C, was equal to 5×10^{-20}. For this value of C, the depth at which the effect of surface relaxation becomes negligible was found to be between 40 and 50 microns (Figs. 4.16(a) and 4.16(b)). The part of a crystal which is of interest is the top 10 microns, since this is the layer in which circuits are built. For this reason, it is important that surface relaxation be incorporated into simulation programs.

Comparison of Fig. 4.16(a) with Fig. 4.16(b) shows that the effect of surface relaxation varies with depth in the crystal, and not with displacement parallel to the entrance surface.

Simulations for precipitates in bent crystals were produced. Unbent crystal simulations were compared with simulations for a bent crystal at different radii of curvature. This was done for the $3\bar{3}\bar{3}$ (Fig. 5.2), $4\bar{2}\bar{2}$ (Fig. 5.5) and $1\bar{1}\bar{1}$ (Fig. 5.6) reflections.

Simulations for a bent crystal at 1000m radius of curvature were almost identical to the simulations for the unbent crystal. This was true for all three reflections.

For the $3\bar{3}\bar{3}$ and $1\bar{1}\bar{1}$ reflections, decreasing the radius of curvature was found to result in displacement of the Pendellösung fringes, and a reduction in the width of the dark fringes on either side of the central band. Even in the special case of the symmetric $4\bar{2}\bar{2}$ reflection, decreasing the radius of curvature resulted in

displacement of the Pendellösung fringes, due to phase changes in the wavefields, as predicted by Chukhovskii [32,58].

In addition, there was some variation in the intermediary image with decreasing radius of curvature. This is expected, since decreasing the radius of curvature increases the long range strain in the crystal, which in turn affects the phase of the wavefields which give rise to the intermediary image.

Decrease in radius of curvature can result in loss of detail in simulations. This is because increased long range strain results in increased variation of the wave amplitudes, so that, without decrease in integration step to accommodate this increased variation, there will be progressive loss of detail. This is illustrated in Fig. 5.2, for a vertical step size of 4 microns. Intensity distribution plots for vertical step sizes of 4 microns, 2 microns and 1 micron are given in Fig. 5.3. These show that reduction in step size gives greater integrated intensity and more uniform intensity distribution. Hence, to compensate for the effect of increased curvature, it is necessary to decrease the integration step size.

The work involved in this project could be developed usefully in two ways.

The first priority would be to establish a program to display the amplitude distribution of wavefields inside the crystal. This would highlight the presence of the hyperboloids of revolution which are the loci of amplitude maxima. More importantly, it would enable one to see clearly how the presence of a precipitate affects the flow of energy inside the crystal. This would provide a graphic explanation of how the dark head, light tail and intermediary parts of the defect image are formed.

A second opening for further work is the possibility of decreasing the step size of the C.S.A. used for generating the simulations. Alternatively, a simulation program based on a V.S.A. might be written, in which the step size is automatically selected so as to accommodate local variations in wave amplitudes. Either approach would generate simulations with increased detail and greater accuracy.

Appendix A

A computer program called 'SECTION', written in Pascal, is listed in A1. Its purpose is to calculate the intensity distribution across the diffracted beam emerging from a crystal with a defect. SECTION is used in the simulation of topographs due to hydrogen precipitates in silicon.

A new simulation program, called 'IMAGE', is constructed to take into account surface relaxation. IMAGE is obtained by making some simple alterations to SECTION. These alterations are illustrated in A2.

35

```
program section;

const pi=3.14159;
      maxno=5000;
      resolution=125;

type complex=record re,im:real; end;
     vector=array[1..3] of real;
     carray=array[1..12] of real;
     matrix=array[1..3,1..3] of real;
     wave=array[1..2,1..maxno] of complex;
     big=array[1..500] of real;
     oarray=array[1..resolution] of real;
     ofile=file of oarray;
     barray=array[1..1500] of real;

var io:integer;

    (*  Setup routine  *)
    defect_code:integer;
    lambda,theta,alpha,absorb,thickness,deltat,width,kappa:real;
    p,q,dir,alt,dv1,dv2,point_separation:real;
    beta,dielep,dieleq,qhio,qhip,qhim:complex;
    lmaxt:integer;

    patry,height,pzy,pas:real;
    ang,param,rn,rf:vector;


    (*  Integration routine  *)
    as,plane:integer;
    xd0,yd0,zd0,depth,dsh:real;                                    (a)

    k:integer;
    rl:real;

    (*  Integration parameters  *)
    elem,transv,sq2:real;
    ap1,ap2,xdis,zdis,diz,dix:real;
    c,shx1,shx3,xppt,yppt,zppt:real;
    xcurve,radius:real;
    co3,co4,co5:vector;
    gd:vector;
    maxplane,lmin,limbe,lmax:integer;
    c1,c2,a,b,ab:complex;
    da:matrix;
    cn:carray;

    (*  Results parameters  *)
    data:ofile;
    mini,maxi:real;
    store1,store2:big;

    dislocation,precipitate,curvature:boolean;
    perfect:boolean;
    factor,fen,fou,field,w1:real;
    i,limit,ip,kperfo,jj,ipl1:integer;
    dum1,dum2,dum3,d,e,f:complex;
    phi:wave;
    reflex:barray;
```

```
procedure dislocn(var da:matrix;var xc,zc,dix,diz:real;
                 var cn:carray;patry,q:real;a,ang,rn,rf:vector);external;

procedure diffdisl(var dsh:real;x1,x2,ap1,ap2:real;co3,co4,co5:vector;
                 cn:carray);external;

procedure pointdef(var c,xc,yc,zc:real;var gd:vector;
                 a,ang,rn,rf:vector);external;

procedure diffpoint(var dsh:real;x,y,z,sh1,sh2,c:real;gd:vector);external;

procedure curvedef(var radius:real;var gd:vector;
                 a,ang,rn,rf:vector);external;

procedure diffcurve(var dsh:real;x,z,sh1,sh2,t,r:real;gd:vector);external;


procedure results(var jj:integer;var store1,store2:big;var data:ofile;
var mini,maxi:real;reflex:barray;
kperfo,limit,ip,io:integer);external;

procedure trap;
begin
end;

   procedure cmult(a,b:complex;var c:complex);external;
   procedure cadd(a,b:complex;var c:complex);external;
   procedure csub(a,b:complex;var c:complex);external;
   procedure cdiv(a,b:complex;var c:complex);external;

procedure integrate;

var dum1,dum2,dum3,d,e,f:complex;
    ks,as,l,k:integer;
    x,dc1,dc2,temp,y,z,xi,zd1,zd2,r1,aa:real;

BEGIN   (* integration *)
    ip:=ip-1;
    temp:=0;
  (*core(plane);*)
  (*begin         *)
    if dislocation then begin
       aa:=yd0-plane;
       xd0:=xdis+aa*dix;
       zd0:=zdis+aa*diz;
       yd0:=2;
    end;
  (*end;          *)
    y:=plane*patry;   (* ???? - *)
    r1:=1;
    for k:=limbe to maxno-1 do begin   (* b.c.s at entrance surface *)
      phi[1,k].re:=field*r1;
      phi[1,k].im:=0;
      r1:=r1*fen;
      phi[2,k].re:=0;
      phi[2,k].im:=0;
    end;
    depth:=0;
    for l:=lmin to lmax do begin  (* loop for each layer *)
```

```
      depth:=depth+elem;
      xi:=-depth*sin(alpha)/cos(alpha)+sq2;
      limit:=maxno-1;
      phi[1,limit].re:=0;
      phi[1,limit].im:=0;
      phi[2,limit].re:=0;
      phi[2,limit].im:=0;
      as:=0;
      x:=xi;
      z:=depth-0.5*elem;
if dislocation then begin
      zd1:=da[1,3]*(z-zd0);
      zd2:=da[2,3]*(z-zd0);
end;
            for ks:=limit to maxno-1 do begin   (* loop for each node in a layer *)
              as:=as+1;
              x:=x-transv;
              if dislocation then begin
                  dc1:=da[1,1]*(x-xd0)+zd1;
                  dc2:=da[2,1]*(x-xd0)+zd2;
                end;
              if perfect then dsh:=0
              else begin
              if dislocation then   diffdisl(temp,dc1,dc2,ap1,ap2,co3,co4,co5,cn);
              if precipitate then begin
                              diffpoint(dsh,x-xppt,y-yppt,z-zppt,shx1,shx3,c,gd);_____ (b)
                              dsh:=q*pi*dsh;
                           end else dsh:=0;
(*      if (precipitate and curvature) then temp:=dsh;       26 Apr 89   *)
              if precipitate then temp:=dsh;
              if curvature then begin
                              diffcurve(dsh,x-xcurve,z,shx1,shx3,thickness,radius,gd);
                              dsh:=q*pi*dsh;
                           end else dsh:=0;
(*      if precipitate or curvature then    dsh:=q*pi*dsh else dsh:=0;   *)
(*      if (precipitate and curvature) then dsh:=dsh+temp; 26 Apr 89   *)
              if precipitate then dsh:=dsh+temp;
              if dislocation then   dsh:=temp+dsh;
                end;
              dsh:=dsh+w1;
              c1.im:=dsh;
              c2.im:=-dsh;
              csub(c1,ab,d);

              cmult(a,phi[2,ks+1],dum1);
              cadd(dum1,phi[1,ks+1],e);
              cmult(b,phi[1,ks],dum1);
              cmult(c2,phi[2,ks],dum2);
              cadd(dum1,dum2,f);
              cmult(c1,e,dum1);
              cmult(a,f,dum2);
              cadd(dum1,dum2,dum3);
              cdiv(dum3,d,phi[1,ks]);
              cmult(b,e,dum1);
              cadd(dum1,f,dum2);
              cdiv(dum2,d,phi[2,ks]);
          end;  (* ks *)
        end;   (* l *)
  if plane=1 then writeln('range on bottom ',(xi-transv-sq2)*1e06:2:1,
                          '  ',(x-sq2)*1e06:2:1);
```

```
END;  (* integration *)


procedure display;
begin
  writeln;
  writeln('   SECTION TOPOGRAPH SIMULATION');
  writeln;
  writeln('wavelength ',lambda*1e10:1:4,' Angstrom');
  writeln('bragg angle ',180*theta/pi:3:2,' degrees');
  writeln('psi zero ',180*alpha/pi:3:2,' degrees');  writeln;
(*writeln('mu ',absorb:1:4);
  writeln('beta ',beta.re,'   ',beta.im);
  writeln('chi h + ',qhip.re,'   ',qhip.im);
  writeln('chi h - ',qhim.re,'   ',qhim.im);
  writeln('chi o   ',qhio.re,'   ',qhip.im);        *)
  writeln('slab thickness ',elem*1e06:1:2,' micron');
  writeln('sample thickness ',thickness*1e06:1:1,' microns');  writeln;
  writeln('transverse step ',transv*1e06:1:2,' microns');
  writeln('transverse printed step ',point_separation*1e06:1:2,' microns');
  writeln;
  writeln('slit width ',width*1e06:1:1,' microns');  writeln;
(*writeln('a= ',param[1]:1:3,' 10(-4) microns');
  writeln('b= ',param[2]:1:3,' 10(-4) microns');
  writeln('c= ',param[3]:1:3,' 10(-4) microns');
  writeln('cos a= ',ang[1]:1:2,'  cos b= ',ang[2]:1:2,
          '  cos c= ',ang[3]:1:2);                        *)
  writeln('surface ',rn[1]:4:0,rn[2]:4:0,rn[3]:4:0);
  writeln('reflection ',rf[1]:4:0,rf[2]:4:0,rf[3]:4:0);  writeln;
  writeln('image height ',height*1e06:1:1,'  microns');
  writeln('image point separation ',patry/2*1e06:1:2,'  microns');  writeln;
  writeln(maxplane:5,' calculated planes of incidence');
end;


procedure setup;
var i:integer;
begin
  dislocation:=false;
  precipitate:=false;
  curvature:=false;
  read(defect_code);                              (* *)
  if defect_code=1 then  dislocation:=true;
  if defect_code=2 then  precipitate:=true;
  if defect_code=4 then  curvature:=true;
  if defect_code=5 then begin dislocation:=true;
                              curvature:=true; end;
  if defect_code=6 then begin precipitate:=true;
                              curvature:=true; end;
readln(defect_code); if defect_code=0 then perfect:=false else perfect:=true;
(*rewrite(data,'FILE=output.dat');*)
  rewrite(data,'unit=2');         (*  15 Oct 87  *)
  readln(KPERFO);  io:=0;
  readln(lambda,theta,alpha,absorb);
  readln(QHIO.re);
  readln(QHIM.re,QHIM.im);
  readln(QHIP.re,QHIP.im);
  readln(elem,thickness,deltat,width);
  readln(param[1],param[2],param[3],ang[1],ang[2],ang[3]);
  readln(rn[1],rn[2],rn[3],rf[1],rf[2],rf[3]);
```

```
  readln(height,pzy);

(*********************************)
(*                               *)
(*        Geometry constants     *)
(*                               *)
(*********************************)

  kappa:=pi/lambda;
  dir:=(alpha+2*theta)*pi/180;
  alt:=(alpha+theta)*pi/180;
  alpha:=alpha*pi/180;
  theta:=theta*pi/180;


(*********************************)
(*     Integration parameters    *)
(*********************************)

  transv:=elem*((sin(dir)/cos(dir))-(sin(alpha)/cos(alpha)));
  sq2:=0.5*elem*sin(dir)/cos(dir);
  p:=elem/cos(alpha);
  q:=elem/cos(dir);
  dv1:=pi*p/(2*lambda);
  dv2:=pi*q/(2*lambda);
  beta.re:=-deltat*sin(2*theta)-0.5*QHIO.re*(cos(dir)/cos(alpha)-1);
  beta.im:=0;
  c1.re:=1-kappa*q*beta.im;
  c2.re:=1+kappa*q*beta.im;
  w1:=-kappa*q*beta.re;
  dielep.re:=dv1*QHIM.im;
  dielep.im:=-dv1*QHIM.re;
  dieleq.re:=dv2*QHIP.im;
  dieleq.im:=-dv2*QHIP.re;
  a:=dielep;
  b:=dieleq;
  cmult(a,b,ab);

  point_separation:=transv*kperfo;
  patry:=point_separation*cos(dir)*2;        (* for next line *)

  if dislocation then  dislocn(da,xdis,zdis,dix,diz,cn,patry,q,param,ang,rn,rf);
  if precipitate then  pointdef(c,xppt,yppt,zppt,gd,param,ang,rn,rf);
  if curvature then  curvedef(radius,gd,param,ang,rn,rf);

  if width>transv then xcurve:=-width/2 else xcurve:=0;

  fen:=exp(absorb*sin(alt)*transv/(2*cos(theta)));
  fou:=exp(-absorb*sin(alt)*transv/cos(theta));

(*************************************)
(*   Integration control parameters  *)
(*************************************)

  maxplane:=trunc(height/patry+0.5);
  maxplane:=maxplane+1;

  lmaxt:=trunc(thickness/elem+0.5);
  if transv>width then width:=transv;
  lmin:=trunc(width/transv+1.5);
  if (lmaxt+lmin)>(maxno-1) then lmax:=maxno-2 else lmax:=lmaxt+lmin-1;
```

```
if io=0 then writeln('lmin = ',lmin,' lmax = ',lmax,' ',lmax-lmin+1,' layers');
   limbe:=maxno+1-lmin;

   field:=1/sqrt((lmin-1)*cos(alpha));

display;

for i:=1 to maxno do begin
   phi[1,i].re:=0;
   phi[1,i].im:=0;
   phi[2,i].re:=0;
   phi[2,i].im:=0;
end;
trap;


(*********************************)
(*      Diff (dsh)  parameters      *)
(*********************************)

   shx1:=-sin(dir);        (* 9/3/88  shx1:=abs(cos(dir));  *)
   shx3:=cos(dir);         (* 9/3/88  shx2:=-abs(sin(dir)); *)


if dislocation then begin
   for i:=1 to 3 do begin
      co3[i]:=cn[i]*(sqr(cn[i+6])+cn[i+9]);
      co4[i]:=2*cn[i+3]*cn[i+6];
      co5[i]:=sqr(cn[i+6])+cn[i+9];
   end;
   ap1:=da[1,3]*abs(cos(dir))-da[1,1]*abs(sin(dir));
   ap2:=da[2,3]*abs(cos(dir))-da[2,1]*abs(sin(dir));
   writeln('WARNING   ignore what follows');
end;
   yd0:=2;       (* *)
   ip:=2;
   if io=0 then writeln(maxplane,' planes of incidence');
   dsh:=0;
end;


(*******************************************)
(*               Main Program                *)
(*******************************************)

begin
   setup;

if dislocation then begin
   writeln('position of dislocation in first plane');
   writeln('x = ',xdis);
   writeln('z = ',zdis);
end;

   for plane:=1 to maxplane do begin    (* loop for each plane of incidence *)
      integrate;
      factor:=exp(-absorb*depth/cos(alpha));

      jj:=kperfo;
      r1:=1;
      for k:=limit to 4999 do begin
         jj:=jj+1;
         reflex[jj]:=factor*r1*(sqr(phi[2,k].re)+sqr(phi[2,k].im));
```

```
      r1:=r1*fou;
    end;

    results(jj,store1,store2,data,mini,maxi,reflex,kperfo,limit,ip,io);
    if perfect then perfect:=false;

  end; (*  plane  *)

if dislocation then begin
  writeln('position of dislocation in last plane');
  writeln('x = ',xd0);
  writeln('z = ',zd0);
end;

  results(jj,store1,store2,data,mini,maxi,reflex,kperfo,limit,200,io);
  close(data);
end.
```

```
xd0,yd0,zd0,depth,dsh,dshnew:real;                                    (a')


     if precipitate then begin
               diffpoint(dsh,x-xppt,y-yppt,z-zppt,shx1,shx3,c,gd);      (b')1
               diffpoint(dshnew,x-xppt,y-yppt,z+zppt,shx1,shx3,c,g
d);                                                                      (b')2
               dsh:=dsh+dshnew;                                         (b')3
```

Appendix B

Simulations with and without surface relaxation are compared for precipitates at different depths along the direct beam. This is done for five different values of deformation parameter.

depth
of
precipitate
(microns)

5

10

20

30

50

without
surface
relaxation

with
surface
relaxation

B1:   Deformation parameter = 5×10^{-21}.

depth
of
precipitate
(microns)

g

10

20

30

40

50

without
surface
relaxation

with
surface
relaxation

B2:   Deformation parameter = 1.7×10^{-20}.

depth
of
precipitate
(microns)

$\longrightarrow$ g

10

20

30

40

50
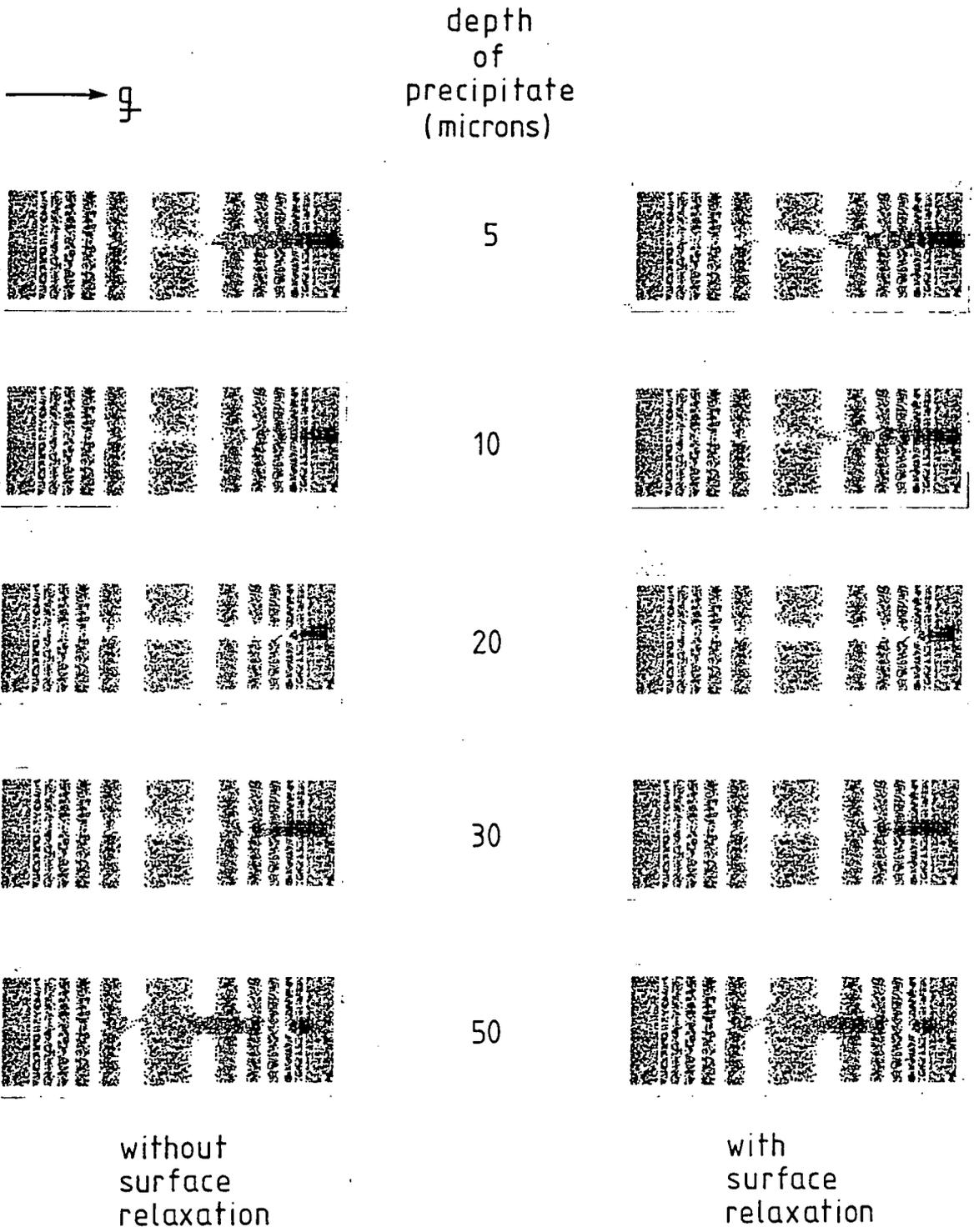
without
surface
relaxation
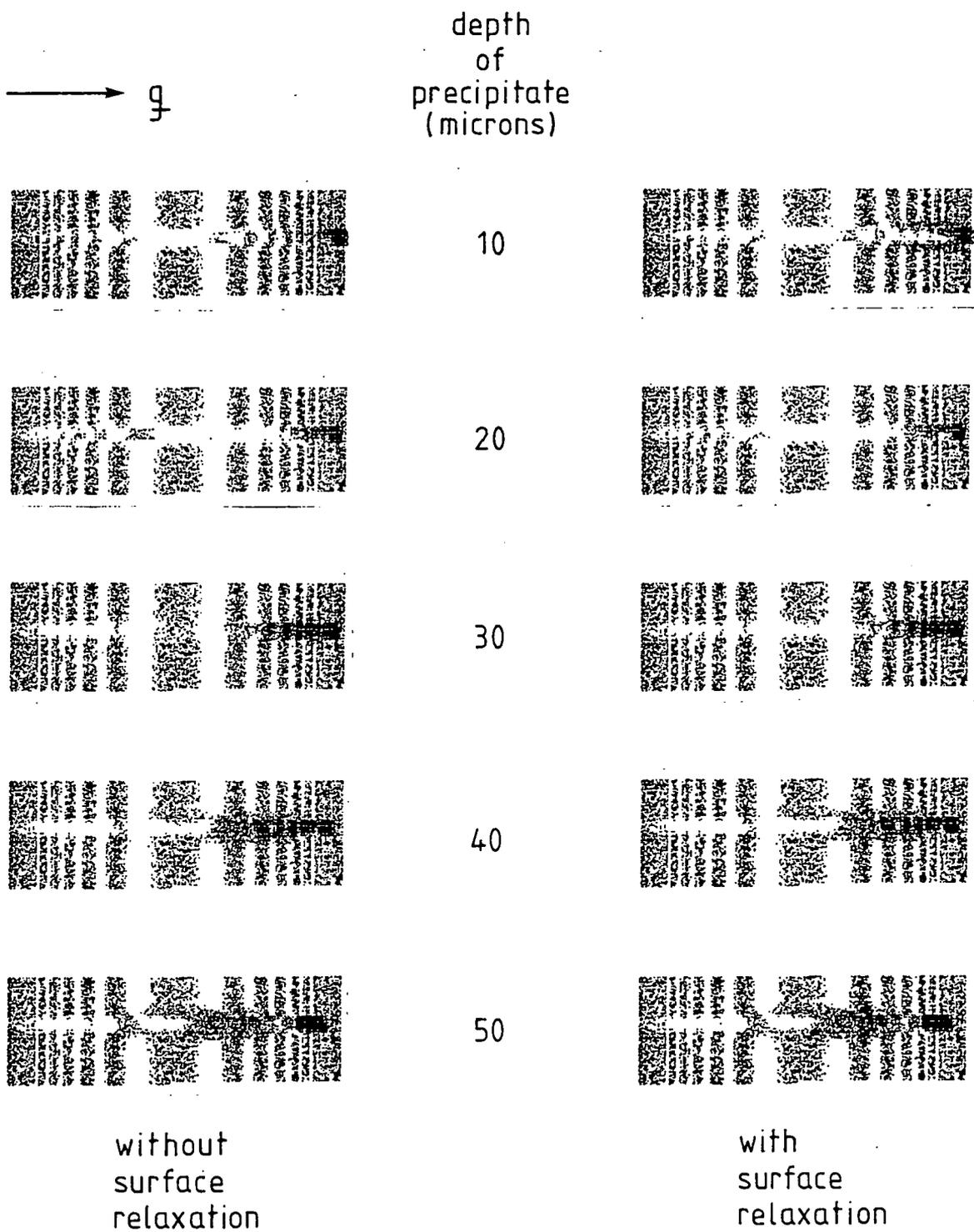
with
surface
relaxation
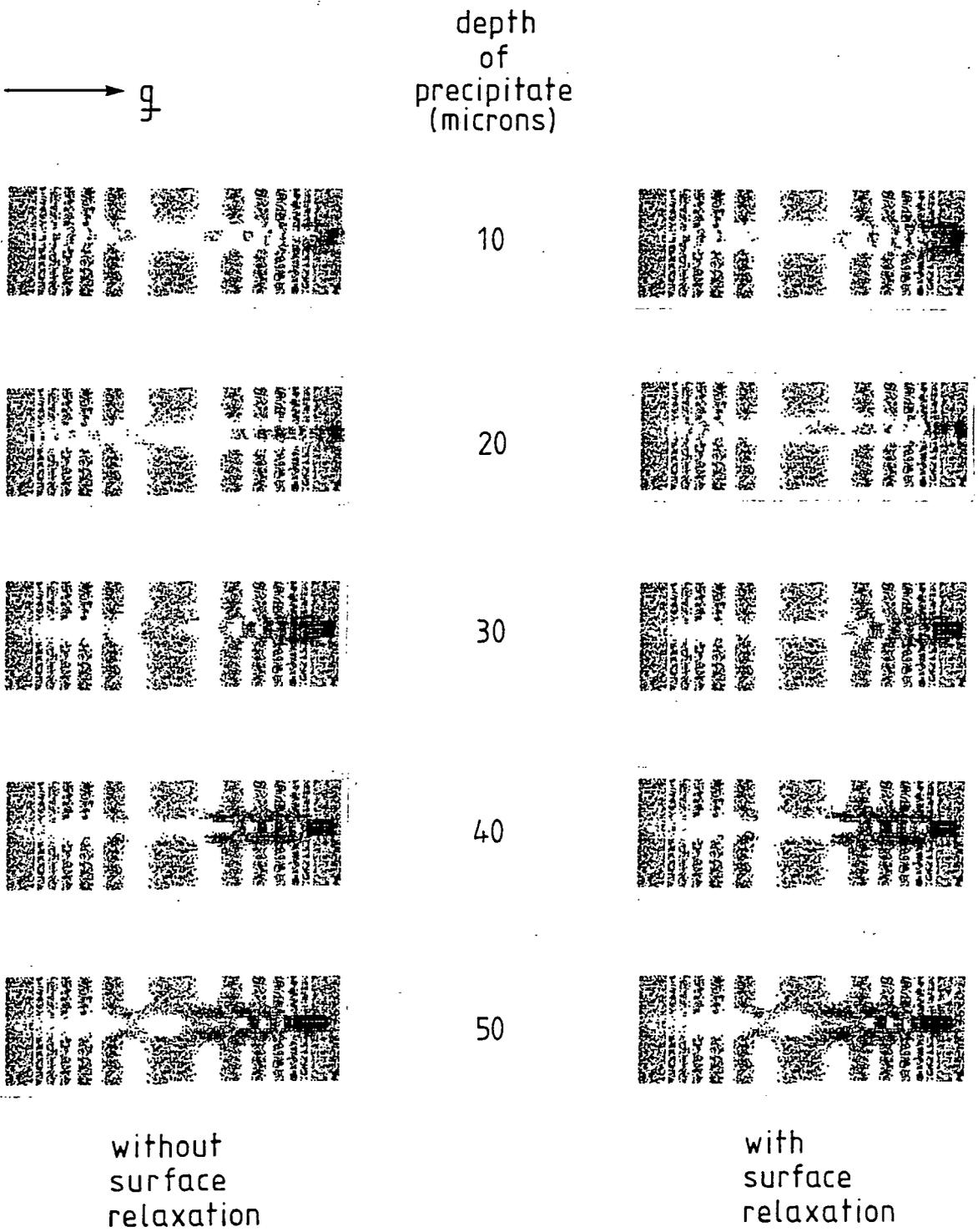
B3:   Deformation parameter = 5×10^{-20}.

depth
of
precipitate
(microns)

→ g
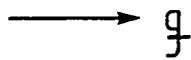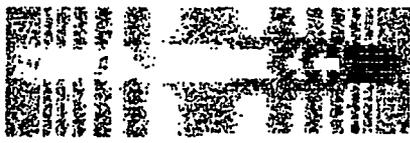
50
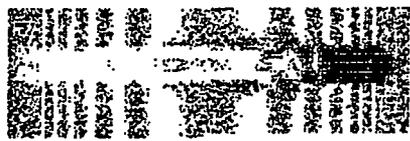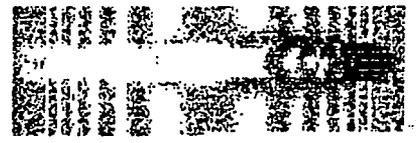
60
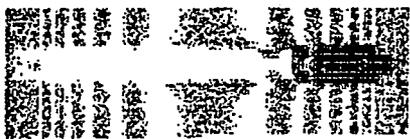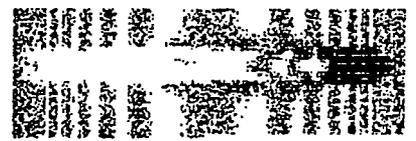
70
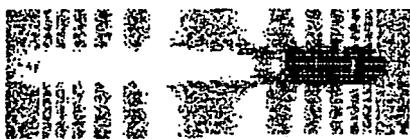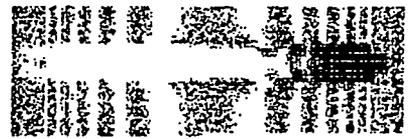
80
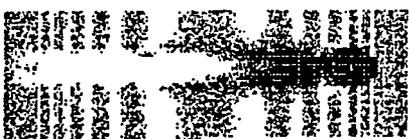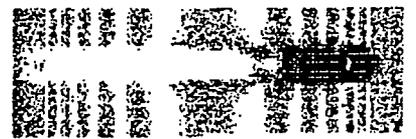
90
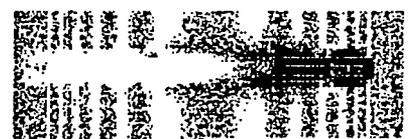
without
surface
relaxation

with
surface
relaxation

B4:   Deformation parameter = 1.5×10^{-19}.

depth
of
precipitate
(microns)

→ g

50

100

110

120

130

without
surface
relaxation

with
surface
relaxation
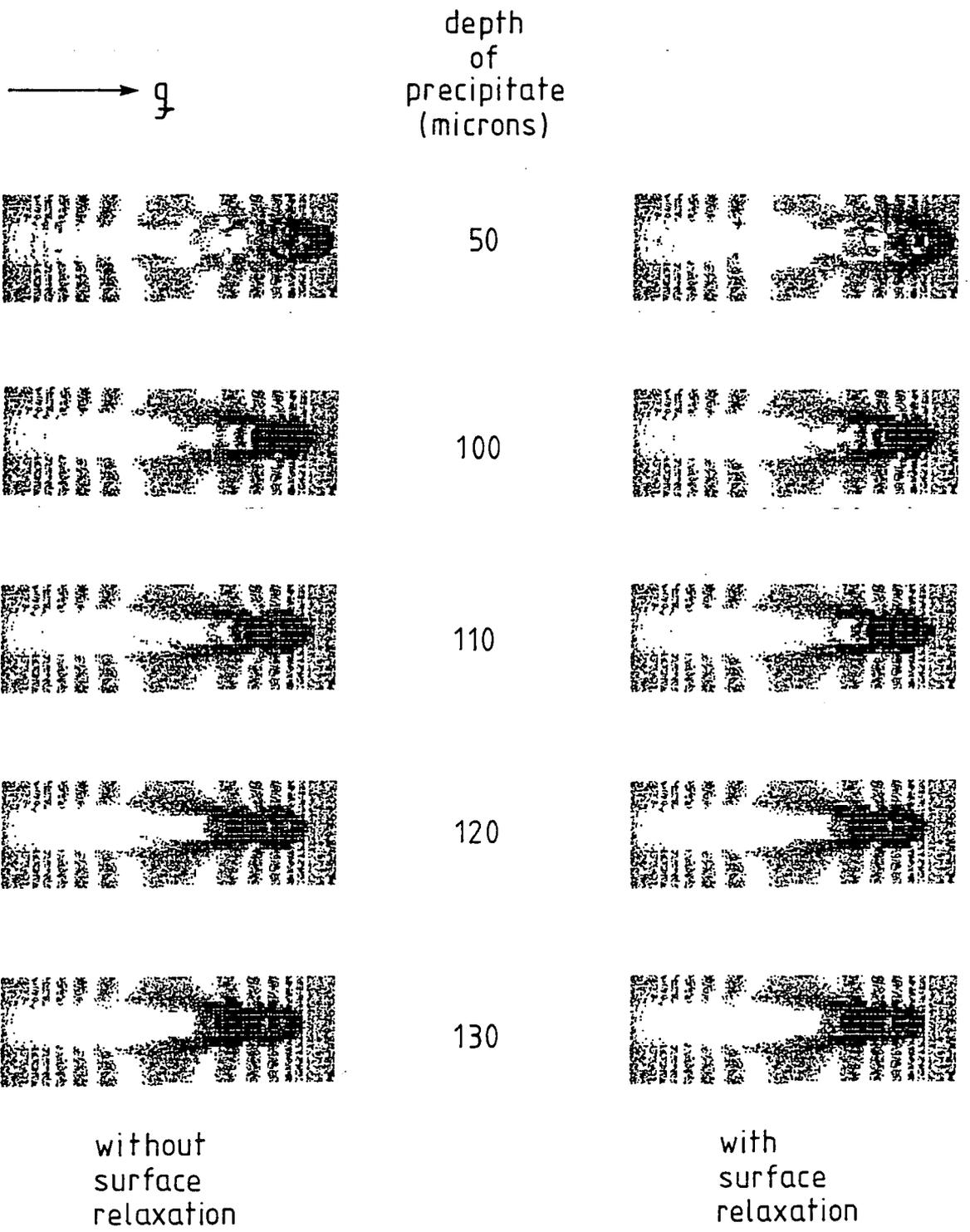
B5: Deformation parameter = 5 x 10^{-19}.

Appendix C

Simulations with and without surface relaxation are compared for precipitates at different depths along a Bragg plane. This is done for five different values of deformation parameter.
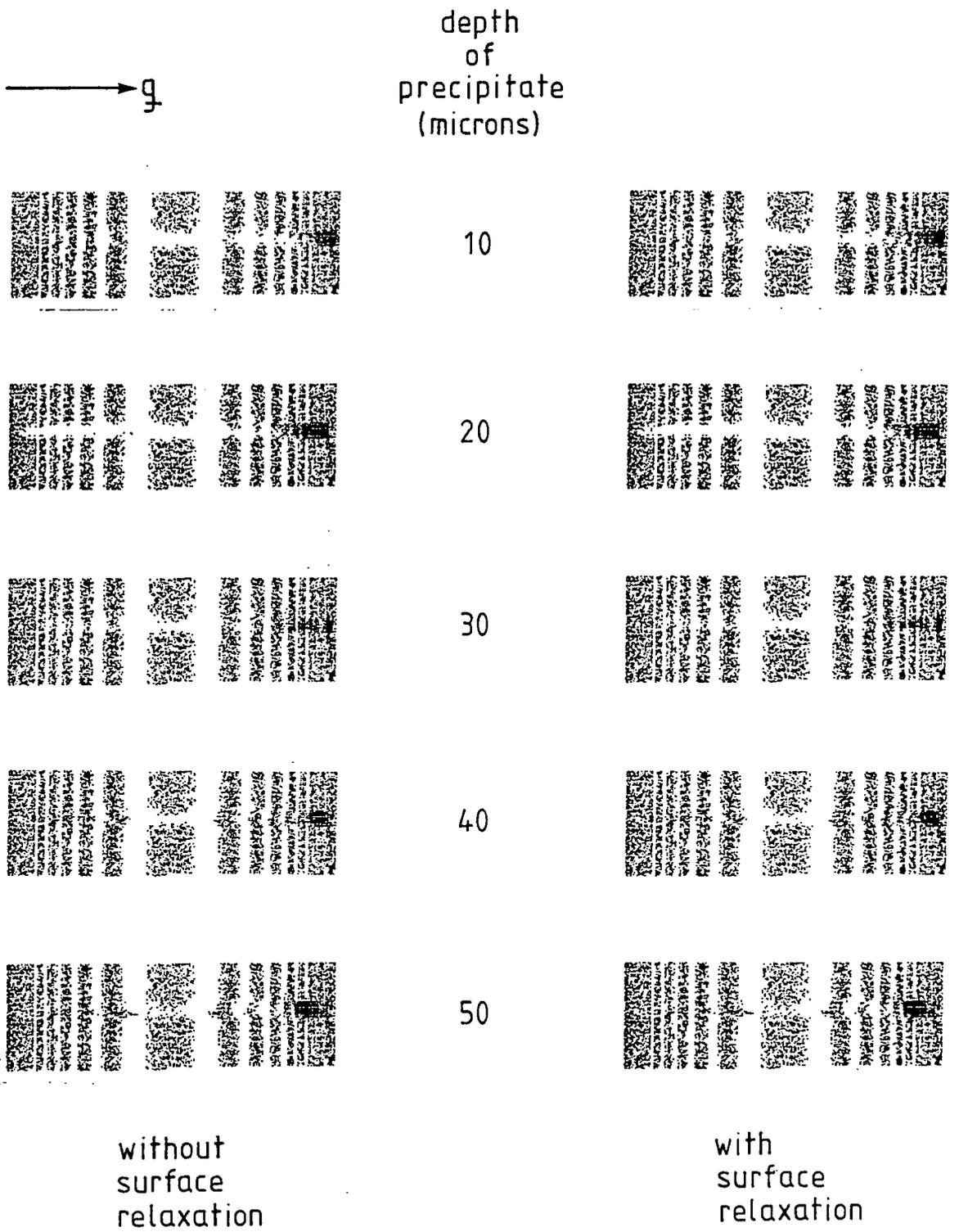
depth
of
precipitate
(microns)

$\longrightarrow \underline{g}$

10

20

30

40

50

without
surface
relaxation

with
surface
relaxation

C1:   Deformation parameter = 5 x 10^{-21}.

depth
of
precipitate
(microns)

$\longrightarrow$ g

10

20

30

40

50

without
surface
relaxation

with
surface
relaxation

C2: Deformation parameter = 1.7×10^{-20}.

depth
of
precipitate
(microns)

$\longrightarrow$ g

10

20

30

40

50

without
surface
relaxation

with
surface
relaxation

C3: Deformation parameter = 5×10^{-20}.

depth
of
precipitate
(microns)

30

50

60

70

80

without
surface
relaxation

with
surface
relaxation

C4:   Deformation parameter = 1.5×10^{-19}.

depth
of
precipitate
(microns)

⟶ g

without surface relaxation	depth of precipitate (microns)	with surface relaxation
	50	
	100	
	120	
	140	
	150	
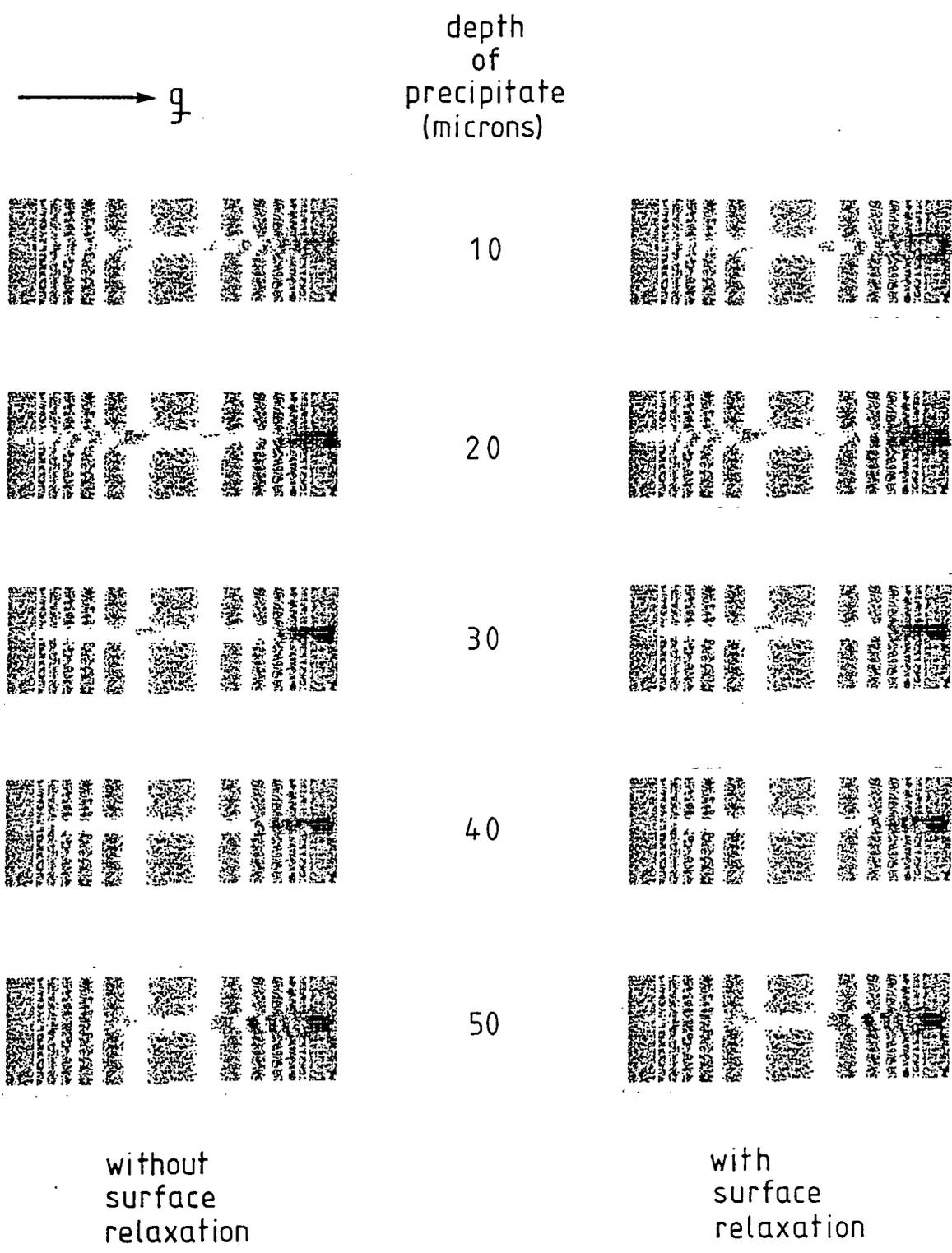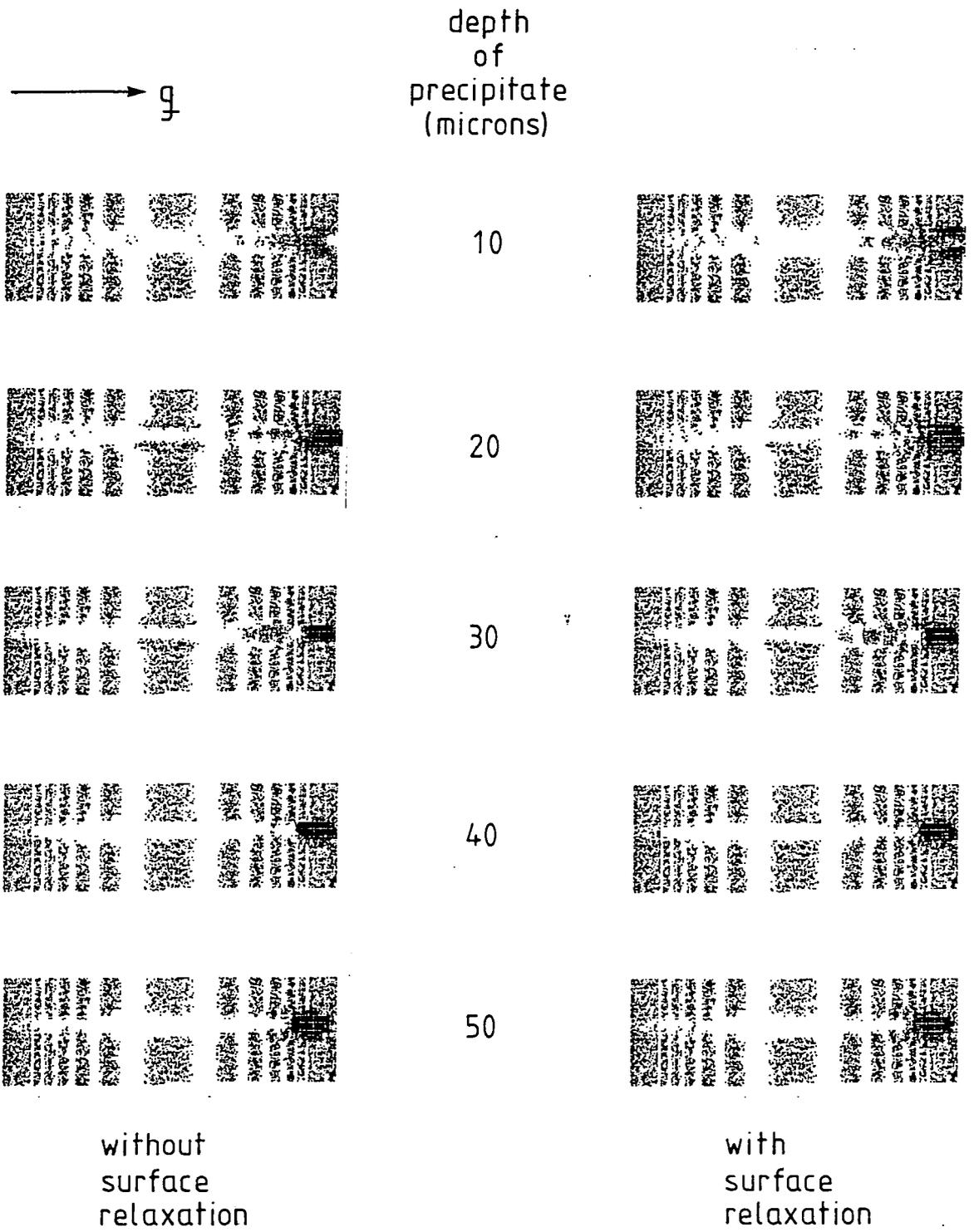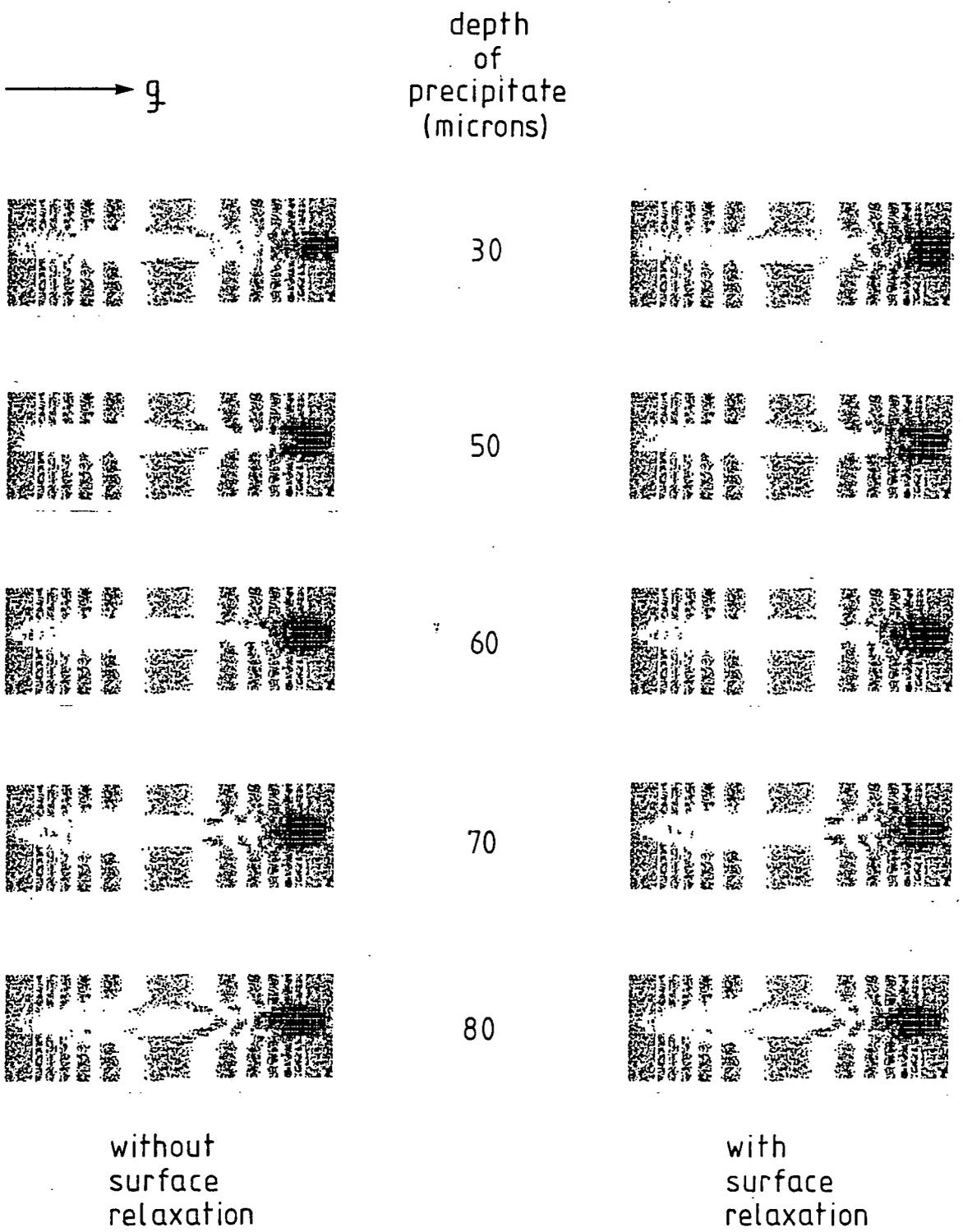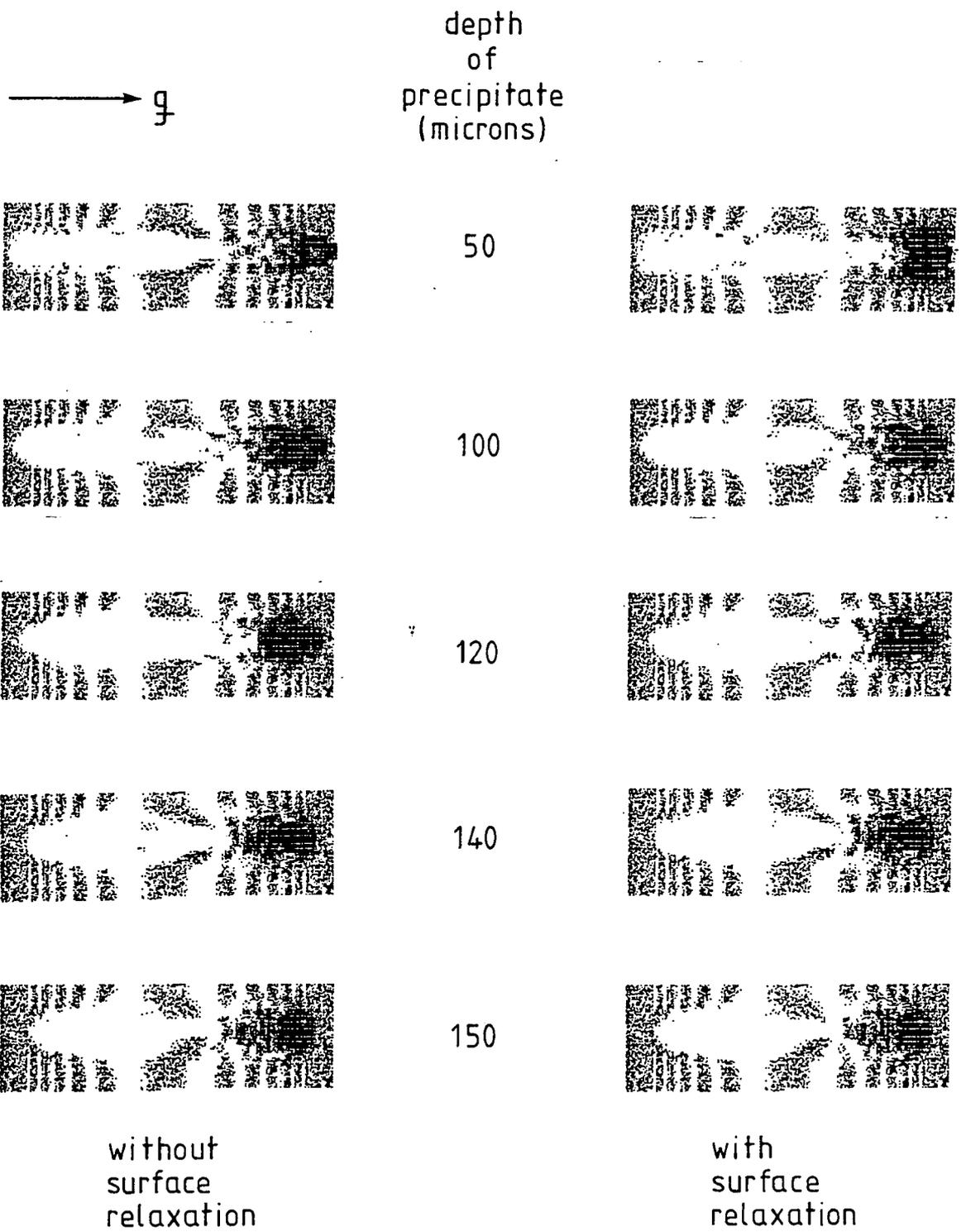
C5:   Deformation parameter = 5×10^{-19}.

Bibliography

[1] B.K. Tanner, (1976), *X-ray Diffraction Topography*, Pergamon, Oxford.

[2] A.R. Lang, (1978), *Diffraction and Imaging Techniques in Material Science*, Vol. II, 2nd rev. ed. (ed. S. Amelinckx, R. Gevers and J. Van Landuyt), North-Holland, p.623.

[3] U. Bonse, M. Hart and J.B. Newkirk, (1967), Adv. X-ray Analysis, Plenum, **10**, 1.

[4] A. Authier, (1967), Adv. X-ray Analysis, Plenum, **10**, 9.

[5] N. Kato and A.R. Lang, (1959), Acta Cryst., **12**, 787.

[6] A.R. Lang, (1958), J. Appl. Phys., **29**, 597.

[7] A.R. Lang, (1959), Acta Cryst., **12**, 249.

[8] A.R. Lang, (1957), Acta Cryst., **10**, 839.

[9] S. Amelinckx, (1964), *The Direct Observation of Dislocations*, (Solid State Physics, Supplement 6), Academic Press, New York.

[10] S. Mardix, (1974), J. Appl. Phys., **45**(11), 5103.

[11] U. Bonse and E. Kappler, (1958), Z. Naturforschung, **13a**, 348.

[12] W.L. Bond and J. Andrus, (1952), Am. Mineralogist, **37**, 622.

[13] T. Tuomi, K. Naukkarinen and P. Rabe, (1974), Phys. Stat. Sol. (a), **25**, 93.

[14] D.K. Bowen, (1988), Adv. Materials Science, Pergamon, **1**, 522.

[15] B.K. Tanner, M. Safa, D. Midgley and J. Bordas, (1976), J. Magnetism and Magnetic Materials, North-Holland, **1**, 337.

[16] M. Hart, (1975), J. Appl. Cryst., **8**, 436.

[17] E.S. Meieran, (1980), *Characterization of Crystal Growth Defects by X-ray Methods*, (ed. B.K. Tanner and D.K. Bowen), Plenum, New York, p.1.

[18] Z.G. Pinsker, (1978), *Dynamical Scattering of X-rays in Crystals*, Springer-Verlag.

[19] R.W. James, (1948), *The Optical Principles of the Diffraction of X-rays*, Bell.

[20] M. Hart, (1980), *Characterization of Crystal Growth Defects by X-ray Methods*, (ed. B.K. Tanner and D.K. Bowen), Plenum, New York, p.216.

[21] B.W. Batterman and H. Cole, (1964), Rev. Mod. Phys., **36**(3), 681.

[22] R.D. Heidenreich, (1942), Phys. Rev., **62**, 291.

[23] J.M. Cowley and A. Moodie, (1957), Proc. Phys. Soc., **B70**, 486.

[24] J.M. Cowley and A. Moodie, (1957), Acta Cryst., **10**, 609.

[25] P. Hirsch, A. Howie and M.J. Whelan, (1960), Trans. Roy. Soc., **A252**, 499.

[26] A. Howie and M.J. Whelan, (1961), Proc. Roy. Soc., **A263**, 217.

[27] A. Howie and M.J. Whelan, (1962), Proc. Roy. Soc., **A267**, 206.

[28] S. Takagi, (1962), Acta Cryst., **15**, 1131.

[29] S. Takagi, (1969), J. Phys. Soc. Jpn., **26**, 1239.

[30] D. Taupin, (1964), Bull. Soc. Fr. Min. Crist., **87**, 469.

[31] T. Uragami, (1969), J. Phys. Soc. Jpn., **27**, 147.

[32] F.N. Chukhovskii and P.V. Petrashen, (1977), Acta Cryst., **A33**, 311.

[33] F. Balibar, F.N. Chukhovskii and C. Malgrange, (1983), Acta Cryst., **A39**, 387.

[34] Y. Epelboin, (1985), Materials Science and Engineering, **73**, 1.

[35] G.S. Green, S.F. Cui and B.K. Tanner, Phil. Mag., (in press).

[36] A. Authier, C. Malgrange and M. Tournarie, (1968), Acta Cryst., **A24**, 126.

[37] P.V. Petrashen, (1976), Fiz. Tverd. Tela, **18**, 3729.

[38] Y. Epelboin, (1981), Acta Cryst., **A37**, 132.

[39] Y. Epelboin, (1983), Acta Cryst., **A39**, 761.

[40] Y. Epelboin, A. Jeanne-Michaud and A. Zarka, (1979), J. Appl. Cryst., **12**, 201.

[41] Y. Epelboin, (1978), J. Appl. Cryst., **11**, 675.

[42] S.F. Cui, Z.H. Mai and L.Z. Quian, (1984), Scientia Sinica, **A27**, 213.

[43] S.F. Cui, P.W. Ge, Y.Q. Zhao and L.S. Wu, (1979), Acta Phys. Sinica, **28**, 795.

[44] W. Bergholz, M.J. Binns, G.R. Booker, J.C. Hutchison, S.H. Kinder, S. Messoloras, R.C. Newman, R.J. Stewart and J.G. Wilkes, (1989), Phil. Mag. B, **59**, 499.

[45] Z.H. Mai, S.F. Cui, J. Lin and Y. Lu, (1984), Acta Phys. Sinica, **33**, 922.

[46] J.D. Eshelby, (1956), *Solid State Physics - Advances in Research and Applications*, (ed. F. Seitz and D. Turnbull), Academic Press, New York, p.79.

[47] C. Teodosiu, (1982), *Elastic Models of Crystal Defects*, Springer-Verlag, p.287.

[48] F. Balibar and A. Authier, (1967), Phys. Stat. Sol. (a), **21**, 413.

[49] S.F. Cui, G.S. Green and B.K. Tanner, (1989), Mat. Res. Soc. Symp. Proc., **138**, 71.

[50] M. Lefeld-Sosnowska, J. Gronkowski and A. Andrejczuk, (1988), Proc. 8th Int. Sch. on Defects in Crystals, World Scientific Press, p. 91.

[51] N. Kato, (1963), *Crystallography and Crystal Perfection*, (ed. G.N. Ramachandran), Academic Press, p.163.

[52] E.S. Meieran and I.A. Blech, (1972), J. Appl. Phys., **43**, 265.

[53] N. Kato, (1963), J. Phys. Soc. Jpn., **18**, 1785.

[54] N. Kato, (1964), J. Phys. Soc. Jpn., **19**, 67.

[55] M. Hart, (1966), Z. Phys., **189**, 269.

[56] G.S. Green and B.K. Tanner, (1987), Inst. Phys. Conf. Ser. No. 87: Section 9, I.O.P. Publishing Ltd.

[57] G.E. White and H. Chen, (1984), Materials Letts., **2**, 347.

[58] F.N. Chukhovskii and P.V. Petrashen, (1975), Sov. Phys. J.E.T.P., **42**(2), 243.